APPLICATION OF CFD TO MODEL AN AEROENGINE INTERNAL GEARBOX

ADAM JAMES TURNER MEng

Thesis submitted to the University of Nottingham
for the degree of Doctor of Philosophy

JULY 2015

Abstract

This thesis describes research undertaken to improve computational modelling capability for the internal gearbox (IGB) of an aeroengine. Using the commercial computational fluid dynamics (CFD) software ANSYS FLUENT modelling methodologies for regions within the IGB have been developed, applied and refined.

The IGB is a bearing chamber that houses the bearings that support the low pressure, intermediate pressure and high pressure shafts and in addition the spiral bevel gear pair that enable power to be taken from the high pressure shaft to power aircraft auxiliary systems. Within civil aeroengines parasitic power loss is a significant issue and as oil is used to lubricate and cool throughout the engine, this power loss largely manifests as increased heat-to-oil (HTO). A significant contributor to HTO is the IGB. The IGB contains complex geometry and a highly rotating two-phase flow consisting of films, droplets, ligaments and mist.

Central to the IGB is the spiral bevel gear pair. Previous modelling research has shown that detailed modelling of flow behaviour is too computationally expensive for domains larger than a few teeth. Modelling the meshing gears with full flow fidelity is not yet feasible. In this thesis a significantly less computationally expensive approach is explored. The complex gear-shroud geometry is replaced by a smooth cone with momentum sources used to generate the required fluid motion. In the single phase model these momentum sources were tuned/calibrated against a full tooth model spanning four teeth. The model was capable of generating flow behaviour to within 5% of the full tooth model. Oil was added as a discrete phase with a film model but was less successful as oil motion is strongly affected by geometrical detail.

A second approach to whole chamber modelling was proposed where the chamber is split into three zones and coupled via boundary conditions. Single phase investigation showed that the amount of swirl in the front chamber affects computed windage power loss with the maximum occurring at an inlet swirl number of around 0.5. The amount of swirl at gear entry does not however affect the amount of swirl at shroud exit and this shows that decoupling of the front chamber is viable.

The investigations into the zonal coupling of the IGB highlighted the importance of the geometry of the rear chamber (between gear and bearing) on the flow through the gear. A study to investigate how best to model the two-phase flow in this rear chamber was conducted. Transient models showed the volume of fluid approach (VOF) to be inadequate whereas a full two-phase Eulerian model converged, yielding viable results consistent with limited qualitative experimental data. The computational model predicts significant accumulation of oil towards the bearing side of the chamber, with this oil stripping periodically through shroud exit slots to the front chamber.

In the final part of the research a parametric study on several geometric features in the rear chamber was conducted using the developed two-phase modelling methodology. The chamber size, rear wall geometry, shroud exit slot location and size were investigated.

The work in this thesis improves IGB modelling capability through

- Establishing the capabilities and limitations of momentum source approach for full two-phase modelling of a shrouded gear
- Establishing that to some extent a bearing chamber can be productively modelled as separate but linked zones
- Identifying a successful modelling methodology for the high volume fraction two phase flow in the rear chamber

In addition the work in this thesis shows that

- For single phase flow the amount of swirl at gear inlet affects the windage power loss
- The behaviour of oil in the rear chamber, including the amount trapped and the exit condition, are strongly affected by chamber geometry

Guidelines for rear chamber design are also suggested.

Acknowledgements

I would like to thank Rolls-Royce Civil Aerospace for the financial and technical support they have provided throughout this project, in particular to my technical customer Adrian Jacobs.

I'd also like to thank my supervisors Dr Hervé Morvan and Dr Kathy Simmons for their invaluable guidance and support at every stage of this project. In addition I'd like to thank Dr Graham Johnson for sharing his technical expertise and for always helping out a PhD student in need, even when he probably should have been doing something else.

Utmost thanks must go to Samira Parhizkar for her unwavering belief and patience and to my family, friends and colleagues without whom I would not be where I am today.

Finally I would like to thank the University of Nottingham Taekwondo Club for providing innumerable opportunities for self development and procrastination over the years. For that I will be forever grateful.

Contents

List of Figures x

List of Tables xix

Nomenclature xxi

1 Introduction **1**

1.1 Overview 1

1.2 Background 1

1.3 Aims and Objectives 5

1.4 Thesis Outline 6

2 Literature Review **9**

2.1 IGB Full Chamber Modelling 9

2.2 Rotating Gears 12

2.2.1 Experimental 12

2.2.2 CFD 21

2.3 Rotating Cones 30

2.3.1 Experimental 31

2.3.2 CFD 34
2.4 Gear Tooth Submodel 36
2.5 Summary 40

3 CFD Methodology **42**

3.1 Navier-Stokes Equations 43
3.2 Spatial Discretisation 44
3.3 Temporal Discretisation 46
3.4 Pressure-Velocity Coupling 47
3.4.1 Rotating Reference Frame 48
3.5 Convergence 49
3.6 Boundary Conditions 50
3.6.1 Walls 50
3.6.2 Pressure Boundaries 50
3.6.3 Mass Flow Boundaries 51
3.6.4 Periodic Boundaries 51
3.7 Turbulence 52
3.7.1 Turbulence Modelling 52
3.7.2 The $k - \epsilon$ RNG Model 54
3.7.3 Wall Functions 57
3.8 Multiphase Models 62
3.8.1 The Discrete Phase Model 62
3.8.2 The Thin Film Model 64
3.8.3 The Volume of Fluid Model 67

3.8.4 The Eulerian Model 72

3.9 Material Properties 75

4 Simplified Gear Modelling Methodology 76

4.1 Introduction 76

4.2 Momentum Source Approach 77

4.3 Geometry Creation 80

4.3.1 Full Tooth Model 80

4.3.2 Momentum Source Model 81

4.4 CFD Methodology 83

4.4.1 Full Tooth Model 84

4.4.2 Momentum Source Model 87

4.5 Momentum Source Model CFD Analysis 91

4.5.1 Data Analysis 91

4.5.2 Single Phase Results 92

4.5.3 Single Phase Simple Chamber Model 100

4.5.4 Two Phase Full Tooth Model Results 103

4.5.5 Two Phase Momentum Source Model Results 112

4.6 Momentum Source Model Conclusions 117

5 Zonal Coupling Study 121

5.1 The Zonal Approach 121

5.2 Computational Model 123

5.2.1 Model Geometry 123

5.2.2 CFD Methodology 123

5.3 Inlet Swirl Investigation 124

5.4 Shroud Restriction Geometry Investigation 130

5.5 Zonal Coupling Conclusions 134

6 Rear Chamber Modelling Investigation 136

6.1 Experimental Facility 137

6.1.1 Experimental Results 139

6.2 Geometry Creation 141

6.3 Single Phase Investigation and Mesh Optimisation 143

6.3.1 CFD Methodology 143

6.3.2 Mesh Independence Study 144

6.3.3 Validity of Axisymmetric Sector Model 149

6.4 Two Phase Investigation 151

6.4.1 Volume of Fluid (VOF) Model 151

6.4.2 Eulerian Model 156

6.5 Rear Chamber Modelling Conclusions 162

7 Rear Chamber Parametric Study 163

7.1 Introduction 163

7.2 CFD Methodology 164

7.3 Single Phase Analysis 164

7.3.1 Chamber Vortices 165

7.3.2 Jet Characterisation 172

7.3.3 Gear Torque 174

7.3.4 Wall Shear 178

7.4 Two Phase Analysis 182

7.5 Parametric Study Conclusions 185

7.5.1 Single Phase Conclusions 185

7.5.2 Two Phase Conclusions 187

8 Conclusions **189**

8.1 Attainment of Objectives 189

8.2 Future Work 197

8.3 Contribution to Science 199

References **200**

Appendix A **209**

List of Figures

1.1 A cut-through of a Trent style engine, the red box shows the IGB location. Image courtesy of Rolls Royce PLC. 2

1.2 A front view of the physical spiral bevel crown gear used within this work. 3

1.3 A close up of the IGB of a Trent style aeroengine. The figure includes the gear, shroud, main location bearing, main and rear chambers as well as the rotating shafts and stationary elements. . 4

1.4 Mechanism of windage power loss proposed by Johnson [9] 5

2.1 Image showing Johnson's gear windage test rig [7] 16

2.2 Graph showing Johnson's data for non-dimensional moment coefficient against shaft speed for a shrouded and unshrouded gear. Both rotational directions are included [7] 18

2.3 Logarithmic scale graph showing moment coefficient against rotational Re number for a shrouded gear, taken from experimental work in Simmons et al. [26] 20

2.4 Graph of Gear torque against time showing the transient fluctuation in Rapley's work [28] 22

2.5 Changes in gear torque with mass flow rate through the gear. CFD data is from Webb [24] and experimental data is from Johnson [7]. 25

2.6 Mean static pressure profiles along the shroud. CFD data is from Webb [24] and experimental data is from Johnson [7] 25

2.7 Comparison of shroud outlet shapes tested by Webb [24]. The control case is shown in black 28

2.8 Oil streak under the shroud at 5000 RPM. 1: crown gear; 2: shroud inlet; 3: into-mesh oil jet; 4: gear outer diameter; 5: path of oil under the shroud [2] 29

2.9 Image depicting the experimental rig used by Yamada and Ito [27] 32

2.10 Experimental data from Yamada and Ito (graphed by Simmons et al [26]) showing variation of torque coefficient C_m with rotational Reynolds' number 33

2.11 Graph of moment coefficient against rotational Reynolds number for a rotating cone. The graph shows Rapley's work [39] comparing his data with Yamada and Ito's experimental results [27]. Vertex angle = 90°, non dimensional gap width = 0.008 and non dimensional throughflow = 1,500 35

2.12 Graph plotting the turbine efficiency η and velocity ratio for a momentum source CFD modelled hydro kinetic turbine and theoretical results. Image originally from Gaden and Bibeau [40]. . . 38

2.13 Diagram showing the replacement of the full tooth geometry (blue) with the cone and momentum source fluid sub region (green). Image originally from Kay [41] 39

2.14 Graph showing the comparison of static pressure at non dimensionalised points along the shroud for an explicitly modelled tooth and two momentum source models. Point A is equivalent to the shroud nose, point B is the beginning of the momentum source sub-region, point C is the end of the momentum source sub-region, point D is the beginning of the shroud gutter and point E is the beginning of the shroud restriction. Taken from Kay [41] 40

3.1 Simplified wall interaction chart for the wall film model available in FLUENT. E is the impact energy of the droplet and T_W is the wall temperature. 65

4.1 The cone and momentum source region superimposed onto the full tooth model. The image shows both the side profile of the tooth domain and a cross-section. The fluid sub region is highlighted in blue. Please refer to Figure 1.2 to see an image of the complex physical gear. 79

4.2 Side view of the full tooth model showing all relevant boundary conditions. 80

4.3 Boundary conditions for the cone and momentum source model. Blue lines represent pressure inlets, red lines pressure outlets and green lines rotating walls. 82

4.4 Image showing a) the full 15.82° cone model mesh and b) a side view of the fluid sub-region, highlighted in red. Note, the apparent step changes in mesh density shown are due to the difficulties of displaying fine mesh regions in an image and do not exist in the actual model. 83

4.5 Graph showing the convergence of gear moment against flow time for the 10th gear revolution of the full tooth model. 87

4.6 Mass flow rate data for the inlet and outlet of the momentum source model taken over 10,000 steady state iterations for model SM3 (please refer to Table 4.1). 89

4.7 Mass flow rate data for the inlet and outlet of the momentum source model taken over 17 transient gear rotations for model SM3 (please refer to Table 4.1). 90

4.8 Cross-sections of a) full tooth model and b) momentum source model. The yellow lines represent the profile lines that were averaged to produce a velocity profile for each model. 92

4.9 Side view of momentum source model domain showing points of data comparison through the tooth region and at the shroud restriction. The non-dimensional position of key geometry features on the shroud are also displayed at the bottom of the image. . . 93

4.10 Axial and azimuthal velocity components at the shroud restriction for the full tooth model (FTM), the cone model without momentum sources (CM), and 3 source models variants (SM1-3). 97

4.11 Jet and azimuthal velocity components at the shroud outlet for the full tooth model (FTM), the cone model without momentum sources (CM), and three source term models (SM1-3). 98

4.12 Boundary conditions for cone model with outer chamber. The green lines represent moving walls and black lines are stationary walls. The gear carrier detail is not shown in this figure and forms no part of the CFD model. 100

4.13 Jet and azimuthal velocities at the shroud outlet for the full tooth model (FTM), calibrated source model (SM2), and calibrated source model with an outer chamber (FCM). 102

4.14 Boundary conditions for the full tooth model. Inlet droplet injection surface is highlighted in dark blue. 104

4.15 Percentage of droplets released into the domain that impact the shroud for geometrically representative model with escape boundary conditions (Red) and with reflect boundary conditions (blue). The impact position along the shroud is non-dimensionalised between 0 and 1. Refer to Figure 4.9 for non-dimensionalised shroud positions. 105

4.16 Boundary conditions for the full tooth model. Into-mesh droplet injection surface is highlighted in dark blue. 107

4.17 Percentage of droplets released into the domain from the into-mesh location that impact the shroud for the full tooth model. The impact position along the shroud is non-dimensionalised between 0 and 1. Refer to Figure 4.9 for non-dimensionalised shroud positions. 108

4.18 Boundary conditions for the full tooth model. The injection surface (gear topland) is highlighted in dark blue. 110

4.19 Film thicknesses for the oil impacting on the underside of the shroud. The left image shows film thickness at about 1/20th of a revolution and the right image shows film thickness at about 1/10th gear revolution. 111

4.20 An isometric and a side view of the computational domain displaying droplet locations at $4.8 \times 10^{-4}s$ (approximately 1/10th gear revolution). Droplets are coloured by residence time. The side of the chamber is coloured in grey and the rotating surfaces in green for clarity. 112

4.21 Boundary conditions for the momentum source model. Into-mesh droplet injection surface is highlighted in blue and shroud inlet injection surface is highlighted in brown. 113

4.22 Histograms comparing percentage of injected droplets that impact the shroud for the momentum source model (blue) and representative geometry model (red). Droplets are injected at the shroud inlet and impact locations on the shroud are non-dimensionalised between 0 and 1. Refer to Figure 4.9 for non-dimensionalised shroud positions. 114

4.23 Droplet tracks for the momentum source model with droplets injected at the shroud inlet. Location of droplets impacting shroud gutter at high speed is circled in red. 115

4.24 Histogram comparing percentage of injected droplets which impact the shroud for the momentum source model (blue) and representative geometry case (red). Droplets are injected representing the into-mesh jet and impact locations on the shroud are non-dimensionalised between 0 and 1. Refer to Figure 4.9 for non-dimensionalised shroud positions. 117

5.1 Diagram showing the three main regions in the gear windage test rig: 1. the gear and shroud subsystem, 2. the rear chamber and 3. the main chamber. 122

5.2 Side view of model domain showing locations of data comparison through the tooth region and at the shroud restriction. 125

5.3 Plot of the azimuthal swirl velocity at a) the shroud inlet (Position 1), b) the bottom of the tooth valley (Position 2), c) the top of the tooth valley (Position 6) and d) the shroud outlet (Position 8) for 5 different full tooth models, each with a different inlet swirl velocity. 126

5.4 Graph showing the effect of inlet swirl on gear torque through the full tooth model. 127

5.5 Graph showing the effect of inlet swirl on mass flow rate through the full tooth model. 129

5.6 Velocity magnitude vectors at the shroud inlet for Cases 1, 3, 5 and 6. The black arrows display the direction of the flow entering the shroud. 130

5.7 Four different models with varying shroud and outlet geometries. a) New shroud with restricted outlet (Case A), b) New shroud with open outlet (Case B), c) Webb's shroud with restricted outlet (Case C), d) Webb's shroud with open outlet (Case D). Blue arrows show flow into the domain and red arrows show flow out of the domain. a) is the present study case; d) is typical of Webb's work. 132

5.8 Comparison of a) axial, b) radial and c) azimuthal velocities at the shroud restriction for four geometry variations Cases A, B, C and D. Geometry features are described in Table 5.2 for each case. 133

6.1 UTC gear windage rig - base configuration [7]. 137

6.2 Test rig as configured for the rear chamber study [67]. 138

6.3 Test rig as configured for the rear chamber study [67]. 138

6.4 Image showing a top down view of the experimental rig rear chamber (enclosed in red) at shaft speed 10,000 RPM and 4.3 lpm oil flow rate. The black line is used to more clearly denote the film interface. 139

6.5 Image showing a) the left and b) the right sides of the experimental rig rear chamber (enclosed in red on each image) at shaft speed 10,000 RPM and 4.3 lpm oil flow rate. The left hand side shows shearing flow upwards opposing gravity. The right hand side shows shearing flow downwards in the same direction as gravity. The black line is used to more clearly denote the film interface. 141

6.6 Side view of the rear chamber computational domain. 142

6.7 Image showing the rear chamber and planes of comparison, shown in black. 146

6.8 Velocity magnitude profile at the shroud outlet hole for each mesh. 146

6.9 Comparison of velocity magnitude vectors for the M1 (1,600,000 cells), M4 (400,000 cells) and M5 (320,000 cells) mesh independence models. 148

6.10 Image showing the secondary flow (azimuthal component removed) in the rear chamber. Block arrows show the bulk direction of flow. 149

6.11 Graph showing the azimuthal velocity profile across the rear chamber for a single phase simulation at 10,000 RPM. Data is taken from position 3 (see Figure 6.7). 151

6.12 Image showing contours of oil volume fraction in the rear chamber for the VOF model. The left hand side shows contours through a plane through the centre of the domain and the right hand side shows an isometric view of iso-contours of oil volume fraction. Dark Blue is for α=0.01, light blue for α=0.1, green for α=0.5 and red for α=1. 154

6.13 Graph showing the mass of oil, simulated by the VOF model, within the rear chamber as a function of time. The black plus sign on the graph represents the point in the simulation that the mesh was refined from 400,000 cells to 900,000 cells. 155

6.14 Image showing contours of oil volume fraction in the rear chamber for the Eulerian model. The left hand side shows contours through a plane through the centre of the domain and the right hand side shows an isometric view of iso-contours of oil volume fraction. Dark Blue is for α=0.01, light blue for α=0.1, green for α=0.5 and red for α=1 157

6.15 Graph showing the mass of oil, simulated by the Eulerian model, within the rear chamber as a function of time. Point 0 refers to the beginning of the Eulerian model. The other points 1-5 refer to the stages illustrated in Figure 6.17. 158

6.16 A close up view of the rear chamber outlet showing the impact of the gear jet on the oil film in this region at 2 seconds into the simulation (point 2 in Figure 6.15). Volume fraction is displayed as light blue for α=0.1, green for α=0.5 and red for α=1. A non uniform film height along the top wall is clearly identifiable. . . . 159

6.17 Images showing the progression of oil build up within the rear chamber over time. Volume fraction is displayed as light blue for α=0.1, green for α=0.5 and red for α=1. The mass of oil in the chamber for each stage can be seen in Figure 6.15 160

6.18 Graph showing the azimuthal velocity profile across the rear chamber for both single phase and Eulerian multiphase models. Data is taken from position 3 (see Figure 6.7). 161

7.1 Parametric variations for the rear chamber. Baseline case, A) relocated shroud hole, B) reduced chamber dimensions, C) slanted back wall section and D) reduced area shroud outlet hole. 165

7.2 Time averaged, velocity magnitude vectors in the rear chamber for all models. Baseline case, A) relocated shroud hole, B) reduced chamber dimensions, C) additional slanted back wall feature and D) resized shroud outlet hole. 166

7.3 In plane, time averaged velocity vectors for the Baseline chamber model. 167

7.4 Time averaged velocity vector comparison of the Baseline model (left) and model A (right) with relocated shroud outlet hole. Oil path for both models is overlaid in red. 168

7.5 Time averaged velocity vector comparison of models A (left) and B (right) with reduced chamber dimensions. Key differences in vortex structure are highlighted in red. 169

7.6 Time averaged velocity vector comparison of models B (left) and C (right) with additional sloped back wall feature. 170

7.7 Time averaged velocity vector comparison of models C (left) and D (right) with resized shroud outlet hole. 171

7.8 Front and top down views of the shroud outlet hole velocity vectors and in plane velocity contours for all five models. 173

7.9 Image comparing the time averaged wall shear on the chamber's rotating surfaces between models A and B. The key region of shear comparison is circled in red. 177

7.10 Comparison of the time averaged wall shear on the stationary top and back chamber walls for all models. 180

7.11 Figure comparing the time averaged wall shear on chamber top and back walls for models A (left) and B (right). Key regions of wall shear comparison are highlighted in red. 181

7.12 Figure comparing the time averaged wall shear on chamber top and back walls for models B (left) and C (right). The key region of wall shear comparison is circled in red. 182

7.13 Graph tracking the mass of oil in the chamber domain with time. Model D is shown in red and the baseline case is shown in blue. . 183

7.14 Series of images showing the vectors and oil volume fraction contours for the distinct phases of the rear chamber cyclic behaviour. Each images refers to a numbered point on the inset oil residence graph. 184

8.1 Image showing the iterative approach to converge the boundary conditions between the full tooth model and the main chamber model. First a full tooth simulation is computed. The outlet flow of this model is set as the inlet of the main chamber model. The main chamber model is then computed and the outlet flow is then set as the inlet to a second full tooth model. This process is then iterated until the boundary conditions at the inlets and outlets converge to a consistent value. 210

8.2 Figure of the main chamber model domain with all boundaries labelled. 211

8.3 Graph of the main chamber mesh independence for cell densities of 200,000, 400,000 and 800,000. Figure is taken from Simmons et al [54]. 212

8.4 Figure showing the contours of time average circumferential velocity in the main chamber. A close up of the swirl velocity in the region of the shroud inlet is also shown. 213

8.5 Figure showing the contours of time averaged total gauge pressure in the main chamber. A close up of the pressure in the regions of the shroud outlet (point 1) and the shroud inlet (point 2) is also shown. 214

List of Tables

3.1 Materials used within this thesis and their properties. 75

4.1 Table detailing the momentum source terms applied in the cylindrical coordinate system for the momentum source models analysed in this thesis. 94

4.2 Non-dimensional velocity and mass flow data at the inlet of the cone model. The case without momentum source (CM) and three momentum source models (SM1-3) are compared to the full tooth model (FTM). The percentage difference of each model from the FTM is given in brackets next to the corresponding value in the table. 95

4.3 Non-dimensional velocity and mass flow data at the shroud restriction of the cone model. The case without momentum source (CM) and three momentum source models (SM1-3) are compared to the full tooth model (FTM). The percentage difference of each model from the FTM is given in brackets next to the corresponding value in the table. 95

4.4 Non-dimensional velocity and mass flow data at the shroud outlet of the cone model. The case without momentum source (CM) and three momentum source models (SM1-3) are compared to the full tooth model (FTM). The percentage difference of each model from the FTM is given in brackets next to the corresponding value in the table. 96

4.5 Velocity and mass flow data at the shroud outlet for the calibrated source model (SM2), and a calibrated source model with an outer chamber (FCM). Data is given in relation to the full tooth model (FTM). The percentage difference of each model from the FTM is given in brackets next to the corresponding value in the table. 101

5.1 Cases run and their inlet swirl velocity values. 125

5.2 Cases run and their key geometry features. 131

5.3 Tabulated mass flow values at the shroud restriction for each case. 134

6.1 Mesh designations and number of cells. 145

6.2 Velocity magnitude averages and error from control mesh for each case at position 1 (shroud outlet hole). 147

7.1 Table showing the time averaged torque loss on the rotating chamber surfaces for all models. Percentage differences from the baseline case are also given for each model. 176

7.2 Table showing the average wall shear on the stationary back and top chamber walls for all models. Percentage differences from the baseline case is also given for each model. 179

Nomenclature

AGB	Accessory Gearbox
AMG	Algebraic Multigrid Method
CFD	Computational Fluid Dynamics
CM	Cone Model, a model designation
DPM	Discrete Particle Model
FCM	Full Chamber Model, a model designation
FTM	Full Tooth Model, a model designation
HP	High Pressure
HTO	Heat to Oil
IGB	Internal Gearbox
IP	Intermediate Pressure
LCDM	Laser Confocal Displacement Meter
RNG	Renormalization Group Theory
SFC	Specific Fuel Consumption
SMx	Source Term Model x, a model designation
UTC	University of Nottingham Technology Centre in Gas Turbine Transmission Systems
VOF	Volume of Fluid Multiphase Model
WPL	Windage Power Loss

α	–	Volume Fraction
Γ	–	Diffusion Coefficient
Γ	–	Blending Function
γ	–	Under-Relaxation Factor
δ_{bl}	[m]	Boundary Layer Thickness
δ_{ij}	–	Kronecker Delta
ϵ	[m^2s^{-3}]	Turbulent Dissipation Rate
η	–	Turbine Efficiency
θ_c	[degrees]	Cone Apex Angle
λ	–	Gravitational Parameter
μ	[Nsm^{-2}]	Dynamic Viscosity
μ_{eff}	[Nsm^{-2}]	Effective Viscosity
μ_t	[Nsm^{-2}]	Turbulent Viscosity
ν	[m^2s^{-1}]	Kinematic Viscosity
ρ	[kgm^{-3}]	Density
$\sigma_k, \sigma_\epsilon$	–	Turbulent Prandtl Numbers
$\sigma_{i,j}$	[Nm^{-1}]	Surface Tension Coefficient
σ_p	[Nm^{-1}]	Liquid Surface Tension
τ	[Pa]	Shear Stress
τ_p	[s]	Particulate Relaxation Time
τ_w	[Pa]	Wall Shear Stress
$\overline{\overline{\tau}}$	–	Stress Tensor
$\overline{\overline{\tau}}_{eff}$	[$kgm^{-1}s^{-2}$]	Effective Dissipation
Φ	–	Level Set Function
$\widetilde{\phi_f}$	–	Average Scalar Value
ω	[$rads^{-1}$]	Gear Rotational Speed
$\overrightarrow{A}$	[m^2]	Area Vector
C	–	Courant Number

C_D	–	Drag Coefficient
C_m	–	Non-Dimensional Torque Coefficient
C_μ	–	Constant Used in the RNG Turbulence Model (= 0.0845)
C_q	–	Non-Dimensional Flow Rate
C_s	–	Momentum Source Factor
CFL	–	Courant Friedrichs Lewy Condition
d	[m]	Droplet Diameter
$\overline{d}$	[m]	Mean Droplet Diameter
E	[$\mathrm{Jkg^{-1}}$]	Energy Per Unit Mass
E	–	Non-Dimensional Droplet Impact Energy
f	–	Drag Function
g	[$\mathrm{ms^{-2}}$]	Gravitational Acceleration
h_{film}	[m]	Film Height
I	–	Identity Matrix
K_{pq}	[$\mathrm{kgm^{-3}s^{-1}}$]	Interphase Momentum Exchange Coefficient
k	[$\mathrm{Jkg^{-}1}$]	Turbulent Kinetic Energy
k_P	[$\mathrm{Jkg^{-}1}$]	Turbulent Kinetic Energy at the Near Wall Node P
k	–	Von Kármán Constant
k_{eff}	[$\mathrm{Wm^{-1}K^{-1}}$]	Effective Thermal Conductivity
l	[m]	Characteristic Length
$\dot{m}$	[$\mathrm{kgs^{-1}}$]	Mass Flow Rate
n_s	–	Droplet Spread Parameter
p	[Pa]	Pressure
Q	[$\mathrm{m^3s^{-1}}$]	Volume Flow Rate
R^ϕ	–	Unscaled Residual Error
Re_{rot}	–	Rotational Reynolds Number

r	[m]	Gear Radius
S	–	Swirl Number
S_h	[kgm^{-1}s^{-3}]	Volumetric Heat Source
S_M	[kgm^{-2}s^{-2}]	Momentum Source Term
s	[kgm^{-2}s^{-1}]	Momentum Per Unit Volume
s	[m]	Cone to Shroud Clearance
$\Delta\vec{s}$	[m]	Displacement Vector
T	[Nm]	Gear Torque
T_w	[K]	Wall Temperature
t	[s]	Time
Δt	[s]	Time Step
U^*	–	Non-Dimensional Velocity
U_f	[m^{3}s^{-1}]	Volume Flux Through Cell Face
U_{film}	[ms^{-1}]	Fluid Film Velocity
u, v, w	[ms^{-1}]	Velocity Components
$\overrightarrow{u}, \overrightarrow{v}, \overrightarrow{w}$	[ms^{-1}]	Velocity Vectors
$\overline{u}, \overline{v}, \overline{w}$	[ms^{-1}]	Mean Velocity Vectors
u', v', w'	[ms^{-1}]	Fluctuating Components of u, v, w
u_{nd}	–	Non-Dimensional Velocity Component
u_τ	[ms^{-1}]	Friction Velocity
V	[m^3]	Control Volume
W	[W]	Turbine Power
Y_d	–	Droplet Mass Fraction
y_P	[m]	Distance from Point P to the Wall
y^+	–	Non-Dimensional Cell to Wall Distance
y^*	–	Non-Dimensional Cell to Wall Distance

Definition of Non-Dimensional Values

$$C_m = \frac{T}{\frac{1}{2}\rho r^5 \omega^2}$$

$$CFL = \frac{u\Delta t}{\Delta x}$$

$$Re_{rot} = \frac{\rho r^2 \omega}{\mu}$$

$$S = \frac{u}{w}$$

$$u_{nd} = \frac{u}{r_{local}\omega}$$

$$y^* = \frac{\rho C_\mu^{0.25} k_p^{0.5} y_p}{\mu}$$

The distance along the shroud is normalised between 0 and 1 such that 0 is the shroud inlet and 1 is the end of the shroud restriction. Refer to Figure 4.9 for details.

The radial position between the gear and shroud is non-dimensionalised between 0 and 1 such that 0 is the gear surface and 1 is the shroud surface.

Chapter 1

Introduction

1.1 Overview

The aim of this project is to develop a modelling strategy for two-phase flow within aeroengine bearing chambers containing gears. This approach will be used as a tool to aid the design of an improved internal gearbox (IGB). The computational fluid dynamics (CFD) software FLUENT [1] is used in this project and supporting experimental and computational work, conducted by the University of Nottingham, is used for validation [2].

1.2 Background

There is a global drive for future aeroengines to have reduced fuel consumption and reduced emissions. Emission reduction targets have been agreed as part of a global aeronautical transport effort [3]. Targets include a 50% reduction in CO_2 and an 80% reduction in NOx by 2020 and must be met to avoid penalties and for manufacturers and airlines to remain competitive. Over the lifetime of an aeroengine the initial purchase cost is far outweighed by operating costs and a reduction in specific fuel consumption (SFC) leads directly to an increase in profit. For example in 2012 a 1% reduction in SFC across the industry could have saved $700 million [4].

In an aeroengine, the internal gearbox is used to take power from the high pressure (HP) shaft (and sometimes also the intermediate pressure (IP) shaft). Power is delivered to the accessory gearbox (AGB) via the radial drive shaft, usually located at approximately 85° from the main shaft and the AGB distributes it to various engine and aircraft accessories. These accessories include the oil pumps, breather and generators. Modern aircraft need increasingly large output from generators to power electrical equipment and as a result the radial drive shaft is required to transmit greater torque leading to greater losses. Hundreds of kW of energy are lost in the internal gearbox alone. Consequently efficient jet engine design creates a demand for improved transmission systems (thereby improving SFC). The location of the IGB within an aeroengine is shown in Figure 1.1.

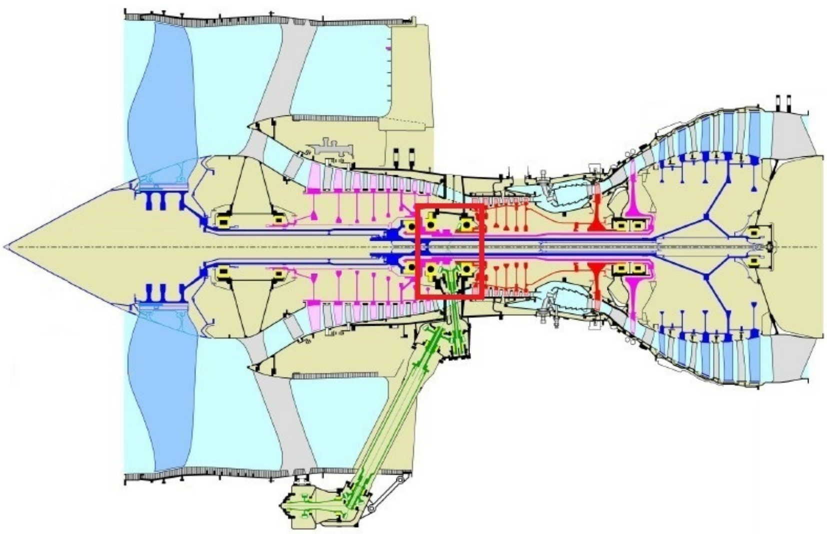

Figure 1.1: A cut-through of a Trent style engine, the red box shows the IGB location. Image courtesy of Rolls Royce PLC.

A spiral bevel gear pair is used to transmit torque between the main shaft and radial drive shaft. The crown gear is located on the main HP shaft with the pinion gear located on the radial drive shaft. A benefit of using spiral bevel gears is improved load bearing, a key consideration in aeroengine design. Reduced shock transmission is also beneficial due to the smoother meshing of bevel gears compared to less expensive gear types. Figure 1.2 shows a front view of the spiral bevel crown gear used within this thesis and Figure 1.3 shows the IGB geometry including the location of the gear.

Figure 1.2: A front view of the physical spiral bevel crown gear used within this work.

Aeroengine bearing chambers use oil both as a lubricant and as a coolant. Oil is supplied to gears (usually via directed jets at the gear meshing point) and bearings and is then removed (scavenged) from the chamber for cooling before being recirculated. A large ball bearing is located behind the gear and is the main location that oil enters the IGB. Oil from the into-mesh jets and bearing is introduced to the rear chamber (shown in Figure 1.3 surrounded by a black box) and ejected into the main chamber through holes in the shroud. The majority of this oil is then scavenged from the system however some is re-ingested by the gear to repeat the cycle. The entire engine oil volume circulates several times per

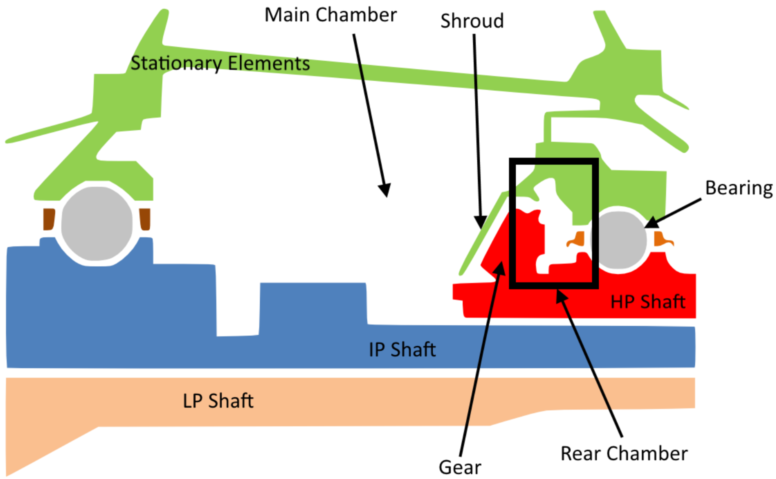

Figure 1.3: A close up of the IGB of a Trent style aeroengine. The figure includes the gear, shroud, main location bearing, main and rear chambers as well as the rotating shafts and stationary elements.

minute when the engine is running. Power loss in the system is transferred as heat energy to the oil, known as heat to oil (HTO), and efficient scavenge is necessary to avoid excessive heat degradation of the oil. Aeroengines run more efficiently at higher temperatures but oil temperatures are limited to about 225°C, so managing HTO is a key concern. Consequences of poor scavenge include coking of oil and increased fatigue and wear to expensive aeroengine components in addition to high HTO.

The main mechanisms of transmission power loss are churning losses, meshing losses, bearing friction losses and gear windage. Windage is the power required to rotate a gear in a fluid and causes increased turbulence and heat generation which, under regular operating conditions, accounts for approximately 10% of HTO [5]. It has been found that windage can be reduced by effective shrouding of the gear as well as efficient scavenging of oil from the system [6–8]. In particular, understanding the interaction between oil scavenge and gear windage is essential as the unnecessary working of oil results in increased power loss and excessive heat generation. This requires a system approach as each component of the flow affects some of the other components. Under exceptional conditions these interactions can cause extremely high HTO as the interaction model proposed by Johnson [9] shows in Figure 1.4.

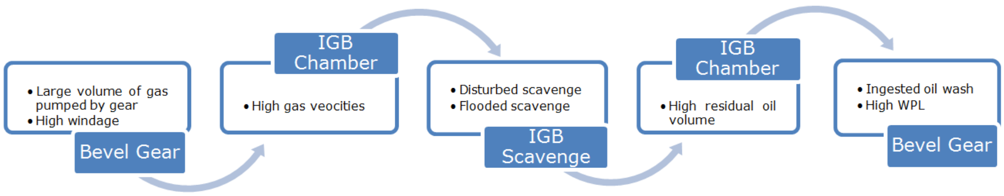

Figure 1.4: Mechanism of windage power loss proposed by Johnson [9]

The generation of a validated computational model will create an unrestricted picture of the complex fluid flows within an aeroengine IGB beyond what can currently be measured or visualised experimentally. This will lead to an improved understanding of air/oil behaviour and their interactions. The intention is that the model will develop to include high speed 3D airflows, meshing gear pair(s), oil films, oil pooling, scavenge and finally heat transfer, producing a complete chamber overview for the aeroengine designer.

1.3 Aims and Objectives

The aim of this project is to progress the development of computational modelling capability and strategy for two-phase simulation of bearing chambers containing gears, creating a system model of an aeroengine IGB. This research includes evaluation of a simplified representation of a gear and the developed models are used to appraise system behaviour and the impact of chamber design on performance.

At the outset objectives focused on developing a simplified modelling approach for a meshing gear pair and modelling a complete IGB system. However, the results from the developed simplified modelling approach called for a re-definition of overall objectives. The objectives for the research presented in this thesis are:

1. Progress CFD modelling capability for a full IGB bearing chamber through:
   (a) The development and evaluation of a momentum source model to replace the geometric and flow complexity of the spiral bevel gear pair.
   (b) Evaluation of the extent to which the IGB can be modelled as a series of linked sub-models.
   (c) Evaluation of the effectiveness of conventional CFD multiphase modelling approaches for modelling the bearing chamber behind the gear within an IGB.
2. Apply identified modelling approach for IGB gear back chamber to determine optimum from a range of proposed/existing designs.

1.4 Thesis Outline

This section outlines the structure used within this thesis and offers a brief description of each chapter.

Chapter 1 has covered the background to the project, offering motivations for the work and stated its aim and objectives. Chapter 2 details the relevant literature. The chapter highlights existing IGB and gear modelling work, both computational and experimental. The same is presented for rotating cones, which can be seen to be analogous to spiral bevel gears and are often used in gear modelling. Existing simplified gear models are also described and finally existing bearing chamber and multiphase work.

The computational fluid dynamics theory and models used within this thesis are outlined in Chapter 3. Justification is given here for model selection and, unless otherwise stated in the relevant section, the formulation described is used throughout the remaining work.

Chapter 4 is the first of four results chapters and presents a novel method of modelling a spiral bevel gear through use of a geometrically simplified representation. This includes the computational domain creation and discretisation, as well as the relevant modelling formulation with reference to Chapter 3. This model is validated against data generated using existing gear modelling techniques. Chapter 4 then goes on to show the result of adding an additional Lagrangian phase to the simplified model and draws conclusions on its performance. The single phase work in this chapter was published in the Proceedings of the XXI International Symposium on Air Breathing Engines, 2013 [10] and the multiphase work was presented at ASME Turbo Expo 2013 [11].

There are several options available to extending the work in Chapter 4 to an IGB methodology. These are discussed in Chapter 5 and a study is presented which determines the most appropriate option moving forward. As a part of this, the sensitivity of the windage rig flows to variations in velocity and geometry at the boundaries of the three distinct windage rig regions is investigated and recommendations about the benefits and limitations of a zonal modelling approach are discussed. The effect of these parameters on system performance is also be noted.

Having identified the chamber at the back of the gear as of key importance to the overall behaviour within the IGB, Chapter 6 presents a methodology to accurately simulate the two phase flows in this region. The method of domain creation and mesh independence are described as are the models employed to solve the simulation, again with reference to Chapter 3. Both the Volume of

Fluid (VOF) and Eulerian multiphase models are investigated and evaluated. The work in Chapter 6 was presented at ASME Turbo Expo 2014 [12].

The methodology devised in Chapter 6 is then utilised in Chapter 7 to conduct a parametric study on several key back chamber geometric features. These include chamber outer radius, chamber width, and additional design features. Design recommendations are then drawn from this analysis.

Finally, Chapter 8 summarises the main conclusions from the previous Chapters and presents recommendations for future work.

Chapter 2

Literature Review

This chapter reviews the previous work done in the field of internal gearboxes and other similar complex chamber flows as found in internal turbomachinary applications. It describes in some detail investigations into gear modelling and windage, a key mechanism of power losses within an IGB, as well as other significant sources of power loss.

The chapter further describes advances in two phase bearing chamber modelling and other relevant two phase modelling literature.

2.1 IGB Full Chamber Modelling

A modelling goal within the aerospace industry is to create a full engine model capable of quickly and affordably representing the performance of a given engine geometry. One-dimensional programs such as SPAN [13] are currently in use but full CFD as a design tool is invaluable and has been used for some time for structural and thermal-mechanical modelling. Chew and Hills [14] have reviewed the application of full engine modelling using CFD and conclude that its applications within the near future are very limited, citing processing power and limitations of RANS turbulence models as key reasons for this.

High fidelity models are possible, as demonstrated by Gorrell [15] who created an engine fan intake model. However 220 million cells were used within this model and 444 processors were required for the calculation, a computational expense not widely available. A requirement of 10-100 billion cells for a whole engine model has been estimated by Dawes [16] in 2007, establishing that full engine models are significantly beyond the scope of current computational resources.

In working towards larger system simulations, there have been some attempts in the past to create complex chamber models, though these works are limited in both number and scope. Chew and Hills [17] have investigated the application of CFD to model internal air systems and noted significant limitations in this area, including numerical difficulties, turbulence model insufficiencies and a limited understanding of flow mechanisms. Rotor-stator flow problems are particularly challenging including three dimensional geometry features and unsteady flow effects e.g. Taylor vortices. In spite of these challenges, confidence in CFD simulations for these types of flows has grown in recent years driven by improved methods.

The difficulties in creating three dimensional internal chamber models have also been highlighted by Long et al. [18] with their model for a HP compressor drive cone. Their initial simplified 3D simulations, which removed the tip clearance from the turbine blades, resulted in significantly altered tangential flows. This work was validated by experimental data from a rig containing a Rolls Royce RB211-535 engine geometry running at engine representative operating conditions.

The most relevant attempt at a full chamber model in the context of this present work was conducted by Sun et al. [19], who created a complete single phase IGB model in 2D. The three dimensional effects of non axisymmetric rotating components, e.g. bolts and gears, were simulated by porous medium regions. The drag coefficients of each were determined by empirical calculations and separate CFD investigations. Using this model the authors were able to show the key flows in the gears and chamber, and that these flows are strongly dominated by gear pumping effects. There are still many limitations to this work. Firstly the simulation is only two dimensional, making it unable to capture the strong three dimensional flows known to be present in an IGB. Secondly there has been no validation for the full model and no sensitivity analysis on their porous media approximations. Finally the model only runs in single phase without oil, though the authors propose that adding an oil phase would be feasible.

In the first instance this project will model only a single gear and its interaction with the air flow. In this case windage is the only possible source of power loss. Following the completion of a simplified gear model, its interactions with the other components in IGB chamber will be studied and the losses relating to a gear pair within a transmission system will be relevant. These include meshing losses, gear pumping and churning losses.

Though this literature review primarily focuses on fluid flow interaction (and resultant losses), it important to understand and evaluate other sources of transmission power loss pertinent to an IGB chamber. Lord [5] attributed typical percentages to the following mechanisms in terms of their relative contribution to total power loss for a spur gear:

- Combined Windage and churning losses 10%
- Bearing losses 50%
- Meshing losses 40%

It is important to note that these percentages are highly dependant on operating conditions. For example, Handschuh [20] found that for a helical gear train meshing losses dominated at low rotational speeds but gear windage losses dominated at high speeds (around 15,000 RPM). At present no data source has been found that gives a comparable breakdown for an aeroengine IGB. It is likely that windage losses will contribute a far higher proportion than for the spur gear. Further investigative work is required in this area.

2.2 Rotating Gears

This project aims to construct an IGB modelling strategy starting with a model of a spiral bevel gear pair. Mass flow and gas velocities are essential to this and both are heavily linked to gear windage. There is only a limited amount of literature describing the behaviour and windage of spiral bevel gears and this has largely been conducted at the University of Nottingham. However there has been a wider array of work on spur gears, which have a much simpler geometry. A review paper by Eastwick and Johnson [21] published in 2008 compiles most of the known gear windage literature and gives a comprehensive overview of the subject. Sections 2.2.1 and 2.2.2 summarise the literature relevant to this current work.

2.2.1 Experimental

The first experimental study on gear windage was conducted by Dawson [6, 22] investigating power loss from spur gears. Dawson conducted a parametric study varying gear size, speed and geometry as well as looking at different forms of gear shrouding [22]. His experimental apparatus consisted of an electric motor driven, horizontally mounted shaft, with gears made from hardwood and cardboard rotating in free space. From testing 37 different spur gears, including a rotating disk and rotating drum, he was able to conclude that windage power loss, WPL, is approximately proportional to gear speed to the power of 2.9 and was also able to attribute 90% of WPL to the gear teeth (by comparison with the smooth drum case). The range of gears tested included root diameters 300-1160 mm, face width 32-543 mm and tooth module 2-16 mm.

Of further note was Dawson's observation that a rotating gear acts similarly to a centrifugal fan and axially draws in air before expelling it radially and tangentially. This requires work to be done on the air and is therefore seen as increasing windage power loss. It is this fan behaviour that the current model aims to replicate.

This discovery led to a concept of using paper washers to block of the ends of the gears, restricting air flow and reducing WPL by 22-44%. Along similar lines, Dawson looked at shrouding the gear to further restrict the passage of air through the gear. By employing a close fitting shroud WPL reductions of 66% were observed.

Dawson expanded on this work [6] by expressing the windage on spur gears in terms of non-dimensional coefficients, including the non-dimensional torque coefficient C, which is defined as

$$C = C\text{''}[Re/(5 \times 10^5)]^\alpha \tag{2.1}$$

where C'' is a constant shape factor which is dependant in the shape of the gear and is the value of C at $Re = 5 \times 10^5$. This constant can be read from a chart published by Dawson [6]. Within the range of his experimental work Dawson estimates $\alpha = -0.15$.

Dawson then expressed windage power loss, P as

$$P = 1.12 \times 10^{-8} C" \rho N^{2.95} D^{4.75} \nu^{0.15} \lambda \tag{2.2}$$

where N is gear rotational speed (RPM), D is gear root diameter, ν is the kinematic viscosity of the fluid surrounding the gear, and λ is a scaling factor to account for the effects of the gear enclosure. λ varies between 0.5 and 1 where 0.5 is a tightly enclosed gear and 1 is the gear running in free space.

A key conclusion from this equation is that WPL scales strongly and unfavourably with gear diameter.

Winfree's [8] gear windage investigations on bevel gears, for which previously there had been very little data, are of more relevance for the present work. Winfree ran experiments on a single shrouded high speed spiral bevel gear with the intention of isolating and measuring its windage effects. The rig consisted of a vertically mounted gear (with 38 teeth and a 15" diameter) and shroud housed in a clear Plexiglas casing. The shroud and casing were designed for multiple shroud configurations and the gear was capable of running up to 6,500 RPM and 333 K. A lubricating spray was included to run in 'wet' conditions, where the liquid used was water. A pinion gear was not included but one was simulated using 1" Plexiglas to block the flow coming across the gear face between the jets.

Seven different shroud configurations were tested looking at the inlet restriction, outlet restriction and gap width. The conclusions of which were that for an air only case, maximum restriction of both inlet and outlet was beneficial, similar to that shown by Dawson [22]. Optimum shroud configurations gave WPL reductions of up to 79%.

There are however several differences once an oil phase has been introduced. Winfree observed that it is no longer enough to restrict the fluid flow but it is also necessary to scavenge oil from under the shroud. In this case restricting the inlet is still a benefit however it becomes detrimental to tightly restrict the outlet and gap width. This traps oil underneath the shroud, meaning the gear does more work on a more dense fluid, and as a result increases WPL. Effective shroud design, such as a greater gap width and open outlet, can aid oil scavenge. There is a small amount of oil supplied in the into-mesh jet (to lubricate the gear mesh) but there would be a significant impact on the system if the large excess of oil in the main chamber was ingested by the gear. This requires an understanding of how the gear and shroud interact with flows in the main chamber.

An effective means to scavenge oil is to include slots in the shroud. Winfree also conducted experiments to find the best combination of slots, concluding that only one slot should be included at no more than 60° from the meshing point. By employing these shroud guidelines Winfree was able to achieve a 63.2% reduction in WPL running in two phase at an oil spray rate of 5 gallons/minute.

Currently the most extensive experimental spiral bevel gear windage research has been conducted by Johnson et al [2, 7, 9, 23]. In the first study [7] a spiral bevel crown gear was mounted in a bespoke test rig capable of rotation up to 15,000 RPM. A staged investigation was conducted in order to separate the various physical phenomena:

- Configuration 1: Unshrouded or open.
- Configuration 2: Shrouded with no control of mass flow rate (natural case).
- Configuration 3: Shrouded with prescribed mass flow rate.

An image of the test rig is presented in Figure 2.1. The basic rig allowed the addition of various shrouds and, for Configuration 3, an air flow conditioning hardware, facilitating a range of possible air inlet pressures. Shroud static pressures were measured using 36 1mm diameter pressure tapings drilled normal to the inner surface of the shroud.

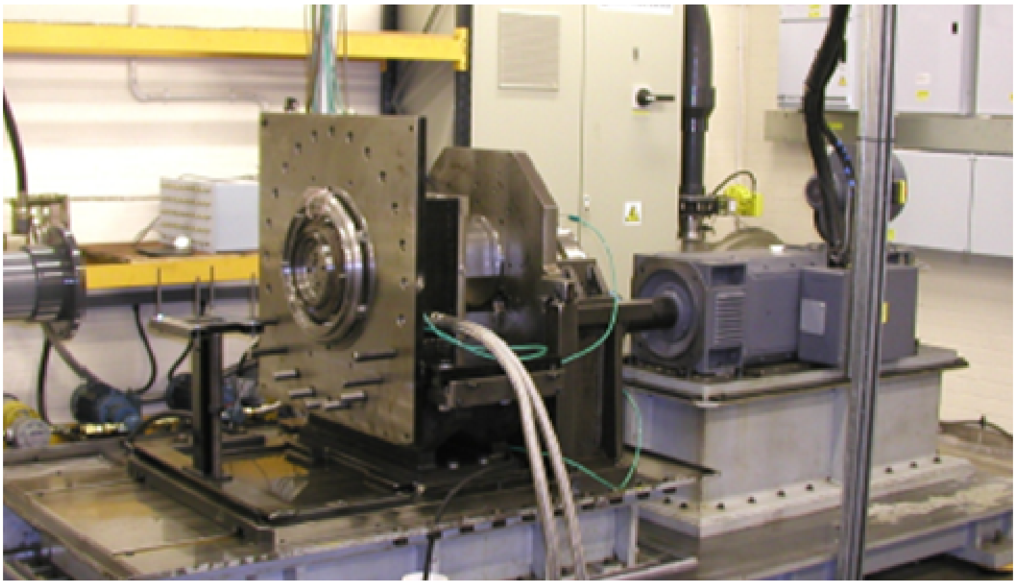

Figure 2.1: Image showing Johnson's gear windage test rig [7]

In all testing WPL data was presented in non-dimensional form using torque coefficient C_m which is defined as

$$C_m = \frac{T}{\frac{1}{2}\rho r^5 \omega^2} \tag{2.3}$$

Here T is the measured windage torque, r is the outer radius of the gear and ω is the gear rotational speed.

From configuration 1 Johnson observed that C_m values were largely constant with some increase at higher rotational speeds. For C_m to remain constant Johnson concluded T must approximately scale with the square of the speed. It was also seen that approximately 25% less torque was required when rotating the gear anti-clockwise. This was thought to be a result of flow separation within the teeth valley from blades angling against the flow of air, reducing the gears pumping effect and thereby reducing WPL. From this an analogy can be made between a spiral bevel gear and a centrifugal fan. This implies that a means of reducing WPL in spiral bevel gears could be to apply design conditions which would create as ineffective a centrifugal pump as possible.

By adding a shroud to the gear and running under free pumping conditions (where no mass flow rate was artificially set) Johnson was able to draw three main conclusions. Firstly a significant 75% reduction in WPL was observed for the clockwise rotating case. Secondly the trend for shrouded C_m values is similar to the trend for unshrouded C_m values, showing an increase at higher rotational speeds. Thirdly there is no significant difference between C_m values for shrouded gears running in clockwise or anti clockwise rotations, as previously noted by Winfree [8]. This data is displayed in Figure 2.2. This work, as well as work by Webb [24], described in Section 2.2.2, was the basis of detailed shroud design guidelines as published by Morvan [25].

For the third test condition, controlling the mass flow rate through the gear, Johnson found that C_m increased with mass flow rate. The lowest torque observed occurred at a near zero mass flow rate. This implies that a restricted shroud inlet to minimise air flow would be beneficial, agreeing with previous works by both Dawson [22] and Winfree [8].

Johnson extended this work by including an oil phase [2]. The existing rig was modified to include pumps and scavenge within a transparent containment chamber to accommodate the oil flow which could be applied at up to 5 l/min.

Running the gear unshrouded with an oil phase led to an expected increase in

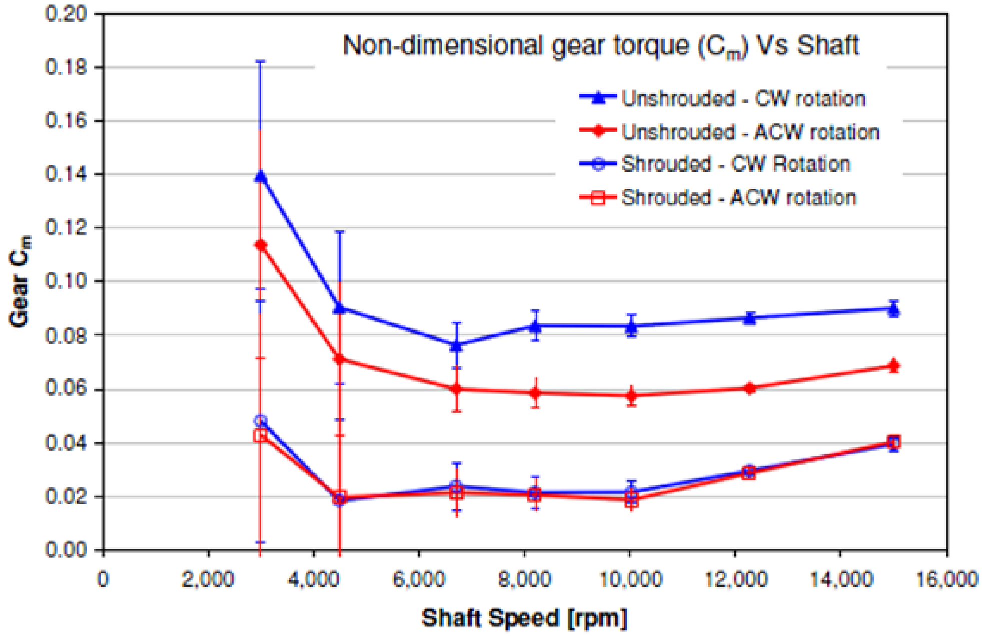

Figure 2.2: Graph showing Johnson's data for non-dimensional moment coefficient against shaft speed for a shrouded and unshrouded gear. Both rotational directions are included [7]

torque, which Johnson was able to very accurately model by analogy to a turbo machine. Here the tangential force on the gear is equal to the oil mass flow rate times the change in whirl velocity, which is the tangential component of the velocity of the working fluid. In this case, the inlet whirl velocity is assumed to be zero and the outlet whirl velocity is the peripheral speed of the gear at its outer radius. Calculated in this way the force acts at the outer radius thus giving the equation

$$T_{oil} = \dot{m}_{oil}\omega r_{gear}^2 \tag{2.4}$$

where $\dot{m}_{oil}$ is the oil mass flow rate (kg/s), ω is the gear rotational speed (rad/s) and r is the outer radius of the gear (m).

For a shrouded gear however there are two key problems. The first is that oil can be ingested into the gear, even a small amount of oil ingestion results in significant torque increases, reducing the beneficial effects of shrouding. Ingestion is made worse by oil pooling in the sump and can be limited by effective shroud inlet design.

The second problem is oil trapped under the shroud being drawn down the underside of the shroud by a torroidal vortex and recirculated. This recirculation results in a much greater perceived torque. Similar to Winfree's work [8], Johnson identified the need to effectively scavenge oil trapped under the shroud. Five shrouds with single slots located in various positions were used and their effects on WPL measured. A shroud with slot 17° from the oil jet and 26° width, designated shroud A, and one 5° from the oil jet and 61° width, designated shroud B, were the two most effective. It is important to note that these were the two shrouds with slots closest to the oil jet, implying that quickly scavenging the oil from the shroud is most beneficial and that oil recirculation has a significant effect on WPL.

A key conclusion from Johnson's work is that there are several mechanisms of WPL associated with two phase gear windage. It is known that meshing losses between a gear and pinion can be minimised by including a lubricating oil phase however, due to the negative effects of oil acceleration and recirculation, it is beneficial to minimise the amount of oil introduced and limit the chance of oil ingestion. An IGB model could help to address both of these issues by tracking oil transport both in the main chamber and under the shroud.

Recent work reported in Simmons et al. [26] extended previous work by investigating the effect of pressure within the chamber. The effect of varying the amount of oil supplied to the chamber was also studied. The test rig was significantly modified by the addition of a pressure chamber and oil feeds. Three configurations: unshrouded crown gear, shrouded crown gear and finally shrouded crown and pinion were investigated.

Data for the shrouded crown gear when plotted as C_m against rotational Reynolds number appeared to show a trend similar to that found by Yamada and Ito [27] for the rotating cone case with two regimes separated by a transition region, illustrated in Figure 2.3. However the data set was very sparse and conclusions are only tentative at this stage. Making comparisons between a spiral bevel gear and a rotating cone suggests it is likely that similar $C_m - Re$ curves might exist for a gear, dependant on non-dimensional flow rate C_q. It was also observed that C_m appears to be independent of Re beyond Re numbers of 2×10^6, though the author suggest more data is required to support these hypotheses.

The experimental work of the Transmission UTC provides a source of validation data for the current study. There is very little quantitative data, largely torque values plus some pressure data for the ambient case, so it is likely that validation will be mostly qualitative and based on bulk quantities.

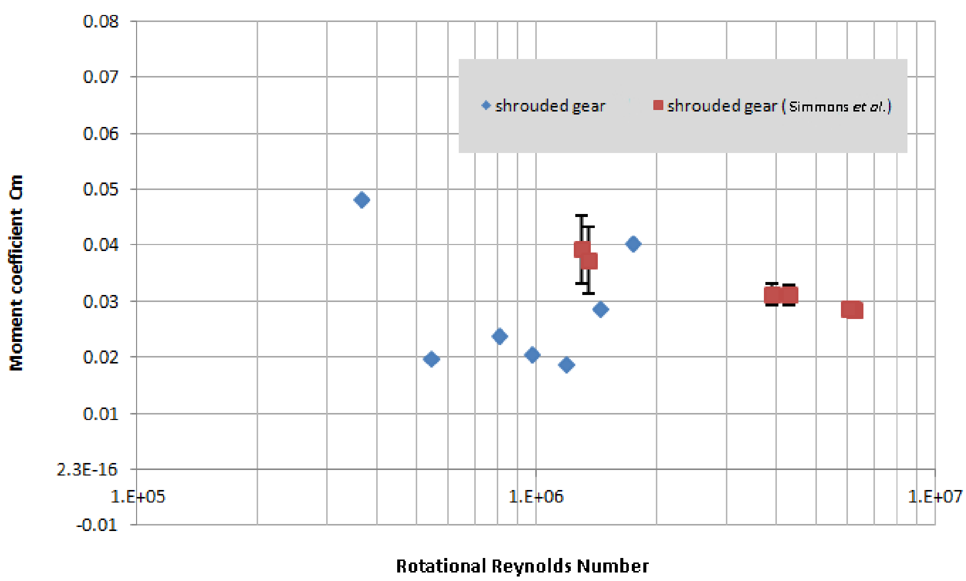

Figure 2.3: Logarithmic scale graph showing moment coefficient against rotational Re number for a shrouded gear, taken from experimental work in Simmons et al. [26]

2.2.2 CFD

Work by Rapley et al. [28] investigating the application of CFD to model spiral bevel gear windage has been conducted parallel to Johnson's [7] experimental work and uses this data for validation. Rapley used two main geometries running under steady state conditions. The first, an unshrouded gear, contained 961,751 cells. The second modelled a shrouded gear with a prescribed mass flow rate, as dictated by a mass flow inlet. This model contained up to 2,200,000 cells. Assuming the gear to be axisymmetric, a one tooth slice of the domain was created corresponding to a 3.96° segment. Periodic boundary conditions were then set. In both cases the models used rotating frames of reference to simulate the gear rotation. The k-ϵ RNG turbulence model was selected due to its reported strength at modelling strongly swirling flows and both standard and enhanced wall treatments were tested. Both wall function treatments were tested on the same mesh, which is of limited value as only one of these treatments would be valid for a give mesh depending on it's y^+ values.

For the unshrouded case rotating in either direction, Rapley was able to simulate very similar trends to Johnson's experimental data, however the CFD model consistently under predicted the torque by 25-28%. Very little difference was seen between the cases run using standard or enhanced wall conditions though Rapley's model had high y^+ values of over 25 [29] and so this could be expected. The shrouded case showed much better comparison to experimental results with both torque and pressure data.

Similar to his rotating cone work, as detailed in Section 2.3.2, Rapley found that steady state modelling was inadequate. Evidence suggesting the need for a transient approach was that C_m values did not adequately settle, exhibiting classic hunting behaviour. Transient cases were then run for the shrouded gear model and periodic transient fluctuations in C_m are clearly evident, as can be seen in Figure 2.4. No analysis comparing the steady and transient simulations was undertaken and so the root of this apparent transient behaviour is unknown. For the transient case, good agreement with experimental data was observed for a rotational speed of 8,203 RPM however again an under prediction of torque was observed for the model running up to 15,000 RPM. No mesh independence was conducted for this rotational speed.

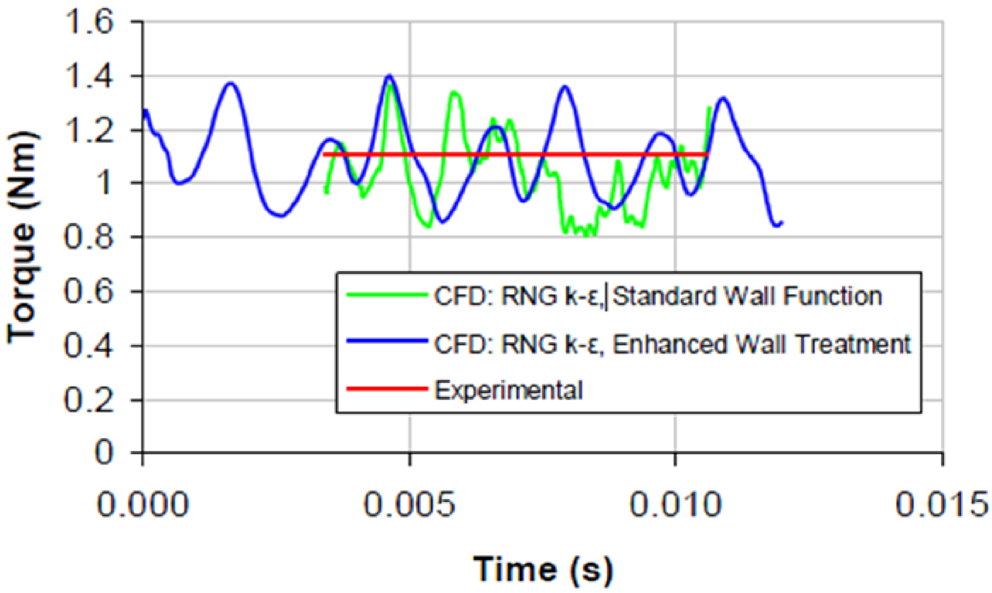

Figure 2.4: Graph of Gear torque against time showing the transient fluctuation in Rapley's work [28]

Based on his shrouded bevel gear model, Rapley [30] extended this initial work to investigate the effects of shroud variations and their effect on WPL. The same single tooth segment gear model was used with parametric shroud variations in the inlet (1.5-4mm), outlet (2.52-4mm) and face clearances (0.25-1.5mm). A similar set up to Rapley's previous transient work was used, selecting standard wall functions for this case. Only 700,000 cells were used in the domain; later work by Webb [24] suggests that this is not enough to provide a mesh independent solution. Therefore Rapley's results should be considered with caution, though the general trends are likely to be correct.

The main conclusion from this investigation is that small variations in some aspects of shroud geometry have significant effects on WPL. In all cases Rapley found restricting the shroud inlet, and thus the flow through the teeth, had a beneficial effect on WPL. This was expected based on previous literature. Reductions in WPL of 46.7% were made in reducing the inlet from 4 mm to 1.56 mm for example. Reducing face clearance however had the opposite effect, a 15.5% increase in torque at 0.25 mm was observed. This shows that it is possible to detrimentally over restrict the flow above the gear teeth.

A complete collection of Rapley's spiral bevel gear work is contained within his thesis [29]. This work demonstrated the potential of CFD to qualitatively model shrouded bevel gears in single phase.

A more robust development of Rapley's parametric work was conducted by Webb [24, 31, 32] and consisted of two separate stages, a gear based study and a shroud based study. Firstly Webb investigated the effect parametric changes in gear geometry would have on the windage [24, 31, 32]. Since it is very costly to create multiple IGB standard gears, a CFD analysis is very beneficial as a wide number of variables can easily be studied without the associated time and expense.

For this work, Webb created a gear model using Pro/Engineer 2.0 and from data provided by a Gleason data sheet[1]. This geometry was very similar to that used by Rapley however the parametric nature of the model meant that Webb [31] could automatically generate new gears by altering several variables, including the total number of teeth, the face width, cone angle, and tooth circular pitch. Webb's work [24] focussed on changing the tooth module, showing the effect of varying the number of teeth a gear has whilst maintaining a constant diameter.

[1]Gleason are one of the spiral bevel gear manufacturers' and their gear sheet provides details as to how a gear is cut and what geometry it will have.

The CFD methodology used by Webb is similar to that of Rapley [28]. A pressure inlet and outlet boundary condition was used to allow the mass flow rate to be as 'natural' as possible. A rotating frame of reference was used to simulate gear rotation at 12,266 RPM. The k-ϵ RNG model for turbulence was used with standard wall functions and all discretisation schemes were second order. All simulations were run transiently from a converged steady state model. A key difference was that Webb's mesh independence study demonstrated a need for a minimum of 250,000 cells in the tooth valley alone. The lack of available computational resources limits the use of the model to gear sectors of only a few teeth at a time and means that modelling a full spiral bevel gear this way is currently out of the question.

Webb's control model was validated against Johnson's experimental work. Figure 2.5 shows that though there is a difference of around 14% between experimental and CFD data for the gear torque the trend of increasing torque with mass flow rate is clearly present. Webb reports the gradients of the graph are within 0.8%. Figure 2.6 is a plot of the mean static shroud pressure and matches very well with the experimental data with only a 100Pa difference across the face of the shroud. Webb concluded his model was suitably validated and used it as a base for a parametric study.

The first conclusions of this study were that increasing the number of teeth decreases windage loss. Using a control gear with 91 teeth, Webb found a WPL decrease of 15% when the number of teeth was increased to 110. Similarly there was an increase of 8% when the number of teeth was reduced to 80. The reason behind this is that as the number of teeth increases, the tooth valleys become smaller and the gear approaches the geometry of a rotating cone. From Dawson's [22] work it is known that rotating cones display a lower WPL than rotating gears.

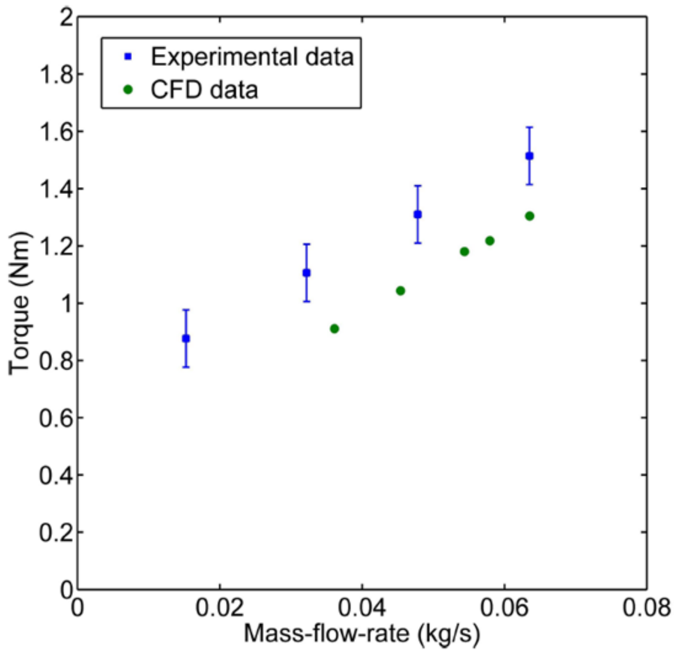

Figure 2.5: Changes in gear torque with mass flow rate through the gear. CFD data is from Webb [24] and experimental data is from Johnson [7].

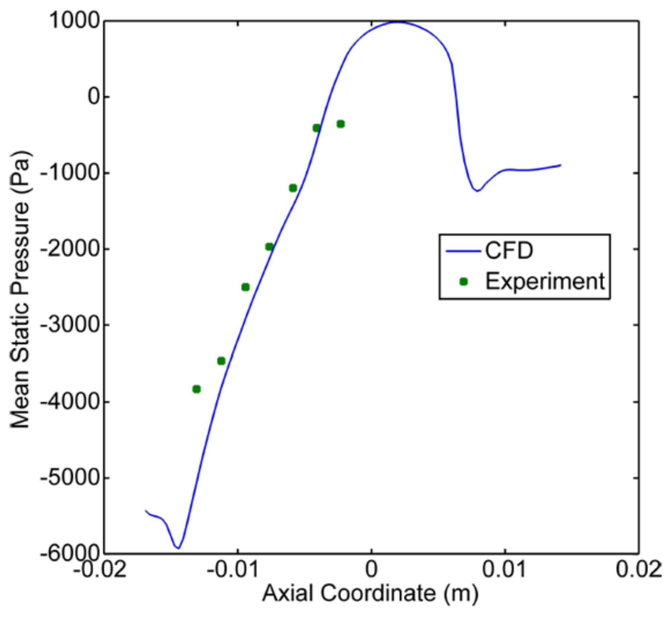

Figure 2.6: Mean static pressure profiles along the shroud. CFD data is from Webb [24] and experimental data is from Johnson [7]

A study to investigate the possible variation in modelling one tooth, three teeth and five teeth was also conducted [24,31]. Webb found that there was a maximum variation in C_m of 4.51% which was observed between the one and five teeth cases. For the other teeth cases there was a variation of 2.24% for two teeth and 2.09% for three teeth. Further investigation on the five tooth case identified that though time averaged static pressure values on the shroud matched well with a single tooth case, at individual time steps structures could be seen spanning multiple teeth. This behaviour is lost when modelling only a single tooth. Webb found that C_m values on the teeth flanks for consecutive teeth vary by only 1-2% and thus concluded that these structures ran solely across the shroud and had minimal impact on the flow in the tooth valleys. Consequently Webb concluded that it was acceptable to continue modelling a single tooth, justified by the significantly lower computational costs and relatively low variations in C_m. This is a significant conclusion for the current study showing that it is only necessary to model a single tooth in order to capture the relevant flow physics, though this may be dependent on other variable such as the shroud gap.

Webb extended this work in his thesis [24] in which he also studied the effect of changing outer diameter (and so a change in face width), inner diameter and gear pitch cone angle. The conclusion of this was that increasing the outer diameter resulted in an increase in WPL proportional to diameter to the power of 4.32. Varying the inner diameter did not appear to have any consistent results and no relationship was suggested. However Webb did find a 6% reduction in WPL for a case with a 20% smaller inner diameter. Finally Webb showed that a decrease in pitch cone angle will give an increase in WPL, a reduction from 60.83° to 55° resulted in 4.5% increase. The opposite was seen when increasing the pitch cone angle. This was attributed to a larger pressure component in this case.

Secondly Webb investigated the effects of windage for several theoretical shroud shapes [24]. This directly continued Rapley's shroud study but was not merely limited to varying the shroud's distance from the gear. As a baseline case Webb modelled his shroud on the design used by Johnson et al. [7] and an inlet passage was included in line with this work. From this case he designed an additional four variations in shroud inlet geometry and assessed the effect of each on WPL. He concluded that adding a nose to the shroud, as proposed by Johnson, can reduce WPL by further restricting the flow into the gear teeth. No other variation in geometry was able to improve on this. Even more effective is a sudden contraction at the inlet down to 1.5 mm. Increasing the inlet passage length was also seen to reduce WPL by increasing the resulting pressure drop.

Webb also looked at shroud outlet geometry. Five outlet geometries were modelled including the control shroud which had the most restricting geometry. These can be seen in Figure 2.7. As mentioned in previous literature by both Dawson [22] and Winfree [8], the most restrictive outlets showed the lowest torque values, all of the outlet variants producing torque between 4.81% and 12.3% greater than the control shroud. This work was conducted in single phase and Webb notes that the more defined air flow away from the gear present in more open outlets might be beneficial in extracting oil in two phase flow. This avoids recirculation of oil and the significant power losses associated with it.

Finally Webb investigated the complex flow behaviour under the shroud and conducted preliminary two phase studies on particles injected into the domain [32]. A discrete particle model (DPM) was implemented to simulate oil droplet injection under the shroud. Using his previous CFD methodology [31], Webb included an escape discrete phase boundary condition for all walls, inlets and outlets. This removes a particle as soon as it comes into contact with the boundary and notes its departure variables. Though this is not physical behaviour it removes the need for a complex film model and Webb deemed it sufficient for initial work monitoring oil impact sites.

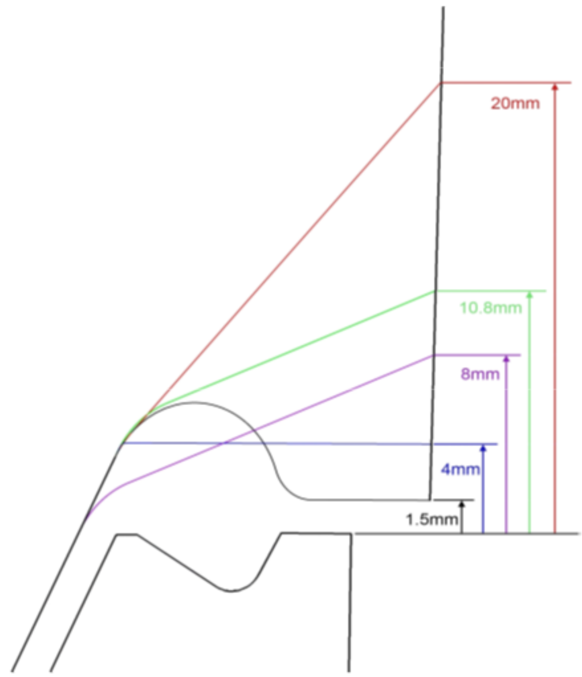

Figure 2.7: Comparison of shroud outlet shapes tested by Webb [24]. The control case is shown in black

Oil was injected at two locations, the shroud inlet and the gear tip. At the shroud inlet Webb found that, due to the low axial velocity of the flow, particles of a size larger than 3.5 microns were more likely to hit the underside of the shroud than to follow fluid streamlines. This is specific to Webb's shroud which includes a shroud nose to restrict the flow. Such behaviour would potentially create a film. Smaller particles were more likely to follow streamlines and be ingested into the teeth as a result. Injections at the gear tip were designed to replicate oil shedding from the gear. Webb showed that particles were likely to be flung onto the underside of the shroud radially out from their injection location. He noted that this occurred with little sensitivity to injection conditions, concluding that confidence in this behaviour was high and also that there was a high likelihood of a film forming as a result of this.

No validation for this work was available due to a lack of available experimental data, Webb stating the complexity of the flow as the cause. However Johnson's work [2] has shown some circumstantial evidence of similar oil behaviour and recirculation Figure 2.8.

As previously mentioned, Webb's work, as well as the works of Johnson, forms part of detailed shroud design guidelines drafted by Morvan [25].

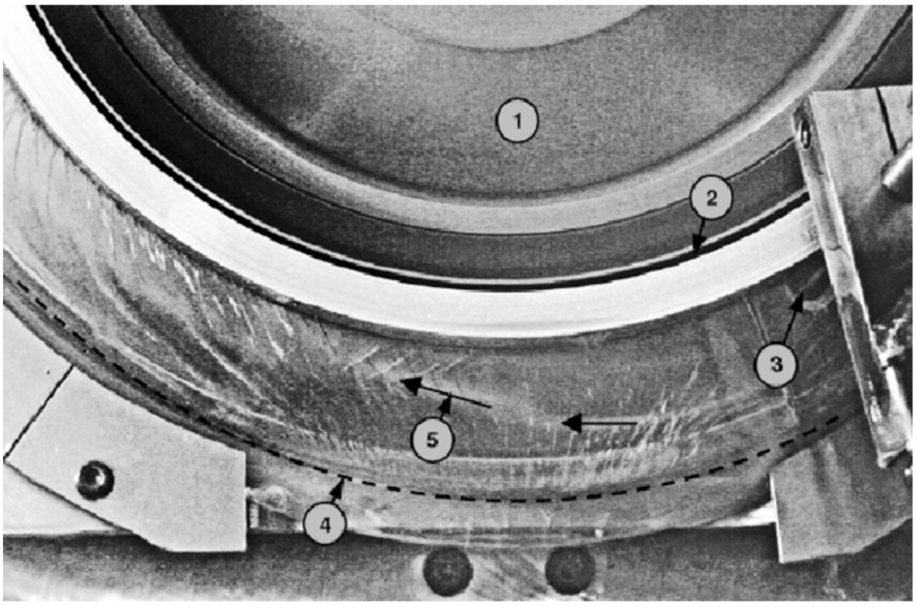

Figure 2.8: Oil streak under the shroud at 5000 RPM. 1: crown gear; 2: shroud inlet; 3: into-mesh oil jet; 4: gear outer diameter; 5: path of oil under the shroud [2]

The majority of computational investigations into meshing gears has focused on spur gear pairs. Strasser [33] has investigated CFD modelling of a mixing pump, which is in essence two meshing spur gears. In this 2D investigation Strasser used a deforming mesh with 65,000 cells to model the meshing region. Using a deforming mesh allows the cells to agglomerate or be created to maintain a specified skewness and maintain mesh quality. Strasser also used an Eulerian mixture model to simulate the injection of a second additive phase with some success.

Similar to Strasser's work, Li [34] also modelled meshing spur gears using a 2D deforming mesh to simulate gearbox lubrication flows under dip conditions. Concurrent experimental work was conducted as validation for the model. The gear configuration consisted of a 40 tooth crown gear with radius 60 mm and a 20 tooth pinion gear with a radius of 30 mm. Two rotational speeds were tested, 1,200 RPM and 325 RPM. The k-ϵ RNG model was used as was the Volume of Fluid multiphase model to simulate the lubricating oil phase. Li found that the WPL was significantly influenced by the rotational speed, increased speed resulted in greater oil churning and an associated increase in power loss. This was also true for an increase in immersion depth.

Whilst both Strasser and Li were able to successfully simulate a spur gear mesh using a deforming mesh both their works are limited to 2D. Extending this work to 3D results in a substantial computational expense, both with the number of cells required and with the increase in complexity of the deforming mesh calculation. It also remains to be seen how these multiphase models would cope for faster rotating gears. The spiral bevel gears modelled in this thesis typically rotate at 12,000 RPM, 10 times faster than those used in Li's work. The required decrease in time step to model gears rotating at this speed adds a further expense, which makes this methodology impractical for 3D flows.

2.3 Rotating Cones

Webb's work has essentially shown that a full IGB CFD model with geometrically accurate spiral bevel gears is beyond current computing capability. A simplified representation of the gear would be a beneficial tool without the associated computational cost. As an approximation, spur gears have often been modelled as simple rotating disks and the equivalent of this for bevel gears is a rotating cone. There has been extensive research done on the flow properties of rotating cones and the relevant previous research is reviewed here.

2.3.1 Experimental

There have been several papers by Yamada and Ito [27, 35, 36] experimentally investigating the frictional resistance of shrouded rotating cones. The first using an enclosed rotating cone [35], demonstrated the relation of non-dimensional moment coefficient C_m and rotational Reynolds' number Re_{rot}, followed by investigation into cone roughness effects [36] and finally the inclusion of an axial throughflow between cone and shroud [27]. Due to pumping effects, axial flow is present in shrouded gear flows so the focus of this section will be on their final paper.

The test rig comprised a rotating cone enclosed in a shroud with the same apex angle and is depicted in Figure 2.9. The inner surface of the shroud is parallel to the surface of the cone and the gap width between the two can be varied. Through flow was able to enter the clearance through an opening at the shroud apex and discharges through ports at the top of the shroud. In this experiment the liquid used was water. A torque pick up with four strain gauges was used to determine the torque on the cone. Both shroud and cone were modular and several cones with varying apex angles were tested.

Yamada and Ito [27], measured C_m with changing Re_{rot}. This was repeated for several different non-dimensional flow rates C_q, shroud gap width ratio's (s/R_c) and cone apex angles θ. The definitions of these parameters are given in Equations 2.5, 2.6 and 2.7:

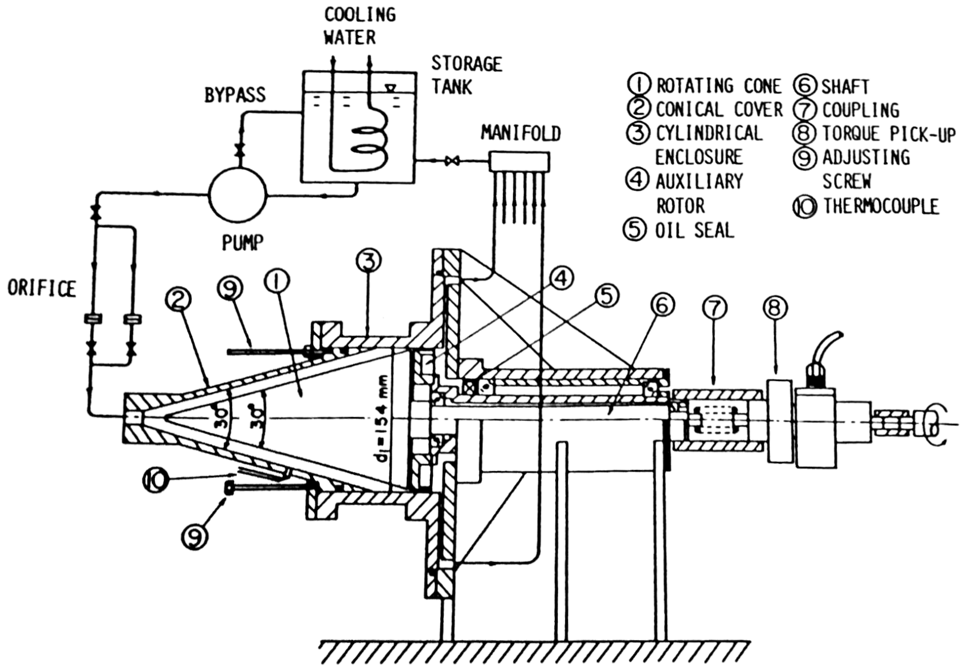

Figure 2.9: Image depicting the experimental rig used by Yamada and Ito [27]

$$C_m = T\frac{sin(\frac{\theta_c}{2})}{\frac{1}{2}\rho\omega^2 R_c^5} \tag{2.5}$$

$$Re_{rot} = \frac{R_c^2\omega}{\nu} \tag{2.6}$$

$$C_q = \frac{Q}{R_c\nu} \tag{2.7}$$

The conclusion of this study was the identification of three separate flow regimes as can be clearly seen in Figure 2.10. The first, up to Re_{rot} of around 10^5, corresponds to a laminar region where the authors believe Taylor vortices do not exist in this case. This region is extended when some throughflow is introduced. It is believed that this throughflow suppresses the otherwise destabilising vortices.

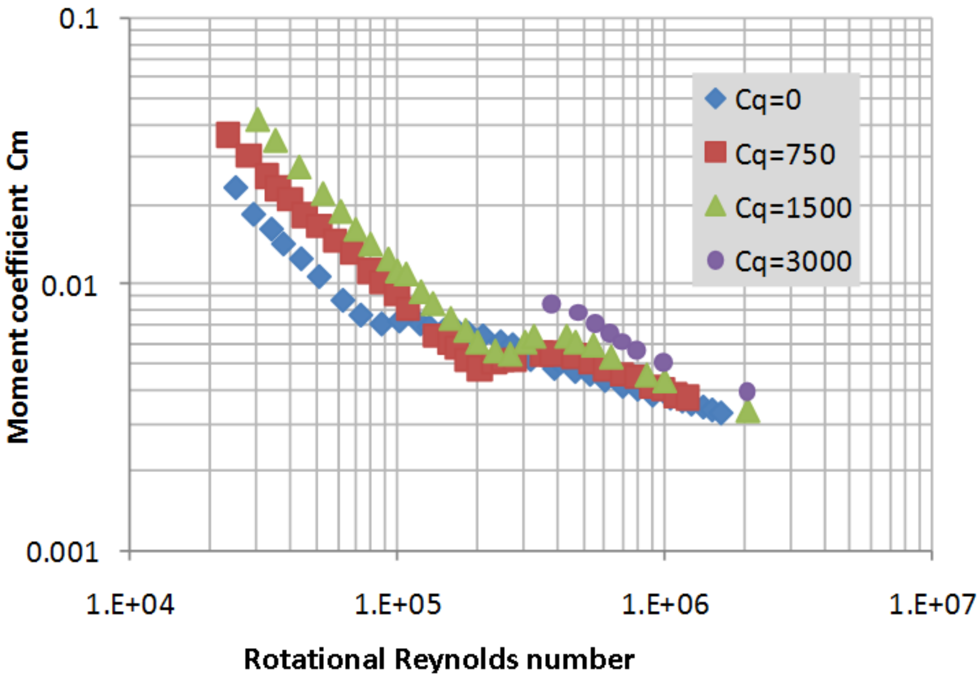

Figure 2.10: Experimental data from Yamada and Ito (graphed by Simmons et al [26]) showing variation of torque coefficient C_m with rotational Reynolds' number

The second transitional region occurs as an intermediate stage between laminar and turbulent regions, the Re_{rot} at which this occurs is the critical Re number. Here a sharp rise in C_m is observed with increasing Re_{rot}, the magnitude of this rise depends on both C_m and θ_c.

The final region is a full turbulent region which occurs at high Re_{rot} numbers typically above 10^6. In this region C_m again decreases as Re_{rot} increases. Here C_m is less sensitive to changes in Re_{rot} and also the non dimensional face clearance (s/R_c). This implies that at very high Re_{rot} numbers, as experienced in gear tooth flows, the gap width will have only a small effect. However it is also important to note that gap width ratio has a determining effect on when the flow transitions to turbulent.

Of key importance to rotating cones is the development of Taylor vortices. Taylor vortices are counter rotating, axisymmetric toroidal vortices which occur between a rotating surface and a stator such as a shroud. There has been a very large volume of work on Taylor flows. Of particular note is work by Wimmer [37] and Noui-Mehidi [38]. Wimmer discovered that in the case of rotating cones, Taylor flow has three dimensional effects and can travel through an enclosed system without any external throughflow. Noui-Medihi's own investigations on Taylor flow showed that elongated vortices can reach lengths up to 2.4 times the size of the shroud gap width, giving them considerable influence on the flow in this region. In particular, Rapley stated that these recirculations suppress the pumping effect of the gear and therefore lower the mass flow rate of the system [29].

2.3.2 CFD

Rapley [39] conducted work aiming to recreate the results of Yamada and Ito [27] using CFD. His model was a simplified representation of the experimental apparatus used by Yamada and Ito, principally in 2D steady state, and several parametric changes were made to the model to test varying gap widths and apex angles, θ_c, as in the informing experimental work. Multiple turbulence models were tested in order to find one most suited to the experimental data, including the k-ϵ, k-ϵ RNG, SST k-ω and the RSM models. A mass flow inlet was used to control the throughflow rate.

Initially Rapley modelled $C_q = 0$ for a no throughflow condition. For $\theta_c = 120°$ poor correlation was obtained using both RNG and SST models, over approximating C_m by 16-70%. However results for $\theta_c = 90°$ using the RNG turbulence model were considerably better, achieving a low error of 0.6-17%.

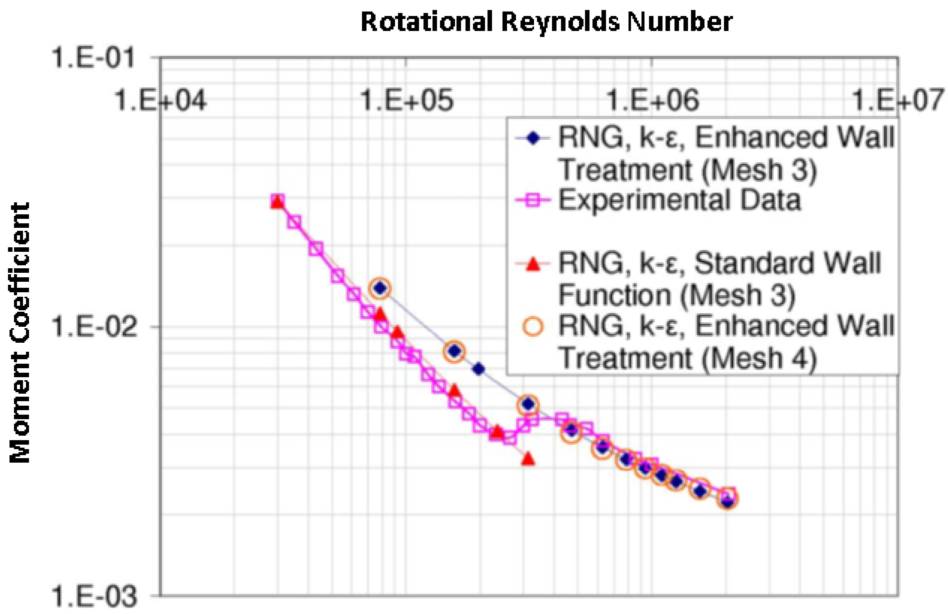

Figure 2.11: Graph of moment coefficient against rotational Reynolds number for a rotating cone. The graph shows Rapley's work [39] comparing his data with Yamada and Ito's experimental results [27]. Vertex angle = 90°, non dimensional gap width = 0.008 and non dimensional throughflow = 1,500

For cases where a throughflow was introduced Rapley observed a strong correlation between turbulence models and individual flow regimes. For example the RNG model with enhanced wall functions produced accurate results when modelling the turbulent flow which occurs at high Re_{rot} again with an error of 0.6-17%. However no individual model was able to accurately model all three regimes and no model at all was able to capture the transitional region. This is shown in Figure 2.11 taken from Rapley's work comparing his data with Yamada and Ito's experimental results [27]. These results are unsurprising as neither standard nor enhanced wall functions are valid within the transitional region and turbulence models are not valid within the laminar region which occurs for flows with Re_{rot} below 10^5 in this case. While Rapley states that all meshes have been adapted for enhanced wall functions to ensure $0 < y_* < 4$, no value was stated for the y_* values when using standard wall functions. Consequently some doubt must be cast over the appropriateness of the use of these models for low Re_{rot} flows.

Rapley suggested the reason for the modelling inaccuracies were that the problem was inherently three dimensional, therefore unable to be captured in a 2D simulation. He went on to extend this work with two 3D models, one a 6° slice of a cone and shroud, and the other a full 360° model. Using these models there were some minor improvements in accuracy. The k-ϵ RNG model used for the turbulent flow regime improved error to 0.2-11% but was still unable to model the transitional region. Flow visualisations demonstrate the three dimensional behaviour of the flow and explain the increase in accuracy from the 2D models. It is known that the transitional region between laminar and turbulent regimes is unpredictable and inherently impossible to capture using RANS formulated turbulence models therefore it is again unsurprising he was unable to predict this transition region.

The primary focus of Rapley's work was a shrouded spiral bevel gear and here he did extend his work to include transient flows, finding transient behaviour of vortices under the shroud.

2.4 Gear Tooth Submodel

In order for a cone to adequately represent a rotating gear momentum sources must be applied to the air flow to mimic the driving action of the teeth. Previous, promising, work on momentum sources and their application to rotating cones is reviewed in this section, largely comprising the preliminary work informing this project.

Momentum sources have been used in turbomachinary applications in the past, one such example being to simply model a hydro kinetic turbine in the work of Gaden and Bibeau [40]. Here they were able to replace the complex turbine rotors with a single momentum source subregion. In this application the source region was used to extract momentum from a free flow to represent the energy extracted by a turbine. The source term was calculated using the equation:

$$\frac{\partial s}{\partial t} = C_s \frac{\rho u^2}{2l} \tag{2.8}$$

where s is the momentum per unit volume removed from the fluid, C_s is the momentum source factor (a constant related to the coefficient of thrust of the turbine, and varied between 0 and 20), u is the local velocity and l is the stream-wise length of the turbine region.

This model was based upon a turbine with radius 1.2 m (approximately 9 times larger than the maximum gear tip radius used in this thesis) and validated against the Betz theory, which states that a turbine cannot extract 100% of the energy from a free stream. Turbine efficiency η is defined as the ratio between the power produced by the turbine W and the power of the undisturbed freestream through the same area that is swept by the turbine rotor W_∞.

$$\eta = \frac{W}{W_\infty} \tag{2.9}$$

The turbine efficiency is plotted against the velocity ratio for the momentum source CFD model and the Betz theory (see Figure 2.12) and a good correlation was discovered between the two. Gaden and Bibeau reported a consistent 5% over prediction of the turbine efficiency.

This project aims to model the driving action of the teeth using a momentum

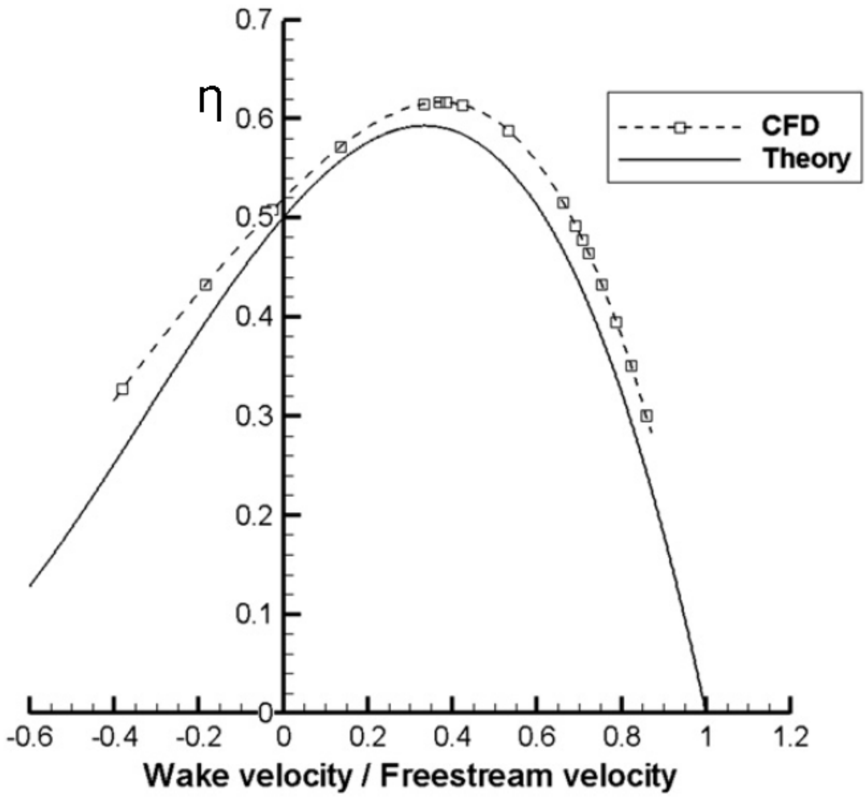

Figure 2.12: Graph plotting the turbine efficiency η and velocity ratio for a momentum source CFD modelled hydro kinetic turbine and theoretical results. Image originally from Gaden and Bibeau [40].

source driven rotating cone model in place of a spiral bevel gear. Work by Kay [41] has shown this goal is feasible and he had success in replicating some of Webb's results [24], replacing the gear geometry with that of a rotating cone and fluid sub-region. Momentum sources were added in this sub-region extending out from the surface of the cone which can be seen in Figure 2.13.

Figure 2.14 shows plots of static pressure along the shroud for both Webb's model and Kay's momentum source model. Kay attempted to match all key flow characteristics which were seen in Webb's model. Though he was able to match bulk flow properties through the teeth and those at the outlet, it was not possible to match the recirculation observed at the shroud inlet. This can

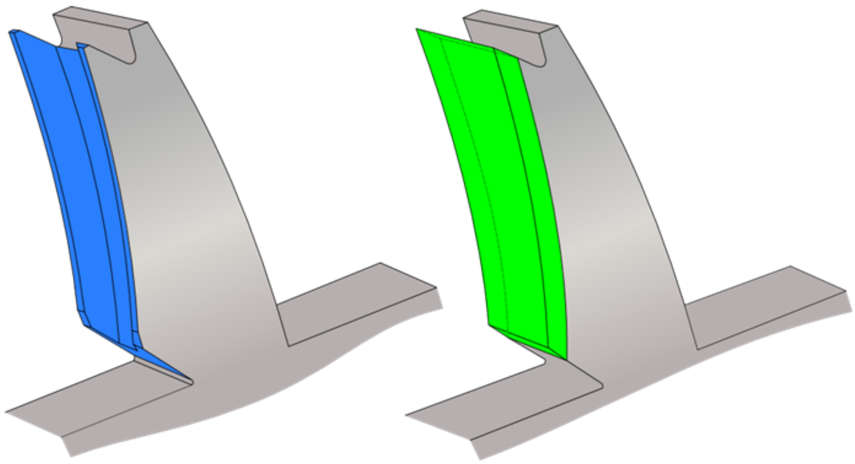

Figure 2.13: Diagram showing the replacement of the full tooth geometry (blue) with the cone and momentum source fluid sub region (green). Image originally from Kay [41]

be seen on Figure 2.14 between points 0.2 and 0.4 on the shroud as a region of low pressure. It appears that this is outside the control of a momentum source region located downstream of the recirculation.

Kay's study did not go as far as investigating the potential effects inlet swirl may have on the simulation though he had started to characterise the azimuthal velocities created by the rotating gear.

The present work aims to model a gear by using momentum sources to mimic the average effect of the gear teeth on the flow. For the gear case the "tooth effects" dominate C_m. With a cone the wall turbulence is a key driver in the C_m behaviour, as described in Section 2.3, though this characteristic is removed when a calibrated momentum source is added to account for the time-average pumping effect a gear would apply. The latter implies that C_m cannot be derived from the cone and momentum source model.

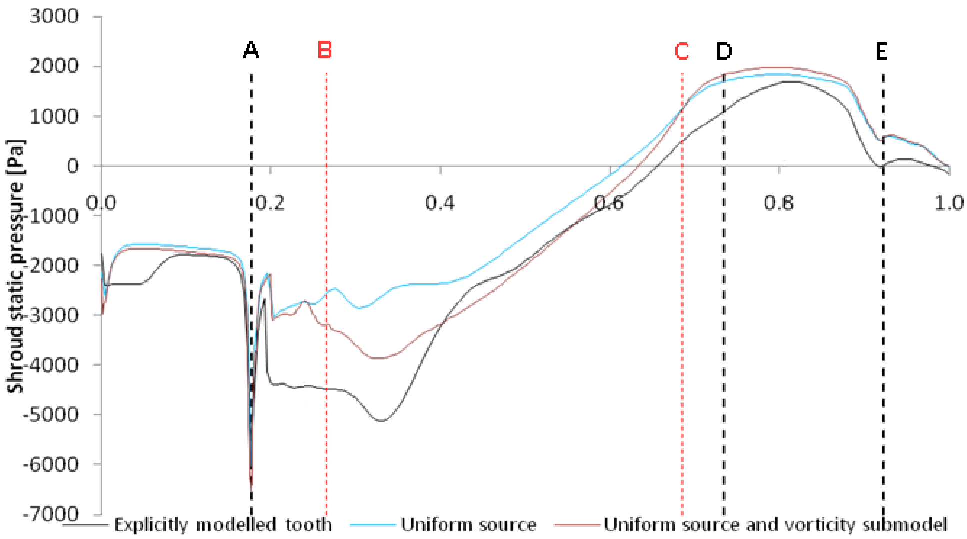

Figure 2.14: Graph showing the comparison of static pressure at non dimensionalised points along the shroud for an explicitly modelled tooth and two momentum source models. Point A is equivalent to the shroud nose, point B is the beginning of the momentum source sub-region, point C is the end of the momentum source sub-region, point D is the beginning of the shroud gutter and point E is the beginning of the shroud restriction. Taken from Kay [41]

.

2.5 Summary

This section has reviewed the current ability of full engine modelling and complex chamber modelling, and shown that significant progress can be made in these areas.

As the base of an IGB modelling approach, a review of spiral bevel gear pairs has been conducted. Experimental work on both spur gears and bevel gears has shown a correlation between changing gear parameters and windage power loss. Shrouding a gear has been shown to reduce gear windage and significant flow restriction at the inlet is most effective means to achieve this. As a consequence of this it is important that any future modelling involve shrouded gears. The interaction between gears and shrouds is a key issue, especially when an oil phase is introduced. An analogy between a spiral bevel gear and a centrifugal fan has also been made.

CFD modelling of a spiral bevel gear has been reviewed and a parametric study on the changes in WPL due to changing gear and shroud parameters has been discussed. This study showed that CFD is capable of replicating experimental results in single phase, with limited research on the oil phase. An appropriate CFD methodology for modelling bevel gears in the current project has been derived from this work.

Extensive work has been done in the area of rotating cones, in particular on the flow which forms between the cone and shroud. The ability of CFD to model such a flow has also been reviewed.

Early work on the use of momentum sources to model a spiral bevel gear has been covered, as well as considering the applicability of previous cone modelling techniques to a cone with momentum sources.

Chapter 3

CFD Methodology

This chapter outlines the fundamental equations employed by commercial CFD codes as well as the more advanced models used within this thesis. This information is detailed and expanded upon for reference in the FLUENT Theory Guide [42]. All models follow the methodology described here unless otherwise stated in the relevant chapter.

The commercial CFD code FLUENT [1] versions 12.0, 13.0 and 14.5 were used throughout this work. CFD codes use numerical algorithms to calculate fluid flows through a defined domain. FLUENT uses a finite volume method and divides the domain into control volumes or cells. Defining the flow properties at the domain boundaries allows flow variables to be calculated within these control volumes, typically using iterative finite differencing methods. Once converged a solution to the flow field can be analysed.

3.1 Navier-Stokes Equations

The Navier-Stokes equations are derived by applying Newton's Second Law to fluid motion and govern the fluid flow of a Newtonian fluid. They describe unsteady, three-dimensional fluid flow.

Continuity and momentum equations are defined as follows:

$$\frac{\partial \rho}{\partial t} + \nabla \rho \overrightarrow{v} = 0 \tag{3.1}$$

$$\frac{\partial (\rho \overrightarrow{v})}{\partial t} + \nabla(\rho \overrightarrow{v} \overrightarrow{v}) = -\nabla p + \nabla(\overline{\overline{\tau}}) + \rho g + S_M \tag{3.2}$$

The derivation of these equations are widely available, an example of which can be found in Versteeg and Malalasekera [43]. The term S_M accounts for additional sources of momentum and could include user applied momentum sources or transferred momentum from dispersed phases. $\overline{\overline{\tau}}$ is the stress tensor and defined as:

$$\overline{\overline{\tau}} = \mu[(\nabla \overrightarrow{v} + \nabla \overrightarrow{v}^T) - \frac{2}{3}\nabla \overrightarrow{v} I \tag{3.3}$$

There is an additional equation to calculate energy and this is described as:

$$\frac{\partial}{\partial t}(\rho E) + \nabla(\overrightarrow{v}(\rho E + p)) = \nabla(k_{eff} \nabla T + (\overline{\overline{\tau}}_{eff} \overrightarrow{v})) + S_h \tag{3.4}$$

where E is defined:

$$E = h - \frac{p}{\rho} + \frac{v^2}{2} \tag{3.5}$$

In Equation 3.4, k_{eff} is effective conductivity and $\overline{\overline{\tau}}_{eff}$ is the effective dissipation, both of which are defined by the selected turbulence model (see Section 3.7). S_h represents additional volumetric heat sources as well as heat transferred to the fluid from external sources.

3.2 Spatial Discretisation

The continuous flow field is calculated by storing values at nodes within each cell control volume, a method known as discretisation. Using the finite volume method, FLUENT first converts the Navier-Stokes equations to algebraic equations which can be numerically solved. For a control volume V the transport equations for scalar quantity ϕ can be written in integral form as:

$$\int_V \frac{\partial \rho\phi}{\partial t} dV + \oint \rho\phi \overrightarrow{v} \cdot d\vec{A} = \oint \Gamma_\phi \nabla\phi \cdot d\vec{A} + \oint_V S_\phi dV \tag{3.6}$$

Γ_ϕ is defined as the diffusion coefficient for scalar quantity ϕ and S_ϕ are its source terms. This is essentially the relation between the left hand side convection terms and right hand side diffusion terms.

The discretisation of Equation 3.6 for a given cell volume gives the following:

$$\frac{\partial \rho\phi}{\partial t} V + \sum_f^{N_{faces}} \rho_f \overrightarrow{v}_f \phi_f \cdot \vec{A}_f = \sum_f^{N_{faces}} \Gamma_\phi (\nabla\phi)_n \cdot \vec{A}_f + S_\phi V \tag{3.7}$$

The subscript f refers to the faces of the control volume and N_{faces} the number of faces on the cell. Equation 3.7 therefore expresses the net flow of the scalar quantities through the cell. This non-linear equation can be linearised to:

$$a_P \phi = \sum_{ab} a_{nb} \phi_{nb} + b \tag{3.8}$$

Linear algebraic equations are written for each cell and a matrix of coefficients is formed. FLUENT then solves this using a coupled algebraic multigrid (AMG) method and a Gauss-Seidel linear equation solver.

Due to the non-linearity of the equations, changes in ϕ need to be controlled to ensure the iteration process remains stable. This is achieved using under-relaxation factors, γ, which restrict the change in ϕ between iterations. Per iteration ϕ is therefore calculated as:

$$\phi_{new} = \phi_{old} + \gamma \Delta \phi \tag{3.9}$$

FLUENT has predefined values for γ though these can be easily modified within the code. Under relaxation factors for momentum and energy were set to 0.4 and 0.7 respectively as recommended by Webb [24] as these values were found to assist convergence.

As FLUENT stores variables at the centroid of each cell, face values of each cell must be calculated using a discretisation scheme. In all cases within this thesis a first-order or second-order upwind scheme was used. The first-order upwind scheme simply assumes that the cell centroid is the average of the variables within the cell. Face variable values are therefore taken to be equal to the centroid of the neighbouring upstream cell and is the simplest discretisation scheme.

A well known drawback to using the first order scheme is it can cause excessive numerical diffusion, notably when the flow does not align with the discretised grid lines. There are several cases within this thesis for which numerical diffusion could be a problem and so the second-order upwind scheme was used. This scheme uses a Taylor expansion about the cell centroid and calculates the face value, ϕ_f as:

$$\phi_f = \phi + \nabla\phi \cdot \Delta\vec{s} \tag{3.10}$$

ϕ is the centroid value, $\nabla\phi$ is the gradient from the upstream cell and $\Delta\vec{s}$ is the displacement vector from the centroid of the upstream cell to the face of the present cell. The gradient $\nabla\phi$ is calculated using the divergence theorem as follows:

$$\nabla\phi = \frac{1}{V}\sum_{f}^{N_{faces}} \widetilde{\phi_f}\vec{A} \tag{3.11}$$

$\widetilde{\phi_f}$ is the average scalar value at the two faces.

Other higher order discretisation schemes, such as QUICK, were not considered on the recommendation of Lee [44] who found no significant improvement in solution accuracy for meshes of similar densities to those used in this thesis.

3.3 Temporal Discretisation

Though some models within this thesis are modelled in steady state, most are calculated transiently. The need to capture transient phenomena was identified by both Rapley [29] and Webb [24]. As a result of this it is necessary to use temporal discretisation to calculate the flow field with respect to time. An iterative calculation is made for every timestep significantly increasing the associated computational expense. A benefit of the cone model is that it can be run in steady state at significantly reduced computational cost.

First order temporal discretisation is found using the following equation:

$$\frac{\phi^{n+1} - \phi^{n}}{\Delta t} = F(\phi) \tag{3.12}$$

Second order discretisation is calculated as:

$$\frac{3\phi^{n+1} - 4\phi^{n} + \phi^{n-1}}{2\Delta t} = F(\phi) \tag{3.13}$$

Again, second order discretisation was used in this work. Transient simulations use a steady state solution as the initial condition. Transient parameters vary depending on the case and are described throughout the thesis where appropriate. Each time step is limited to a maximum of 50 inner iterations though typically each time step converges within 25 iterations.

3.4 Pressure-Velocity Coupling

FLUENT contains two different methods for solving the flow field, the density-based solver and the pressure-based solver. The density-based solver solves all the governing equations (continuity, momentum and energy) simultaneously and iteratively due to non-linearity. However there are some limitations to using the density based solver, primarily restrictions on the multiphase models that can be used in conjunction with it. Neither the Volume of Fluid (VOF) nor the Eulerian model are available within the FLUENT code for the density based solver. As a result the pressure-based solver was used in this thesis.

The pressure-based solver calculates the flow field by solving for pressure through a manipulation of the continuity and momentum equations. Here, a segregated approach is used where the governing equations are solved sequentially and independently of one another. An initial pressure is guessed and corrected from the continuity equation, and then used to correct initial guesses for the velocities. This process is repeated until all variables have converged.

There are several models available to achieve this coupling and in the present work the Semi-Implicit Method for Pressure-Linked Equations (SIMPLE) algorithm [45] was used.

3.4.1 Rotating Reference Frame

Some of the work within this thesis employs a rotating reference frame to simplify the post processing of calculated data.

Under normal conditions, the rotating domain is observed from a static position and as a result the rotating teeth makes the solution unsteady and changes the shape of the domain with respect to time in the process. This makes post processing the data very difficult.

Using a rotating reference frame, the domain is observed from a rotating position moving at the same speed as the rotating surfaces. As a result the domain is fixed and does not change shape with respect to time. The difference between both cases is purely in how the solution is observed and so calculated pressures and velocities are identical. This method does require some changes in boundary conditions and this is explained where applicable.

3.5 Convergence

In this work, convergence for both steady and transient models is determined by three methods. Firstly scaled residuals are monitored until they have iterated to a set value, secondly the mass flow rates into and out of the model are monitored to ensure mass balance and thirdly the non-dimensional torque coefficient C_m on the rotating surfaces is measured until it is judged to be at a steady level.

Unscaled residuals R^ϕ are calculated from the imbalance from Equation 3.8 and summed over all the cells in domain. This is then scaled by the flow rate of ϕ through the domain and defined as

$$R^\phi = \frac{\sum_{cellsP} | \sum_{nb} a_{nb}\phi_{nb} + b - a_P\phi_P}{\sum_{cellsP} |a_P\phi_P} \tag{3.14}$$

Typically scaled residuals were considered converged once they reached 10^{-5}.

C_m is monitored and summed across all rotating surfaces within the domain. The definition of C_m used in this thesis is

$$C_m = \frac{T}{\frac{1}{2}\rho r^5 \omega^2} \tag{3.15}$$

where T is gear torque, r is the outer gear radius and ω is the gear rotational speed (rad/s). C_m is considered converged when the average moment doesn't vary by more than 3% for each subsequent gear revolution.

These convergence criteria are occasionally varied and are reported in the appropriate sections.

3.6 Boundary Conditions

Part of setting up the computational domain is to define the conditions at the domain boundaries. Several different conditions were used for the models described in this thesis and these are listed in the relevant sections. This section defines the mathematical principles behind the types of boundaries used.

3.6.1 Walls

At a wall boundary, a no slip shear condition ensures that the velocity components of the fluid are fixed at either zero or the value at which the wall is moving.

It is also possible to specify a zero shear wall which allows the fluid to have a non-zero velocity at the wall. This has been used in some special cases within this work.

How wall boundary conditions interact with turbulence models is described in Section 3.7.3.

3.6.2 Pressure Boundaries

Both pressure inlets and outlets are described in this section. Pressure boundaries are used when the pressure at the location in the domain is known but velocity or flow rates are not. FLUENT requires the total pressure to be prescribed and where the energy equation is used temperature must also be specified. Total pressure for a compressible fluid is described in Equation 3.16. In most cases within this work total pressure was set at 0 Pa relative to the FLUENT operating pressure of 101,325 Pa. Temperature was set to ambient, where required.

In all cases, turbulent characteristics were defined by specifying a turbulence intensity and a hydraulic diameter. Turbulence intensity was taken to be a low value of 1% as air drawn in from the main chamber is typically of a range between 1 and 5%. A sensitivity analysis on inlet turbulence intensity between these ranges showed no perceivable impact on the simulation results.

$$p_0 = p_s \left(1 + \frac{\gamma - 1}{2} M^2\right)^{\gamma/\gamma - 1} \tag{3.16}$$

3.6.3 Mass Flow Boundaries

A mass flow rate boundary prescribes a flow rate into the domain. In this case pressure is calculated and not prescribed. For incompressible flows, mass flow boundaries are practically comparable to velocity inlets, which also calculate the total pressure at the boundary.

3.6.4 Periodic Boundaries

Periodic boundaries are defined in linked pairs so that the flow exiting one surface is identical to the flow entering the other. This is beneficial in reducing domain size where symmetry exists, in this case for a segment of a gear and circular chamber.

3.7 Turbulence

3.7.1 Turbulence Modelling

All flows described in this thesis are highly turbulent. Flow of this type is typically characterised as irregular and chaotic, which can be a challenge to model correctly. It is possible to model turbulence directly, however it requires a very small mesh size and timestep to model the smallest length and timescales of turbulence. This is often prohibitively expensive.

As an alternative, it is possible to consider the instantaneous velocity as having an average and a fluctuating component:

$$u = \overline{u} + u' \tag{3.17}$$

If the velocity terms in the Navier-Stokes equations (Equation 3.2) are replaced with Equation 3.17 the Reynolds-averaged Navier-Stokes (RANS) equations can be derived:

$$\begin{aligned}\rho\left(\frac{\partial\overline{u}}{\partial t}+\overline{u}\frac{\partial\overline{u}}{\partial x}+\overline{v}\frac{\partial\overline{u}}{\partial y}+\overline{w}\frac{\partial\overline{u}}{\partial z}\right) = -\frac{\partial p}{\partial x}+\mu\left[\frac{\partial^2\overline{u}}{\partial x^2}+\frac{\partial^2\overline{u}}{\partial y^2}+\frac{\partial^2\overline{u}}{\partial z^2}\right] \\ -\rho\frac{\partial\overline{u'^2}}{\partial x}-\rho\frac{\partial\overline{u'v'}}{\partial y}-\rho\frac{\partial\overline{u'w'}}{\partial z}\end{aligned} \tag{3.18}$$

$$\rho\left(\frac{\partial\overline{v}}{\partial t}+\overline{u}\frac{\partial\overline{v}}{\partial x}+\overline{v}\frac{\partial\overline{v}}{\partial y}+\overline{w}\frac{\partial\overline{v}}{\partial z}\right)=-\frac{\partial p}{\partial y}+\mu\left[\frac{\partial^2\overline{v}}{\partial x^2}+\frac{\partial^2\overline{v}}{\partial y^2}+\frac{\partial^2\overline{v}}{\partial z^2}\right] -\rho\frac{\partial\overline{u'v'}}{\partial x}-\rho\frac{\partial\overline{v'^2}}{\partial y}-\rho\frac{\partial\overline{v'w'}}{\partial z} \quad (3.19)$$

$$\rho\left(\frac{\partial\overline{w}}{\partial t}+\overline{u}\frac{\partial\overline{w}}{\partial x}+\overline{v}\frac{\partial\overline{w}}{\partial y}+\overline{w}\frac{\partial\overline{w}}{\partial z}\right)=-\frac{\partial p}{\partial z}+\mu\left[\frac{\partial^2\overline{w}}{\partial x^2}+\frac{\partial^2\overline{w}}{\partial y^2}+\frac{\partial^2\overline{w}}{\partial z^2}\right] -\rho\frac{\partial\overline{u'w'}}{\partial x}-\rho\frac{\partial\overline{v'w'}}{\partial y}-\rho\frac{\partial\overline{w'^2}}{\partial z} \quad (3.20)$$

From these equations six additional terms become evident, termed the Reynolds stresses. Three normal stresses:

$$\tau_{xx}=-\rho\overline{u'^2},\tau_{yy}=-\rho\overline{v'^2},\ \tau_{zz}=-\rho\overline{w'^2} \quad (3.21)$$

and three shear stresses:

$$\tau_{xy}=\tau_{yx}=-\rho\overline{u'v'},\tau_{xz}=\tau_{zx}=-\rho\overline{u'w'},\tau_{yz}=\tau_{zy}=-\rho\overline{v'w'} \quad (3.22)$$

As there are now more terms than equations to solve them it is necessary to use turbulence models to predict the Reynolds stresses to close the equations. The Boussinesq hypothesis can be used to simplify this process and proposes that Reynolds stresses are proportional to the mean rate of deformation. This can be defined as:

$$\tau_{ij}=-\rho\overline{u_i'u_j'}=\mu_t\left(\frac{\partial U_i}{\partial x_j}+\frac{\partial U_j}{\partial x_i}\right)-\frac{2}{3}\rho k\delta_{ij} \quad (3.23)$$

where $k = \frac{1}{2}(\overline{u'^2} + \overline{v'^2} + \overline{w'^2})$, μ_t is the turbulent viscosity and δ_{ij} is the Kronecker delta. $\delta_{ij} = 1$ if $i = j$ and $\delta_{ij} = 0$ if $i \neq j$.

The Boussinesq hypothesis assumes that the turbulent viscosity, μ_t, is isotropic and that the ratio of Reynolds stresses to the mean rate of deformation is the same in all directions. In many complex flows this assumption does not hold, however typically works well for shear driven flows dominated by one of the turbulent shear stresses. The computational expense saved using this method makes it a preferable alternative to using the more costly Reynolds stress model, which solves transport equations for each of the terms in the Reynolds stress tensor. The Boussinesq hypothesis is employed in the $k - \epsilon$ group of turbulence models.

3.7.2 The $k - \epsilon$ RNG Model

Having used the Boussinesq hypothesis, RANS turbulence models are now needed to define μ_t. Within this work a variant of Launder and Spalding's [46] classic 2-equation $k - \epsilon$ model is used. The $k - \epsilon$ RNG model, as developed by Yakhot et al [47], was chosen for its strength in modelling swirled flows and work by both Rapley [29] and Webb [24] have shown it appropriate for modelling rotating gear cases.

In the standard $k - \epsilon$ model two additional transport equations for k and ϵ are introduced and these include several constants such as the turbulent Prandtl numbers σ_k and σ_ϵ. These transport equations combined are used to calculate turbulent viscosity as follows:

$$\mu_t = \rho C_\mu \frac{k^2}{\epsilon} \tag{3.24}$$

The constant $C_\mu = 0.0845$ is used as default in the RNG model as it has been empirically found to fit a wide range of engineering flows.

The $k - \epsilon$ RNG model is based on Renormalization Group theory and includes several refinements to the classic model:

- An extra term, R_ϵ, in the ϵ equation improves accuracy for rapidly strained flows
- The effect of swirl on turbulence is included
- An analytical formula is used to drive Prandtl numbers

The RNG modified transport equations for k and ϵ are respectively:

$$\frac{\partial(\rho k)}{\partial t} + \nabla(\rho k \overrightarrow{v}) = \nabla[\alpha_k \mu_{eff} \nabla k] + G_k + G_b - \rho\epsilon - Y_M + S_k \tag{3.25}$$

$$\frac{\partial(\rho \epsilon)}{\partial t} + \nabla(\rho \epsilon \overrightarrow{v}) = \nabla[\alpha_\epsilon \mu_{eff} \nabla \epsilon] + C_{1\epsilon}\frac{\epsilon}{k}(G_k + C_{3\epsilon} G_b) - C_{2\epsilon}\rho\frac{\epsilon^2}{k} - R_\epsilon + S_\epsilon \tag{3.26}$$

Here μ_{eff} is effective viscosity and is defined as $\mu_{eff} = \mu + \mu_t$. Calculating k and ϵ allows μ_t to be found and thus used to solve the Reynolds equations described in Equations 3.18, 3.19 and 3.20.

Constants are defined within FLUENT as $C_{1\epsilon} = 1.42$ and $C_{2\epsilon} = 1.68$.

From Equation 3.25 the term G_k represents the production of kinetic energy, G_b the effects due to gravity (not modelled in the work presented here), Y_M the reduction in kinetic energy due to compressibility and S_k the addition of kinetic energy from other source terms.

Additionally, from Equation 3.26 the term S_ϵ defines the addition of dissipation from other source terms and R_ϵ, as previously specified, improves accuracy for rapidly strained flows. This is achieved by increasing the value of ϵ in regions of high flow and is calculated as:

$$R_\epsilon = \frac{C_\mu \rho \eta^3 (1 - \eta/\eta_0)}{1 + \beta \eta^3} \frac{\epsilon^2}{k} \tag{3.27}$$

where $\eta \equiv Sk/\epsilon$, $\eta_0 = 4.38$, $\beta = 0.012$.

All $k - \epsilon$ group models assume that the flow is fully turbulent. For all cases in this thesis Re_{rot} is above 10^6, which is in the fully turbulent region. Since the flow is well out of the transitional region RANS modelling is appropriate. The RNG model is capable of modelling lower Re number flows but this is dependant on correct handling of the near wall region.

As referred to in Equation 3.4 the selected turbulence model determines the calculation of two terms in the energy transport equation. These are the effective thermal conductivity k_{eff} and the stress tensor $\overline{\overline{\tau}}_{eff}$. The RNG model defines these as

$$k_{eff} = \alpha c_p \mu_{eff} \tag{3.28}$$

and

$$\overline{\overline{\tau}}_{eff} = \left(\mu_{eff} \left[(\nabla \overrightarrow{v} + \nabla \overrightarrow{v}^T) - \frac{2}{3} \mu_{eff} \nabla \overrightarrow{v} I \right] \right) \tag{3.29}$$

where $\mu_{eff} = \mu + \mu_t$ and α is the inverse Prandtl number.

3.7.3 Wall Functions

Close to the wall, within the boundary layer, there is a viscous sublayer in which molecular viscous forces dominate. This means that the $k - \epsilon$ assumption that the flow is fully turbulent no longer holds. As a result, it is necessary to either employ a model integrated with the turbulence model to correctly predict near wall behaviour or to use a very fine mesh and resolve the flow all the way down to wall using modified turbulence models which are valid within this region. In the first instance these models are called wall functions and can represent a saving in computational expense as less dense meshes can be used in the near wall region.

Wall functions use relationships which are dependant on the position of the cell within the near wall region and this position is determined using a non-dimensional indicator, y^+. This is defined as

$$y^+ = \rho u_\tau y / \mu \tag{3.30}$$

where y is the distance of the cell centroid from the wall, μ is the dynamic viscosity of the fluid and the friction velocity u_τ is defined

$$u_\tau = \sqrt{\frac{\tau_w}{\rho}} \tag{3.31}$$

FLUENT in fact uses a different relationship, y^*, to determine cell position. In practice this is very similar to y^+ at positions close to the wall and is calculated as

$$y^* = \frac{\rho C_\mu^{0.25} k_P^{0.5} y_P}{\mu} \tag{3.32}$$

where k_P is the turbulent kinetic energy at the near wall node P and y_P is the distance from point P to the wall. For a cell to be out of the viscous sublayer it must have a $y^* > 11.225$.

Standard Wall Functions

The standard wall function available in FLUENT is based on the work by Launder and Spalding [46]. Depending on a cell's y^* value two different relationships are used to determine mean non-dimensional velocity. For $y^* < 11.225$ (within the viscous sublayer):

$$U^* = y^* \tag{3.33}$$

and for $y^* > 11.225$ (outside of the viscous sublayer):

$$U^* = \frac{1}{k} ln(Ey^*) \tag{3.34}$$

where k is the von Karman constant = 0.4187 and E is a constant = 9.793. Nondimensional velocity is

$$U^* = \frac{U_p C_\mu^{0.25} k_p^{0.5}}{\tau_w/\rho} \tag{3.35}$$

FLUENT's standard wall functions have limited reliability in cases which exhibit low Reynolds number flow or severe pressure gradients. In such cases FLUENT recommends using enhanced wall treatment, which is described in the following section.

Enhanced Wall Treatment

For cases where meshes are necessarily fine near the wall in some regions, or for flows where the standard wall functions have been previously described as being limited, enhanced wall treatment offers improved accuracy with the flexibility of not requiring a fine mesh in all near wall regions.

Between the viscous sublayer and fully turbulent flow there exists a buffer region within which neither Equation 3.33 nor 3.34 holds. FLUENT defines this region as $3 < y^* < 10$. For cases where mesh density necessitates that y^* values fall into this range, enhanced wall treatment can be used to provide a better representation of turbulence variables and velocity profiles by blending the equations for the viscosity affected near wall region and the fully turbulent region.

For fine meshes, where $y^* \approx 1$ the standard two layer approach is employed to find ϵ and turbulent viscosity μ_t in the near wall cells. This is achieved by dividing the domain into two distinct regions using Re_y where

$$Re_y \equiv \frac{\rho y \sqrt{k}}{\mu} \tag{3.36}$$

Here k is turbulent kinetic energy, μ is dynamic viscosity and y is the wall-normal distance from the cell centres. y is defined

$$y \equiv \min_{\vec{r}_w \in \Gamma_w} \|\vec{r} - \vec{r}_w\| \tag{3.37}$$

where $\vec{r}$ is the position vector at the field point and $\vec{r}_w$ is the position vector at the wall boundary. Γ_w is the union at the wall boundaries.

For cells in the fully turbulent region where $Re_y > Re_y^*$ the chosen turbulence model is used. For cells in the viscous affected region where $Re_y < Re_y^*$ the one equation Wolfschtein [48] model is used to calculate $\mu_{t,2layer}$ and ϵ_{2layer} and the momentum and k equations are the same as in the chosen turbulence model. The critical value of Reynolds number is $Re_y^* = 200$.

$$\mu_{t,2layer} = \rho C_\mu l_\mu \sqrt{k} \tag{3.38}$$

$$\epsilon_{2layer} = \frac{k^{\frac{3}{2}}}{l_\epsilon} \tag{3.39}$$

Length scales l_μ and l_ϵ are calculated

$$l_\mu = yC_l^*(1 - e^{-Re_y/A_\mu}) \tag{3.40}$$

$$l_\epsilon = yC_l^*(1 - e^{-Re_y/A_\epsilon}) \tag{3.41}$$

Where constants are defined by Chen and Patel [49] as $C_l^* = kC_\mu^{-3/4}$, $A_\mu = 70$ and $A_\epsilon = 2C_l^*$.

Enhanced wall treatment then blends the equations for $Re_y < 200$, $\mu_{t,2layer}$ and ϵ_{2layer}, with the equations for $Re_y > 200$, μ_t and ϵ. For μ_t this is as follows as proposed by Jongen [50]

$$\mu_{t,enh} = \lambda_\epsilon \mu_t + (1 + \lambda_\epsilon)\mu_{t,2layer} \tag{3.42}$$

where blending function λ_ϵ is defined

$$\lambda_\epsilon = \frac{1}{2}[1 + tanh(\frac{Re_y - Re_y^*}{A})] \tag{3.43}$$

and A is a constant which determines the width of the blending function

$$A = \frac{|\Delta Re_y|}{artanh(0.98)} \tag{3.44}$$

A similar process is used to blend ϵ_{2layer} and ϵ.

To calculate momentum and energy equations, enhanced wall treatment blends the laminar ($Eq.$3.33) and turbulent ($Eq.$3.34) equations together using Kader's function [51] defined as

$$u^+ = e^{\Gamma} u^+_{lam} + e^{\frac{1}{\Gamma}} u^+_{turb} \tag{3.45}$$

where the blending function Γ is defined as

$$\Gamma = -\frac{a(y^+)^4}{1 + by^+} \tag{3.46}$$

and constants $a = 0.01$ and $b = 5$.

The benefits of this treatment is that one wall law can be used for the entire wall region. In addition the effects of pressure gradients are included.

Throughout this thesis standard wall functions have been employed as advised by Webb [24]. Some cases were switched to enhanced wall treatment as required by y^* values. This has been noted where appropriate in later chapters.

3.8 Multiphase Models

3.8.1 The Discrete Phase Model

Within FLUENT [42] the discrete phase model (DPM) is a Lagrangian method whereby a dispersed phase (oil in this case) is solved by tracking point particles or parcels, which occupy a low volume fraction, through a continuous fluid phase (air in this case). A low volume fraction is typically considered to be less than 10-12% and under the shroud a volume fraction of 3% is expected making this condition valid. DPM can be used to represent droplets or packets of them. The droplets and the continuous phase can be coupled which allow them to exchange momentum mass and energy for an associated computational cost.

A droplet trajectory is determined by integrating the force balance acting on the droplet as follows:

$$\frac{du_p}{dt} = \frac{18\mu}{\rho_p d_p^2}\frac{C_D Re}{24}(u - u_p) + F_x \tag{3.47}$$

The subscript p relates to particle variables where u is the fluid phase velocity, u_p is the particle velocity, μ is the molecular viscosity of the fluid, d_p is the particle diameter, Re is the relative Reynolds number and C_D is the drag coefficient.The term F_x relates to other forces acting on the particle, which can include Saffman and Brownian forces as well as the force due to the pressure gradient in the continuous phase and the force due to accelerating the fluid around the particle [42]. An additional gravity term can be applied to equation 3.47. None of these were included in any of the simulations in this work.

In this case the relative Re number and C_D are defined as:

$$Re = \frac{\rho d_p |u_p - u|}{\mu} \tag{3.48}$$

$$C_D = a_1 + \frac{a_2}{Re} + \frac{a_3}{Re^2} \tag{3.49}$$

where a_1, a_2 and a_3 are constants which apply over several ranges of Re given by Morsi and Alexander [52]. For the range $10,000 < Re < 50,000$ $a_1 = 0.5191$, $a_2 = -1662.5$ and $a_3 = 5.4167 \times 10^6$ for example.

For two way coupled formulations momentum can be exchanged between the discrete and continuous phases. This momentum exchange through a control volume is calculated using

$$F = \sum \left(\frac{18\mu C_D Re}{\rho_p d_p^2 24} (u_p - u) \right) \dot{m}_p \Delta t \tag{3.50}$$

This force term is then added as a source term to the continuous phase momentum equation. In the current work DPM iterations were set to take place every 10 continuous phase iterations. This is less often than in Webb et al [32] where DPM iterations were calculated every 2 continuous phase iterations. The particle trajectories are closely linked to the continuous phase so more frequent DPM iterations provide a more accurate solution, however computational constraints made less frequent DPM iterations more suitable for the current work.

Following Webb's methodology [32] droplets were injected using a Rosin-Rammler size distribution on all simulations unless a uniform droplet size is specified. This assumes an exponential relationship between droplet diameter, d, and the mass fraction of droplets with diameters greater than d. This mass fraction Y_d is calculated as follows:

$$Y_d = e^{-(d/\overline{d})^{n_s}} \tag{3.51}$$

here $\overline{d}$ is the mean diameter of the injected particles and n_s is the spread parameter. As advised by Webb's work [24] these values were chosen to be 10 microns and 3.5 respectively.

At the time of modelling there were no experimental data giving droplet size distribution for the UTC gear windage test rig. Data from Karlsruhe Institute of Technology (for example [53]) suggests that the majority of droplets within an aeroengine bearing chamber will be in the range 1 to 100 microns in diameter. Webb chose values for his Rosin-Rammler distribution of mean diameter 10 microns and spread factor 3.5 giving. 20 diameters in 1-100 microns range and the same parameters have been used here unless otherwise stated. Recent work by Simmons et al [54] have shown that only droplets with a diameter of less than 10 microns are likely to be ingested by the gear. This suggests the range used in this work is slightly too high but that the mean diameter is correct.

3.8.2 The Thin Film Model

Within FLUENT, thin films can be modelled using the O'Rourke and Amsden method [55]. Once a particle impacts the wall there are four possible outcomes with this model. If the wall is at a temperature higher than or equal to the boiling temperature of the oil then the droplet will either rebound or splash. For cases where the wall temperature is below this, the droplet may spread, stick or splash. This is shown in Figure 3.1.

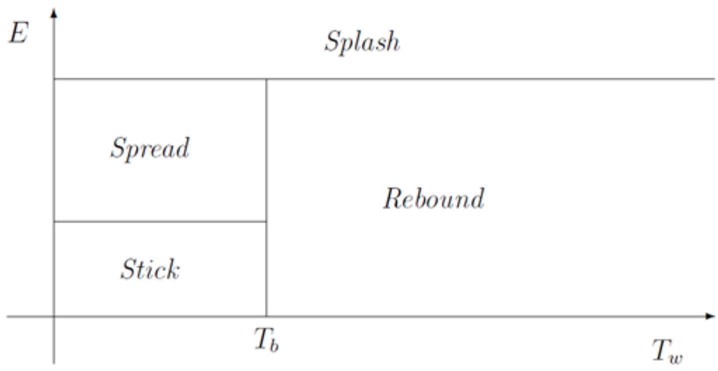

Figure 3.1: Simplified wall interaction chart for the wall film model available in FLUENT. E is the impact energy of the droplet and T_W is the wall temperature.

Where splashing occurs the droplet diameters after splashing and the splashed mass are obtained in FLUENT from the experimental data of Mundo et al [56]. This data is not valid for the splashing behaviour of high speed particles impacting a fast moving film. In this work we assume that zero splashing occurs. As the wall temperature is also far below the oil boiling temperature this leaves only spreading and sticking as possible oil impact behaviour. This is determined by the non-dimensional impact energy of the droplet, E. For E $<$ 16 sticking occurs and for E $>$ 16 spreading occurs. E is calculated as

$$E^2 = \frac{\rho_p V_r^2 D_p}{\sigma_p} \left(\frac{1}{min(h_{film}/D_p, 1) + \delta_{bl}/D_p} \right) \tag{3.52}$$

where ρ_p is the liquid density, V_r is the velocity of the particle relative to the wall velocity, D_p is the droplet diameter, σ_p is the liquid surface tension, h_{film} is the film height and δ_{bl} is the boundary layer thickness.

In this case δ_{bl} is defined as

$$\delta_{bl} = \frac{D_p}{\sqrt{Re_p}} \tag{3.53}$$

where

$$Re_p = \frac{\rho_p V_r D_p}{\mu_p} \tag{3.54}$$

There are several restrictions to using this model and these are as follows [42],

- Film thickness must be less than 500 microns,
- Heat from the wall is transferred into the film by conduction alone,
- Film temperature must be below the droplet boiling temperature.

Wall film velocity is calculated from:

$$0 = \tau_w t - \mu_p(\overline{T})\frac{u_{film} - u_{wall}}{h_{film}/2} + \dot{P}_{imp} - (\dot{P}_{imp} \cdot n)n + \dot{M}_{imp}[(u_{wall} \cdot n)n - u_{film}] \tag{3.55}$$

where τ_w is the shear stress on the gas side of the film, t is the tangent ot the surface in the direction $u_{film} - u_{wall}$, μ_p is the film liquid viscosity, $\overline{T}$ is the mean film temperature, h_{film} is the film thickness, $\dot{P}_{imp}$ is the impingement pressure, n is the unit normal pointing away from the wall and $\dot{M}_{imp}$ is the impingement mass of particles hitting the wall.

Momentum is determined by a combination of the viscous forces from the moving wall and film, the shear stress from the surrounding moving fluid and the force from impacting droplets impinging on the film.

3.8.3 The Volume of Fluid Model

The Volume of Fluid (VOF) model is an Eulerian multiphase model which allows two (or more) immiscible fluids to be solved using one set of momentum equations. Additionally, VOF tracks the volume fraction of each fluid in every cell in the computational domain and is able to determine the interface between each phase. As it only solves one set of momentum equations it is the least computationally intensive multiphase model available and is particularly effective when modelling phases with significant differences in density and a clear interface between them.

The VOF model momentum equation is calculated by

$$\frac{\partial}{\partial_t}(\rho\vec{v}) + \nabla\cdot(\rho\vec{v}\vec{v}) = -\nabla p + \nabla\cdot\left[\mu\left(\nabla\vec{v} + \nabla\vec{v}^T\right)\right] + \rho\vec{g} + \vec{F} \tag{3.56}$$

and volume fraction is tracked by

$$\frac{1}{\rho_q}\left[\frac{\partial}{\partial_t}(\alpha_q\rho_q) + \nabla\cdot(\alpha_q\rho_q\vec{v}_q) = S_{\alpha_q} + \sum_{p=1}^{n}(\dot{m}_{pq} - \dot{m}_{qp})\right] \tag{3.57}$$

where $\dot{m}_{pq}$ is the mass transfer from phase p to phase q. S_{α_q} is a source term, which for this work was equal to zero. This equation is solved for each phase apart from the primary phase, which instead is calculated by satisfying the equation

$$\sum_{q=1}^{n}\alpha_q = 1 \tag{3.58}$$

Within this thesis the primary phase is always defined as air and the only secondary phase used is oil.

Time Discretisation

The volume fraction equation can be solved by two methods of time discretisation, either the implicit or explicit scheme.

The implicit scheme requires volume fraction values at the current time step and as a result a standard transport equation can be solved iteratively for each phase (other than the primary phase). An implicit VOF approach is preferable as it generally allows larger time steps to be used than in the explicit formulation thus achieving convergence more quickly.

Alternatively, the explicit scheme requires volume fraction data from both the current and the previous time step. In this case a finite-difference interpolation scheme is employed as follows

$$\frac{\alpha_q^{n+1}\rho_q^{n+1} - \alpha_q^n \rho_q^n}{\Delta t} V + \sum_f \left(\rho_q U_f^n \alpha_{q,f}^n\right) = \left[\sum_{p=1}^{n} \left(\dot{m}_{pq} - \dot{m}_{qp}\right) + S_{\alpha_q}\right] V \qquad (3.59)$$

where $n+1$ is the index for the current time step, n is the index for the previous time step, $\alpha_{q,f}$ is the face value of the q^{th} volume fraction, V is the cell volume and U_f is the volume flux through the face.

In the current work it proved impossible to achieve convergence for this complex flow with an implicit approach and thus the explicit VOF approach was selected. Equation 3.57 is solved using an explicit time-marching scheme and the volume fraction is updated once per time step (as opposed to once per iteration).

The global time step size is allowed to vary during the simulation to aid computational stability and this is controlled by the Courant Friedrichs Lewy condition, CFL, where

$$CFL = \frac{u\Delta t_{global}}{\Delta x} \tag{3.60}$$

The CFL condition sets the maximum allowable time step for a simulation to calculate accurate results based on the mesh structure and fluid flow characteristics. For every VOF case described in this thesis the CFL is set as 2 [57] and the global time step size, Δt_{global}, varies to satisfy this condition. The explicit scheme does typically require a much smaller time step, which was found to be of the order $5\text{x}10^{-6}s$.

In addition to this, the VOF calculation uses a different time step size when calculating the volume fraction in order to improve accuracy and stability. The Courant number, C, is used in the same way as the CFL condition and for VOF simulations is set to 0.25 [57]. This method allows the volume fraction to be calculated for several time steps within each global time step.

Interface Interpolation

At the interface between phases, convection and diffusion fluxes through the control volume faces must be balanced to maintain FLUENT's control-volume formulation. For standard discretisation schemes, such as the first-order upwind or the modified high resolution interface capturing (HRIC) schemes [58], interpolation at the boundary is treated in the same way as interpolation in a cell completely filled with one phase or another.

Central differencing schemes and upwinding schemes are overly diffusive and as a result are not suitable for modelling VOF simulations as they may give unphysical results. The modified HRIC scheme available in FLUENT is an advisable alternative which non-linearly blends upwind and downwind differencing. It is a relatively cost effective means to improve accuracy over second order schemes and has been found to be more accurate than the third order QUICK scheme for VOF formulations.

An improved alternative to this is to use a special interface interpolation treatment such as the geometric reconstruction scheme. This scheme uses a linear piecewise approach which assumes that the interface in each cell has a linear slope, which is then used when calculating advection through the cell face.

There are three steps to the geometric reconstruction scheme:

1. calculate the position of the linear interface using volume fraction and its derivatives
2. calculate the advecting fluid through the face using the computed linear interface and normal and tangential velocity values
3. calculate the volume fraction in the cell using the balance of fluxes in step 2.

The geometric reconstruction scheme is more costly than the HRIC scheme and, due to the computationally expensive nature of the models simulated in this thesis, the HRIC scheme was therefore chosen for use within VOF simulations. It is possible to switch to the geometric reconstruction scheme at any point in the VOF calculation if improved accuracy is required, though this was not the case in the present work.

Surface Tension

The VOF model can include surface tension between phases at their interface. In this work, the continuum surface force model was used within FLUENT as developed by Brackbill et al. [59]. This model states that surface tension can be written in terms of the pressure jump across the surface and so a volume force is added into the momentum equation as a source term. Where there are only two different phases this force is defined as

$$F_{vol} = \sigma_{ij} \frac{\rho k_i \nabla \alpha_i}{\frac{1}{2}\left(\rho_i + \rho_j\right)} \tag{3.61}$$

In this case σ_{ij} is the surface tension coefficient, k is the curvature from the surface normal, α is the volume fraction and ρ is the volume-average density. Equation 3.61 shows that the surface tension source term is proportional to the average density in the cell.

Coupled Level Set Model

A key weakness of the VOF model is that volume fractions are discontinuous across the interface and as a result spatial derivatives are difficult to calculate. The level set method is a smooth and continuous function which means its gradients can be easily calculated. When coupled with the VOF model, the level set function tracks the fluid interface and gives an accurate estimate of both the interface curvature and surface tension as a result of curvature.

The level set function Φ calculates the normal and curvature of the interface as

$$\vec{n} = \left.\frac{\nabla\Phi}{|\nabla\Phi|}\right|_{\Phi=0} \tag{3.62}$$

$$K = \nabla \cdot \left.\frac{\nabla\Phi}{|\nabla\Phi|}\right|_{\Phi=0} \tag{3.63}$$

When the level set function is used throughout for the homogeneous multiphase model, volume conservation issues may arise; however when combined with the VOF model and used to reconstruct the curvature of the interface this weakness is overcome as VOF is strong at conserving momentum. The proposed combined approach is a very good compromise; as it is discontinuous along the interface, the VOF function alone tends to lead to inaccurate curvature computations and therefore inaccurate surface tension effects.

3.8.4 The Eulerian Model

Whereas the VOF model is beneficial for modelling two fluids with a clear interface, the Eulerian model is capable of simulating multiple interpenetrating fluids. The number of fluids and their complexity may be limited by convergence behaviour and available memory. Unlike the VOF model, the Eulerian model solves momentum and continuity equations for each phase and a single pressure term is shared by all phases. A volume fraction is determined for each phase q as follows

$$V_q = \int_V \alpha_q dV \tag{3.64}$$

and momentum and continuity are satisfied separately for each phase. Continuity for phase q for example is solved as

$$\frac{\partial}{\partial_t}\left(\alpha_q\rho_q\right) + \nabla\cdot\left(\alpha_q\rho_q\overrightarrow{v}_q\right) = \sum_{p=1}^{n}\left(\dot{m}_{pq} - \dot{m}_{qp}\right) + S_q \tag{3.65}$$

where $\dot{m}_{pq}$ is the mass transfer from phase p to phase q, α is the phase volume fraction and $\overrightarrow{v}_q$ is the phase velocity. The source term S_q is equal to zero in this thesis.

Conservation of momentum is defined as

$$\frac{\partial}{\partial_t}\left(\alpha_q\rho_q\overrightarrow{v}_q\right) + \nabla\cdot\left(\alpha_q\rho_q\overrightarrow{v}_q\overrightarrow{v}_q\right) = -\alpha_q\nabla p + \nabla\cdot\overline{\overline{\tau}}_q + \alpha_q\rho_q\overrightarrow{g} + \sum_{p=1}^{n}\left(\overrightarrow{R}_{pq} + \dot{m}_{pq}\overrightarrow{v}_{pq} - \dot{m}_{qp}\overrightarrow{v}_{qp}\right) + \left(\overrightarrow{F}_q + \overrightarrow{F}_{lift,q} + \overrightarrow{F}_{vm,q}\right) \tag{3.66}$$

The q^{th} phase stress-strain tensor $\overline{\overline{\tau}}_q$ here is defined

$$\overline{\overline{\tau}}_q = \alpha_q\mu_q\left(\nabla\overrightarrow{v}_q + \nabla\overrightarrow{v}_q^{T}\right) + \alpha_q\left(\lambda_q - \frac{2}{3}\mu_q\right)\nabla\cdot\overrightarrow{v}_q\overline{\overline{I}} \tag{3.67}$$

In Equation 3.67, μ_q represents the shear viscosity of phase q and λ_q represents its bulk viscosity. The force terms in Equation 3.66 $\overrightarrow{F}_q$, $\overrightarrow{F}_{lift,q}$ and $\overrightarrow{F}_{vm,q}$ are an external body force, a lift force and a virtual mass force respectively, all of which are equal to zero in the present work.

Fluid-Fluid Exchange Coefficient

The term $\overrightarrow{R}_{pq}$ in Equation 3.66 is an interaction force which determines the momentum exchange between phases. This is calculated with the relationship

$$\sum_{p=1}^{n} \overrightarrow{R}_{pq} = \sum_{p=1}^{n} K_{pq} \left(\overrightarrow{v}_p - \overrightarrow{v}_q \right) \tag{3.68}$$

where K_{pq} is the interphase momentum exchange coefficient defined as

$$K_{pq} = \frac{\alpha_q \alpha_p \rho_p f}{\tau_p} \tag{3.69}$$

Here, f is the drag function and τ_p the particulate relaxation time. The Schiller and Naumann model [60], which is a multi-purpose model applicable for the majority of fluid-fluid phase pairs, defines f as

$$f = \frac{C_D Re}{24} \tag{3.70}$$

and τ_p as

$$\tau_p = \frac{\rho_p d_p^2}{18 \mu_q} \tag{3.71}$$

In order to calculate τ_P a droplet diameter must be set. In all the rear chamber cases a representative d_p of 80 microns was chosen; this value was selected with reference to the work of Glahn et al. [61, 62].

As with the VOF model, an explicit time-stepping approach was employed with variable global time step to satisfy $CFL = 2$ and multiphase time step to satisfy $C = 0.25$.

3.9 Material Properties

In all cases within this thesis the fluids modelled are air and oil. The 3cSt oil used is comparable to that used by Johnson in his experimental work [2]. Unless specified otherwise, their material properties at 300 K are:

Table 3.1: Materials used within this thesis and their properties.

Material	**Density [kg/m^3]**	**Viscosity [kg/ms]**
Air	1.225	1.7894x10^{-5}
Oil	935.59	0.02774

Chapter 4

Simplified Gear Modelling Methodology

4.1 Introduction

In this chapter, a simplified modelling technique is developed to model a shrouded spiral bevel gear without the associated computational expense identified in Section 2.2.2. The approach, representing the toothed spiral bevel gear as a smooth truncated cone with momentum sources to transfer momentum to the gas as the gear teeth would do, is detailed in Section 4.2 and the model formulation is described in Sections 4.3 and 4.4. These sections also describe the formulation of a geometrically similar simulation, which is an exact representation of the physical toothed gear including teeth. This is modelled using Webb's existing gear methodology [24] and referred to throughout this thesis as a 'full tooth model'.

In Section 4.5 the 'full tooth model' will be used to calibrate the developed 'momentum source model' in single phase.

This work is then extended to two phases using the discrete particle model (DPM). Firstly the behaviour of the full tooth model in two phase is analysed. This is then used as validation for the two phase momentum source model.

The performance of the momentum source model in both single and two phase is then evaluated in Section 4.6.

4.2 Momentum Source Approach

In this section, a modelling approach is proposed and developed in which a simplified representation based on a truncated cone with additional momentum sources replaces the detailed geometry of the spiral bevel gear. This approach facilitates the creation of a full 360° gear representation and thereby aids the development of an IGB modelling strategy.

In the momentum source approach the gear tooth geometry is not explicitly modelled but the effect of the teeth on the flow is simulated by adding an extra term in the governing equations in the tooth region. This extra term is a source of momentum equivalent to that produced by the gear teeth (an extra forcing term). Calibrating the source term against a full tooth model of a small sector of the gear will allow flow features such as pressure distribution and momentum generation in the tooth valley to be captured, at least at system level, as if it had been explicitly modelled.

The benefit of such an approach is that a very fine mesh is no longer needed in the gear tooth region significantly reducing model mesh density and calculation time. In addition, it is theorised that, due to the stabilising effect of the momentum sources, the model could be run in steady state as opposed to transiently which further reduces calculation time. As a result, a momentum source model for a four tooth sector could be run in a matter of hours as opposed to the equivalent full tooth simulations which take approximately a week. This time-saving opens the possibility of modelling a full 360° shrouded gear and in the future, incorporating a pinion. The viability of this approach is explored in Section 4.4.2.

In the momentum source model the detailed tooth geometry is not reproduced and instead a smooth shrouded rotating cone is modelled. A decision was made by Kay [41] to maintain the flow area in the momentum source model the same as in the actual geometry and so the diameter of the cone is larger than the tooth root diameter. The source term model is constructed such that an additional (external) force term is added in a user-defined region. The extent of this sub-domain covers the volume where there would have been teeth. The additional source results in modified Navier-Stokes equations as follows:

$$\frac{\partial(\rho\overrightarrow{v})}{\partial t} + \nabla(\rho\overrightarrow{v}\,\overrightarrow{v}) = -\nabla p + \nabla(\overline{\overline{\tau}}) + \rho g + S_M \tag{4.1}$$

The source term S_M is the momentum source required the reproduce the effect of the teeth. Figure 4.1 illustrates how the sub-domain sits relative to the full tooth geometry. The added momentum is the primary momentum source for the resulting system although the smooth rotating cone surface does provide a source of azimuthal momentum itself.

Removing the detailed tooth geometry makes capturing the exact flow physics under the shroud impossible. However it is possible to calibrate for bulk velocity components and mass flow. These two properties are identified as the most important because a) WPL is a direct function of mass flow [7] and b) the mean speed characterises the mean transport. The momentum source model cannot deliver a value for WPL but in an assessment of IGB performance, the

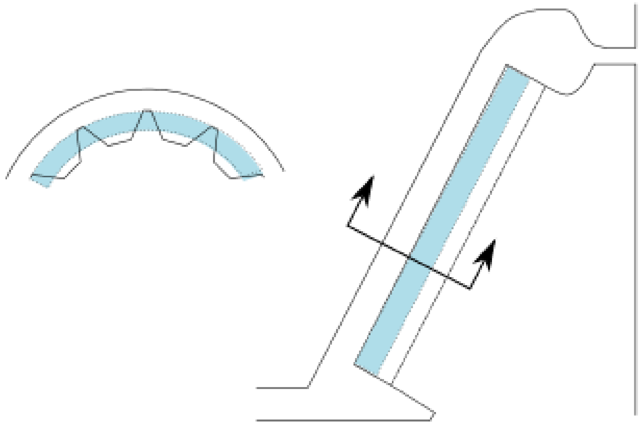

Figure 4.1: The cone and momentum source region superimposed onto the full tooth model. The image shows both the side profile of the tooth domain and a cross-section. The fluid sub region is highlighted in blue. Please refer to Figure 1.2 to see an image of the complex physical gear.

ability to accurately model mass flow is important. The intent behind calibrating velocity components is to obtain representative mean flow characteristics, primarily magnitude, direction and wall shear in single phase. When the momentum source model was under development the intention was to add an oil phase. As will be shown later in this chapter, this now seems unlikely to be feasible or representative.

The momentum source approach requires detailed data to which the momentum sources within the cone representation can be mapped. Webb [31] established the capability of CFD to adequately match experimental data for a shrouded spiral bevel gear with 360° shroud running without a pinion. In the experimental study used for validation the shrouded gear was mounted within a large chamber and run with minimal oil, as close to single phase as possible [7]. The gear-shroud geometry for this current study is slightly different to that modelled previously and extends further so a new detailed-geometry CFD model was required for momentum source calibration.

4.3 Geometry Creation

4.3.1 Full Tooth Model

Using the methodology of Webb [31] a new geometrically representative full tooth domain was created. The gear-shroud geometry was developed using Pro/Engineer Wildfire 4.0 [63]. A schematic view of this model can be seen in Figure 4.2.

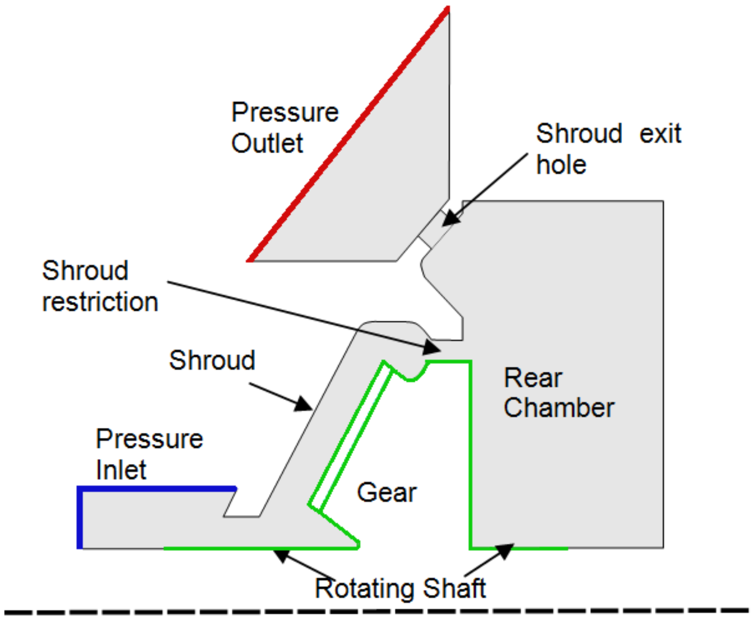

Figure 4.2: Side view of the full tooth model showing all relevant boundary conditions.

The shroud incorporates 23 equally spaced holes through which the air pumped by the gear is ejected. On the test rig oil is also ejected through these holes. The CFD model is an axisymmetric segment of the shroud, including one hole. A 1/23 (15.65°) section of the shroud could not be used as the gear contains 91 teeth and this is not divisible by 23. A section including 4 teeth (15.82°) was modelled and the area of the hole was slightly increased to be representative of the larger domain. This maintained the correct flow area. Webb's model did not extend as far as the shroud exit holes and so he was able to model a single tooth.

Guidance was taken from Webb [31] on a suitable mesh density for rotating gears, with approximately 250,000 cells within each tooth valley.

4.3.2 Momentum Source Model

The geometry of the cone model was constructed with the distance between the slanted cone face and the inside shroud surface set such that the cross sectional area of the gap was the same as in the full tooth model (accounting for the tooth channels). This is an essential step as mass flow rate and gas speeds are targeted variables for calibration. A fluid sub-region (sub-domain) was created starting from the cone surface and rising to the height of the teeth on the original gear. This means the distance between the top of the teeth and the shroud is the same as the distance between the top of the fluid sub region and the shroud. Figure 4.1 shows the cone geometry and the fluid sub region superimposed onto the full tooth model for comparison.

All other geometrical features, including the shroud, are identical to the full tooth model. A 15.82° sector of the cone was used as this is the same size domain as the four teeth modelled in the full tooth model. Figure 4.3 illustrates the momentum source model geometry and boundary conditions. The outlet is just a convenient point to end the computation; physically this is part of the external bounding chamber.

The cone model was meshed using ANSYS ICEM CFD meshing software [64]. The mesh was designed with enough cells within the fluid sub region to ensure suitable velocity resolution. The rest of the domain was meshed around this criterion with additional refinement at the shroud inlet, shroud outlet and shroud restriction. Images of the full mesh are shown in Figure 4.4. The final computational domain contained 187,000 hexahedral cells. Note that the geometrically representative gear tooth model contains around 2 million cells, which is approximately 10 times more than this model. Removing the tooth valleys, where a very dense mesh is required, allows the mesh density to be universally reduced and very large computational savings to be made. For rotating surfaces y^* values were designed to be close to but above 20. On the cone surface 98% of cells are above this value as are 70% across all rotating surfaces and the static shroud.

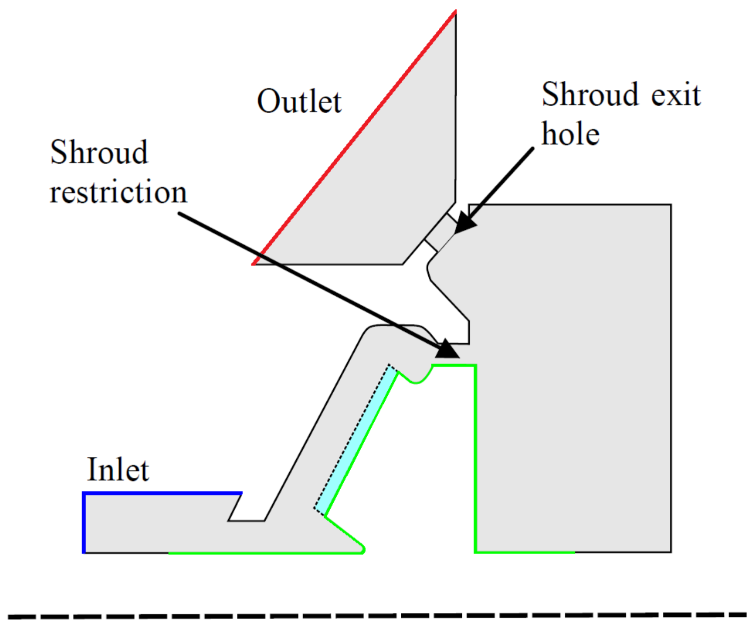

Figure 4.3: Boundary conditions for the cone and momentum source model. Blue lines represent pressure inlets, red lines pressure outlets and green lines rotating walls.

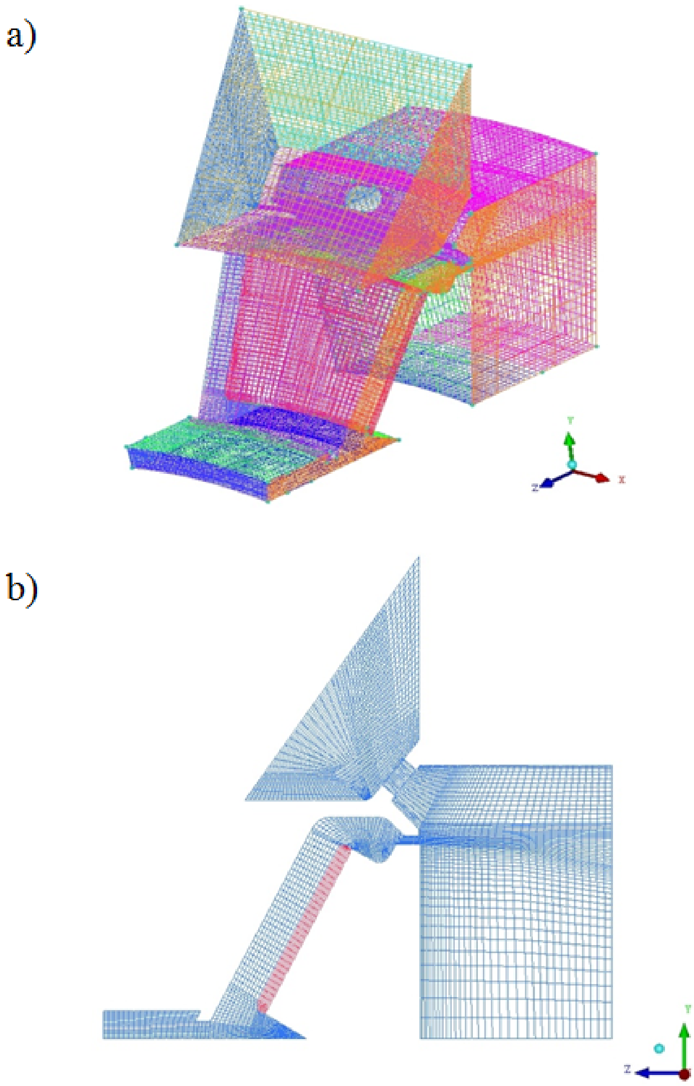

Figure 4.4: Image showing a) the full 15.82° cone model mesh and b) a side view of the fluid sub-region, highlighted in red. Note, the apparent step changes in mesh density shown are due to the difficulties of displaying fine mesh regions in an image and do not exist in the actual model.

4.4 CFD Methodology

This section details the specific CFD methodology for the full tooth and momentum source models. The CFD formulation is as described in Chapter 3 unless otherwise mentioned here.

4.4.1 Full Tooth Model

Steady State Set Up

As previously shown by Rapley [29] and Webb [24], rotating gears display transient behaviour, however it is possible to obtain an initial, approximate solution in steady state that subsequently accelerates convergence of the transient model. The rotation speed for which experimental data is available is 12,266 RPM but both Webb and Rapley found it best to obtain an initial solution at 4,000 RPM and then increase this to 12,266 RPM. Turbulence and energy models are then applied at this maximum rotational speed. The fluid, initially defined as a constant density to ease convergence, is then modelled as an ideal gas allowing for the fact that gear tip Mach number reaches 0.54. Mach number exceeds 0.3 in approximately 25% of the domain and therefore compressibility effects must be taken into account. This ramping up process is typically completed in 6,500 iterations taking approximately 3 hours on 24 Intel Xeon E5472 3.0GHz CPUs.

Temporal Discretisation

Having obtained an initial solution the simulation was than calculated transiently. Second order discretisation was used where possible during this work. Transient parameters set are a time step size of $5.37 \times 10^{-6} s$ (equivalent to a CFL number of 1.99) for 910 time steps. This simulates one complete rotation of the gear at 12,266 RPM. Each time step is limited to a maximum of 50 inner iterations though typically each time step converges within 25 iterations.

Turbulence Model and Wall Functions

The k-ϵ RNG turbulence model was utilised for this model for reasons discussed fully in Chapter 3. The computational mesh was created based on Webb's guidelines [24] and 80% of cell y^* values are within the 20-80 range. As such standard wall functions have been employed. Regions of low y^*, in the range 10-15, exist in some locations on the inlet bottom wall and on the back wall of the outer chamber section, however Webb was able to obtain results which matched well with experimental results [31] with the same mesh density. As a result it was not found necessary to refine the mesh at these locations which would have resulted in an additional computational expense.

Boundary Conditions

The inlet and outlet of the domain are defined as a pressure inlet and outlet respectively, both set at atmospheric pressure (0 Pa gauge pressure). Supporting work, presented in Appendix A, has shown that there is a negligible pressure difference between the inlet and outlet of the shroud in the outer chamber which justifies this boundary condition. An engine representative inlet swirl number of 0.89 was used, the value of which was also determined by supporting work presented in Appendix A (also refer to Chapter 5 for more information on the swirl numbers used in this thesis). A rotational speed of 12,266 RPM is set for each moving wall. Rotating periodic boundaries were used for the sides of the model. Figure 4.2 depicts these boundary conditions.

Rotating Reference Frame

A rotating reference frame as described in Section 3.4.1 was employed for the full tooth model owing to its repeating (but not axisymmetric) geometry. This was applied to all regions upstream of the shroud hole. It is not appropriate to model the shroud hole with a rotating reference frame as it is not a continuous feature and as such is was defined as a separate fluid domain with a stationary frame of reference. The interface between the stationary and rotating reference frames is at the shroud outlet. This multiple reference frame formulation assumes the flow is steady but can give a good approximation for time averaged unsteady flow. As only time averaged data was used in this work, the multiple reference frame model is preferable to a computationally more intensive unsteady sliding plane formulation.

Convergence

General residuals for the whole domain are recorded, continuity converging to an order of magnitude of 10^{-4}, energy to 10^{-6} and all velocities and turbulence criteria to 10^{-5} typically within 25 inner iterations.

The non-dimensional torque coefficient C_m was also monitored on all surfaces. Convergence was determined by comparing C_m histories per revolution, and over several revolutions, and considered converged when successive revolutions yielded values within 3% of each other. This was typically achieved within 5 revolutions for all full tooth simulations. A plot of gear moment against flow time is shown in Figure 4.5 for the 10th gear revolution. Individual revolutions take approximately 16 hours to complete on 24 Intel Xeon E5472 3.0GHz CPUs.

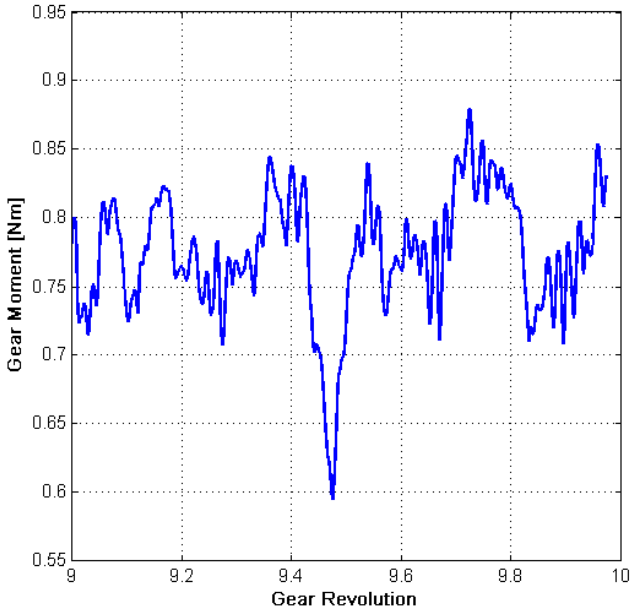

Figure 4.5: Graph showing the convergence of gear moment against flow time for the 10th gear revolution of the full tooth model.

4.4.2 Momentum Source Model

Turbulence Model

The k-ϵ RNG turbulence model, as developed by Yakhot et al [47], was selected for the momentum source model. Rapley [39] has shown it appropriate for modelling rotating cone cases. Re_{rot} for the current work is above 10^6, which is in the fully turbulent region. Though the current work (cone and momentum source) is significantly different from the cone work carried out by Rapley, the k-ϵ RNG model will be used in a first case as Rapley has shown it to accurately model the flow for this Re range. Since the flow is well out of the transitional region RANS modelling is appropriate.

Wall Functions

85% of y^* values for the momentum source model were within the range 20-50 and so standard wall functions were appropriate.

Boundary Conditions

Boundary conditions for the momentum source model are as follows. The inlet and outlet of the domain are defined as a pressure inlet and outlet respectively, both set at atmospheric pressure (0 Pa gauge pressure). An engine representative inlet swirl number of 0.89 was used (please refer to Chapter 5 for more information of the swirl numbers used in this thesis). A rotational speed of 12,266 RPM is set for each moving wall. Rotating periodic boundaries were used for the sides of the model. Figure 4.3 depicts these boundary conditions.

Reference Frame

The momentum source model was entirely calculated with a stationary reference frame.

Fluid Sub-model Source Terms

In the momentum source model the fluid sub-region was assigned source terms of constant value in the axial, radial and azimuthal directions. Initial values for these source terms were calculated by finding the difference in mass flow, $\Delta \dot{m}$, between the FTM and a cone model without any additional momentum sources (the CM model). The force required to accelerate the mass of air in a control volume to make up for this mass flow deficit was determined and applied to the model. These source terms were then refined across a series of models.

Temporal Discretisation

Having removed the tooth geometry from the momentum source model, the case is comparable to the cone models investigated by Rapley [29] and discussed in Chapter 2. Rapley found that unsteady fluctuations were evident in his cone model and recommended future cases be modelled transiently. However, with the addition of momentum sources it may be possible to run the source model in steady state if they act as a stabilising force and suppress the cones transient behaviour. The benefit of this would be a large saving in computational expense.

The momentum source model was first run in steady state and mass flow rates were monitored at the inlet and outlet. Mass flow rate data for both these boundaries is shown in Figure 4.6 for 10,000 iterations.

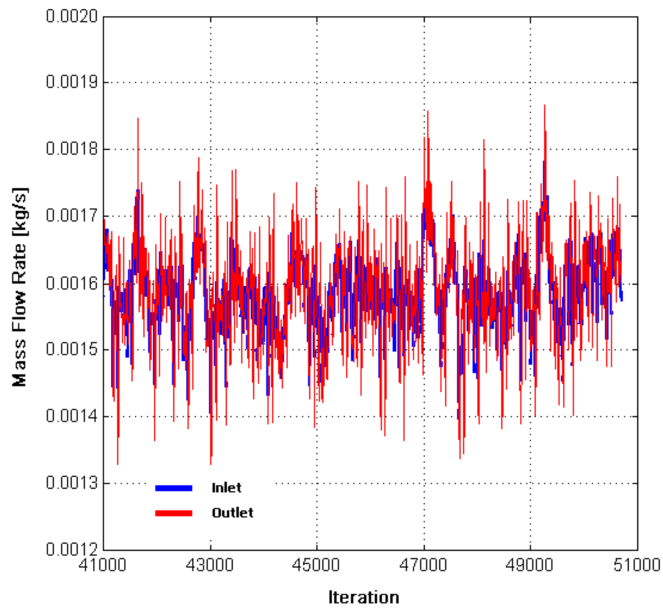

Figure 4.6: Mass flow rate data for the inlet and outlet of the momentum source model taken over 10,000 steady state iterations for model SM3 (please refer to Table 4.1).

As can be see from the graph, mass flow rate is unable to converge to a steady value. Although averaged over 10,000 iterations a mean value of 0.00158 kg/s can be determined, at individual time steps this may vary by +/- 13%. From this it can be concluded that unsteady behaviour is not entirely suppressed and calculating the model transiently may be more appropriate.

Based on this conclusion, a transient model was then run again monitoring the mass flow rates at the inlet and outlet of the model. Transient parameters set are a time step size of $2.15 \times 10^{-5}s$ (equivalent to a CFL number of 1.79) for 228 time steps. This simulates one complete rotation of the gear at 12,266 RPM. Mass flow rate data is displayed in Figure 4.7 for 17 gear rotations.

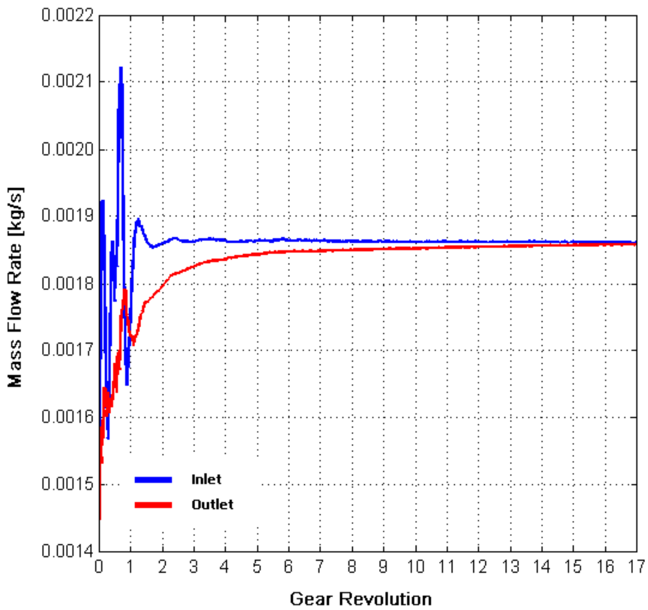

Figure 4.7: Mass flow rate data for the inlet and outlet of the momentum source model taken over 17 transient gear rotations for model SM3 (please refer to Table 4.1).

Figure 4.7 shows a clear convergence of both inlet and outlet mass flow rates to a value of 0.00186 kg/s after approximately 12 gear rotations. This convergence confirms that an unsteady formulation is required.

A transient calculation results in a longer computational time, approximately 12 hours in comparison to 2 hours steady state. This is still significantly less expensive than an equivalent tooth model, which takes approximately one week to run, due to a coarser mesh and a correspondingly larger time step. As a result all momentum source models simulated in this thesis have been run transiently.

Convergence

The same convergence criteria as the full tooth model were applied to the momentum source model.

The simulation then continues to run until C_m values for the rotating surfaces reached a steady value. This was typically achieved within 2,000 additional iterations. Total run time for the single phase momentum source model is approximately 3 hours on a 4 core Intel(R) Core(TM)2 2.66GHz CPU.

4.5 Momentum Source Model CFD Analysis

4.5.1 Data Analysis

In order to calibrate the momentum source model, velocity profiles from the geometrically representative and momentum source models are compared. However, this presents some challenges as the distance between shroud and tooth tip/valley is different to the distance between shroud and cone surface.

To account for this, a cross section of velocity data has been averaged across several radial line profiles to produce a single synthetic velocity profile for each model. This process is illustrated in Figure 4.8. Figure 4.8a shows the geometrically representative geometry with radial lines at tooth tip and tooth valley. The radial distance was non-dimensionalised to span from 0 to 1 and data averaged over all the profiles. In order to directly compare transient full tooth data to the steady state source term model, data was time averaged over 5 fully converged revolutions. Convergence was defined as existing when C_m values for successive revolutions were within 5% and 5 revolutions were then taken from this point.

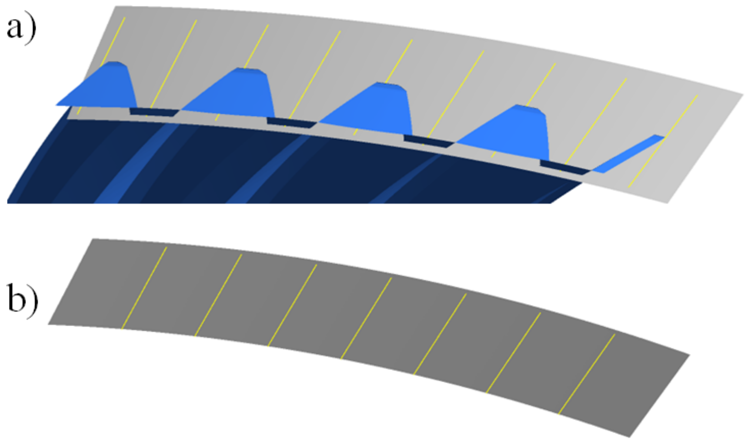

Figure 4.8: Cross-sections of a) full tooth model and b) momentum source model. The yellow lines represent the profile lines that were averaged to produce a velocity profile for each model.

4.5.2 Single Phase Results

As a baseline case the cone model was run with no additional source terms. Determining the difference in momentum between the full tooth model and such a cone model at selected points along the gear face allowed a first estimate of the momentum source terms to be made. These terms were then calibrated so as to match the velocity profiles at 8 regions in the domain, defined in Figure 4.9. There was a particular focus on calibration at the inlet (1), shroud restriction (7) and shroud outlet (8) regions, as the inlet and outlet are key from a pump model standpoint.

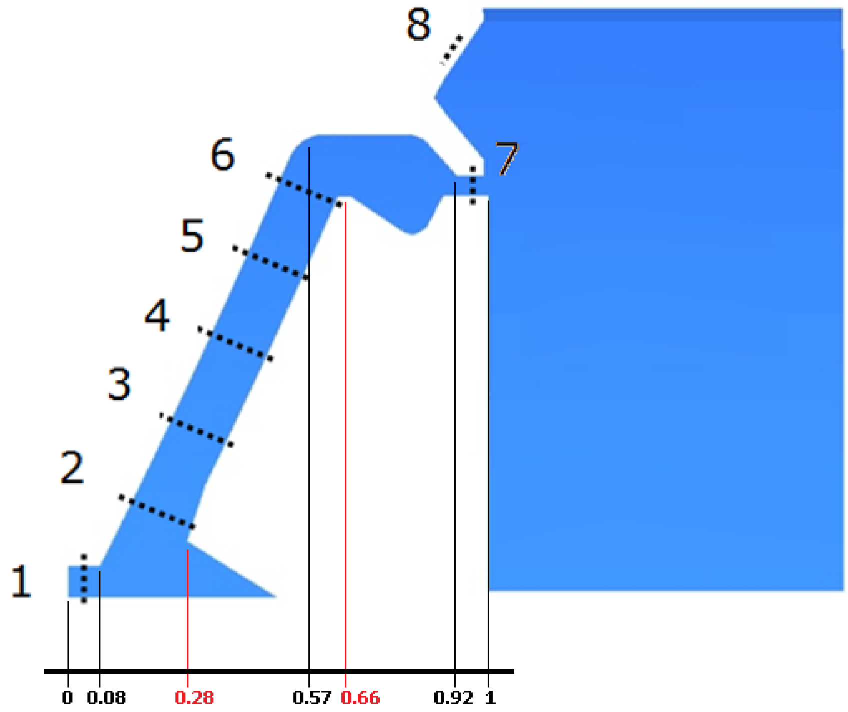

Figure 4.9: Side view of momentum source model domain showing points of data comparison through the tooth region and at the shroud restriction. The non-dimensional position of key geometry features on the shroud are also displayed at the bottom of the image.

Three source term models are compared in this section, designated SM1-SM3. Spiral bevel gears (Figure 1.2) have highly three dimensional geometry and source terms in three dimensions are therefore required to correctly define the flow field. Each source term model has the same term in the azimuthal direction but different terms in the axial and radial directions, which quantifies the amount of pumping the teeth would have on the fluid. This axial term increases from SM1 to SM3 and these terms are given in Table 4.1 for each model. The full non-dimensionalised velocity and mass flow data at positions 1, 7 and 8 are reported in Tables 4.2-4.4 for the full tooth model (FTM), cone model without momentum sources (CM) and three source term variants (SM1-SM3). The velocity parallel to the gear topland has been termed the toothwise velocity and the jet velocity is the velocity perpendicular to the shroud outlet hole.

Table 4.1: Table detailing the momentum source terms applied in the cylindrical coordinate system for the momentum source models analysed in this thesis.

Model	**Axial Source Term [Nm^{-3}]**	**Radial Source Term [Nm^{-3}]**	**Azimuthal Source Term [Nm^{-3}]**
CM	0	0	0
SM1	125,000	100,000	126,000
SM2	150,000	100,000	126,000
SM3	175,000	200,000	126,000

Velocities have been non-dimensionalised with the following equation

$$u_{nd} = \frac{u}{r_{local}\omega} \tag{4.2}$$

where u_{nd} is non-dimensionalised velocity, u is velocity, r_{local} is the local outer diameter of the gear and ω is the gear rotational speed (rad/s). The radial position has been non-dimensionalised between 0 and 1 such that the gear surface is 0 and the shroud surface is 1.

Table 4.2: Non-dimensional velocity and mass flow data at the inlet of the cone model. The case without momentum source (CM) and three momentum source models (SM1-3) are compared to the full tooth model (FTM). The percentage difference of each model from the FTM is given in brackets next to the corresponding value in the table.

Model	Non-dimensional Axial Velocity		Non-dimensional Azimuthal Velocity		Mass Flow Rate [kg/s]	
FTM	0.13	-	0.16	-	0.00160	-
CM	0.04	(-73.4%)	0.32	(104.5%)	0.00040	(-75.1%)
SM1	0.14	(3.0%)	0.20	(29.8%)	0.00156	(-2.8%)
SM2	0.15	(10.5%)	0.20	(28.5%)	0.00166	(4.0%)
SM3	0.16	(23.8%)	0.20	(28.1%)	0.00186	(16.5%)

Table 4.3: Non-dimensional velocity and mass flow data at the shroud restriction of the cone model. The case without momentum source (CM) and three momentum source models (SM1-3) are compared to the full tooth model (FTM). The percentage difference of each model from the FTM is given in brackets next to the corresponding value in the table.

Model	Non-dimensional Axial Velocity		Non-dimensional Azimuthal Velocity		Mass Flow Rate [kg/s]	
FTM	0.15	-	0.71	-	0.00160	-
CM	0.04	(-73.3%)	0.48	(-32.3%)	0.00040	(-75.0%)
SM1	0.15	(-4.4%)	0.65	(-7.4%)	0.00156	(-2.8%)
SM2	0.16	(1.5%)	0.70	(-0.8%)	0.00166	(3.8%)
SM3	0.17	(13.1%)	0.71	(1.0%)	0.00186	(16.3%)

Table 4.4: Non-dimensional velocity and mass flow data at the shroud outlet of the cone model. The case without momentum source (CM) and three momentum source models (SM1-3) are compared to the full tooth model (FTM). The percentage difference of each model from the FTM is given in brackets next to the corresponding value in the table.

Model	**Non-dimensional Jet Velocity**		**Non-dimensional Azimuthal Velocity**		**Mass Flow Rate [kg/s]**	
FTM	0.17	-	0.21	-	0.00160	-
CM	0.05	(-71.6%)	0.08	(-61.5%)	0.00041	(-74.1%)
SM1	0.16	(-3.6%)	0.20	(-3.0%)	0.00155	(-3.0%)
SM2	0.17	(2.5%)	0.21	(3.4%)	0.00166	(3.9%)
SM3	0.19	(16.0%)	0.23	(13.8%)	0.00186	(16.0%)

Figure 4.10 shows a comparison of axial and azimuthal velocity components at the shroud restriction for these same models. Similarly Figure 4.11 reports the velocity components at the shroud outlet.

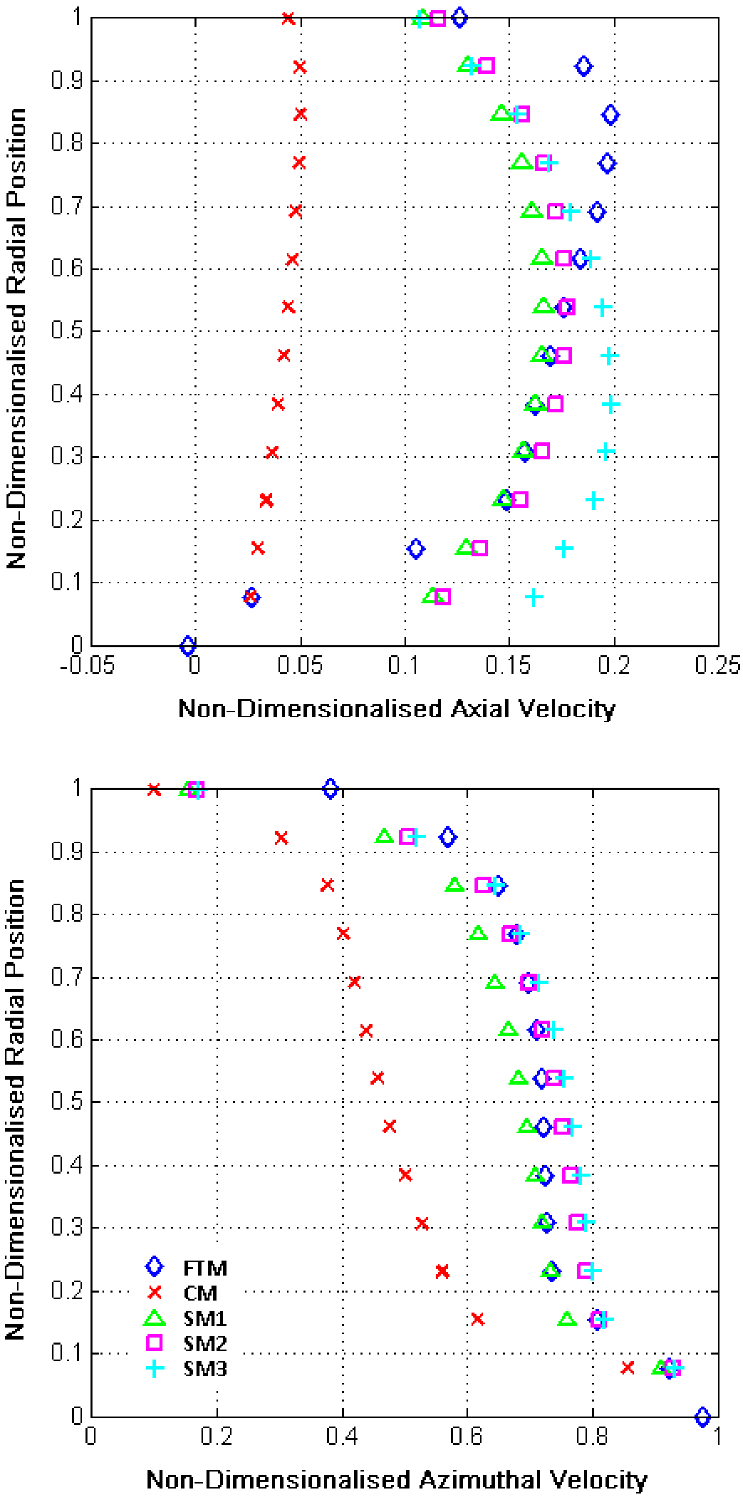

Figure 4.10: Axial and azimuthal velocity components at the shroud restriction for the full tooth model (FTM), the cone model without momentum sources (CM), and 3 source models variants (SM1-3).

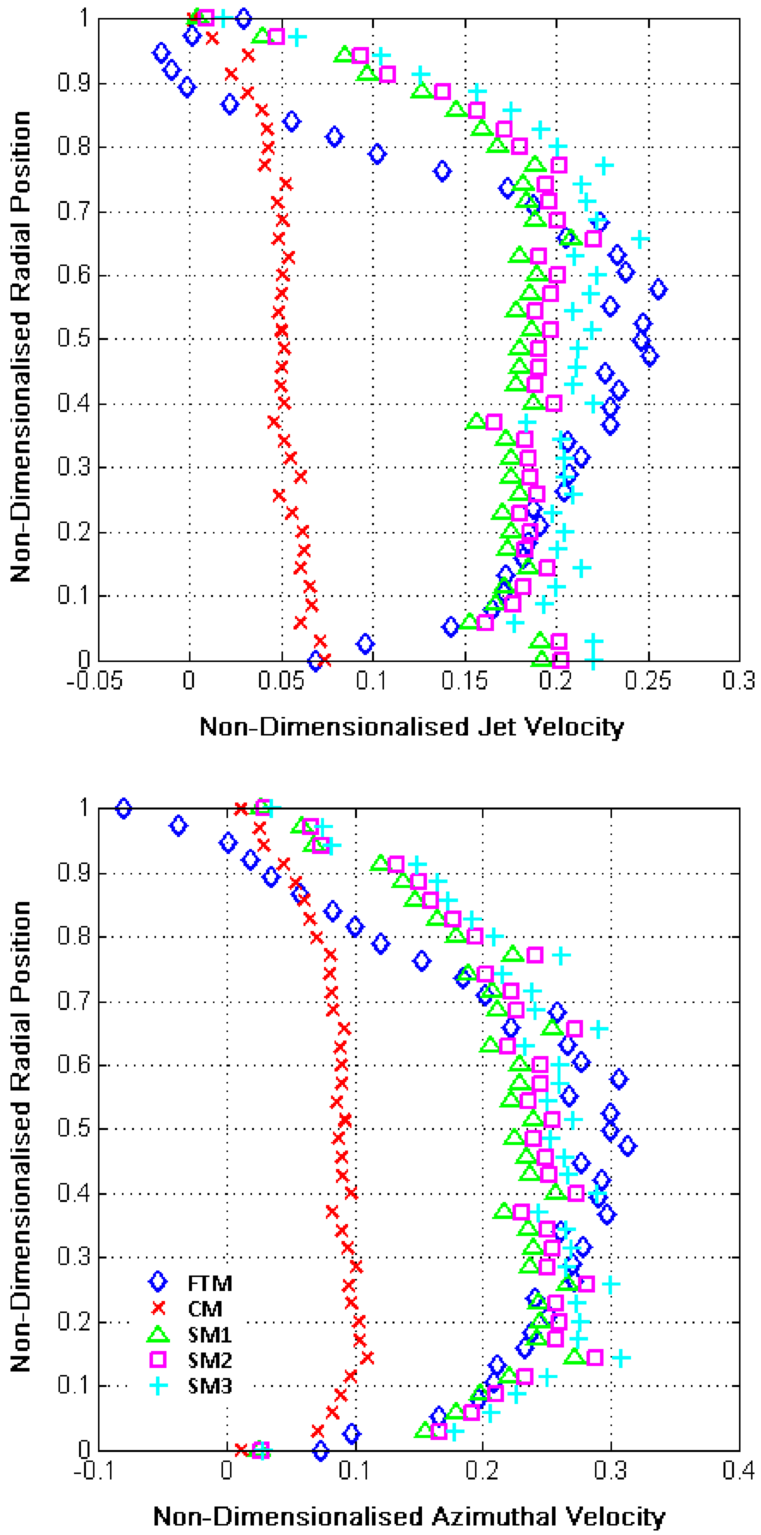

Figure 4.11: Jet and azimuthal velocity components at the shroud outlet for the full tooth model (FTM), the cone model without momentum sources (CM), and three source term models (SM1-3).

These results highlight the expected difficulty in capturing the full flow physics at the various locations using a single momentum source. For example model SM1 displays the best results at shroud inlet and is within 2.8% of the full tooth model mass flow rate at outlet. The next closest model is SM2 (highlighted in green in Tables 4.2-4.4) which is within 4%.

However, model SM1 is not the best when comparing restriction and outlet positions. In these regions SM2 provides the closest match to axial and azimuthal velocity components within 2.5% and 3.4% respectively. Mass flow is also consistently strong at these positions within 3.9%. SM1 in comparison is a poorer match for velocity components, within 4.4% for axial velocity and 7.4% for azimuthal velocity.

Taking the main aim of the momentum source model as to reproduce the pumping effects the shrouded gear exerts on the fluid in the IGB chamber system, as opposed to replicating the detailed flow structure under the shroud, then SM2 is the best model. SM2 provides a good balance between accurate mass flow rates and accurate velocity components and so was selected as the base for the next stage of calculations (in which oil transport will be computed).

Nevertheless, Table 4.2 shows a significantly large difference in azimuthal velocity at the inlet between the full tooth model and all the tested momentum source models. However, as will be described in Chapter 5, the magnitude of the inlet swirl velocity has no significant impact on the swirl at the shroud outlet. Therefore the mass flow rate at this point is a better indicator and it is found to be within 4% of the FTM value. Getting the mass flow through the model correct is essential for a pump model and to characterise WPL. At the outlet the velocities are well predicted; therefore both flows in the main chamber and overall through the whole system should also be well predicted.

As an additional point of interest, the azimuthal velocity at the inlet for the CM model is much larger (approximately 100% larger) than the other models with the additional source terms. Though this appears counter-intuitive, it is because the other models have an increased through flow which pulls fluid with a lower azimuthal velocity into this region. As a result the average azimuthal velocity at the inlet is lower for models with increased through flow.

4.5.3 Single Phase Simple Chamber Model

From the initial cone model with defined inlet and outlet boundary conditions, the next step was to create a closed system with the gear representation inside a bearing chamber. A bearing chamber was created with the same geometry as one tested experimentally by Johnson [23]. An image of the domain can be seen in Figure 4.12.

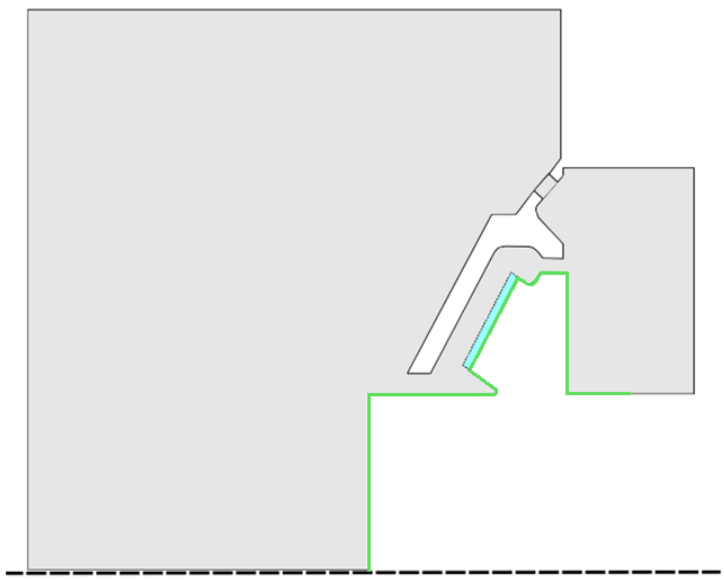

Figure 4.12: Boundary conditions for cone model with outer chamber. The green lines represent moving walls and black lines are stationary walls. The gear carrier detail is not shown in this figure and forms no part of the CFD model.

The same CFD methodology as described previously for the momentum source model was applied here. Over 80% of wall y^* values are within the 20-50 range and so a standard wall function approach has been applied. The regions of low y^* occur in the main chamber and away from the key regions of interest.

The velocity profiles at the shroud outlet are shown in Figure 4.13 for the full tooth model (FTM), momentum source model SM2 and full chamber model FCM. Velocity and mass flow data are recorded in Table 4.5.

At all locations the chamber model compares well to the initial cone model. It is within 7% for each velocity component. Mass flow rates are within 5%.

Table 4.5: Velocity and mass flow data at the shroud outlet for the calibrated source model (SM2), and a calibrated source model with an outer chamber (FCM). Data is given in relation to the full tooth model (FTM). The percentage difference of each model from the FTM is given in brackets next to the corresponding value in the table.

Model	Non-dimensional Jet Velocity		Non-dimensional Azimuthal Velocity		Mass Flow Rate [kg/s]	
FTM	0.17	-	0.21	-	0.00160	-
SM2	0.17	(2.5%)	0.21	(3.4%)	0.00166	(3.9%)
FCM	0.18	(5.9%)	0.22	(7.2%)	0.00168	(5.0%)

These results show that using a momentum source model developed in isolation as part of a chamber model is feasible. Consistent bulk flow rates and velocities are displayed. At the inlet and outlet the mass flow rates are within 5% of the full tooth model values. This is a positive step towards a full IGB model and the eventual addition of more complex components to the system.

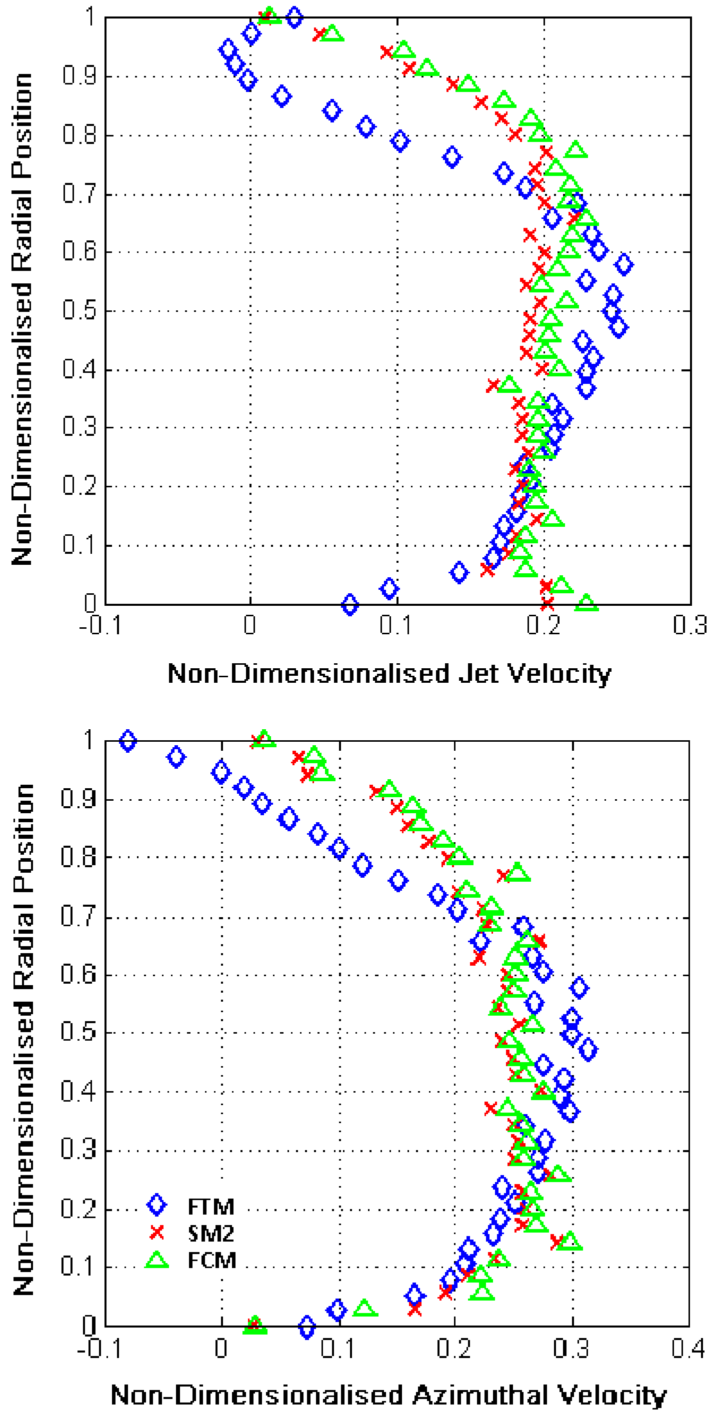

Figure 4.13: Jet and azimuthal velocities at the shroud outlet for the full tooth model (FTM), calibrated source model (SM2), and calibrated source model with an outer chamber (FCM).

4.5.4 Two Phase Full Tooth Model Results

Droplet Release at Shroud Inlet

Experimental work by Johnson et al [2] has shown that a suspended mist of oil is formed in the outer chamber when gears rotate at high speeds. The change in pressure seen across the gear draws in air flow from the outer chamber through the domain and therefore oil is also ingested by the gear.

This process has been simulated by releasing oil droplets at the entrance of the shroud and monitoring the droplet impact sites. At the time this work was undertaken there was no experimental data giving droplet size distribution for the UTC gear windage test rig. Data from Karlsruhe Institute of Technology (for example [61]) suggests that the majority of droplets within an aeroengine bearing chamber will be in the range 1 to 100 microns in diameter. Webb chose values for his Rosin-Rammler distribution of mean diameter 10 microns and spread factor 3.5 giving 20 diameters in 1-100 microns range and the same parameters have been used here. Recent work by Simmons et al [54] have shown that only droplets with a diameter of less than 10 microns are likely to be ingested by the gear. This suggests the range used in this work is slightly too high but that the mean diameter is correct.

Figure 4.14 shows the position of the droplet injection surface. Droplets are injected with a zero initial speed and pick up momentum from the continuous phase.

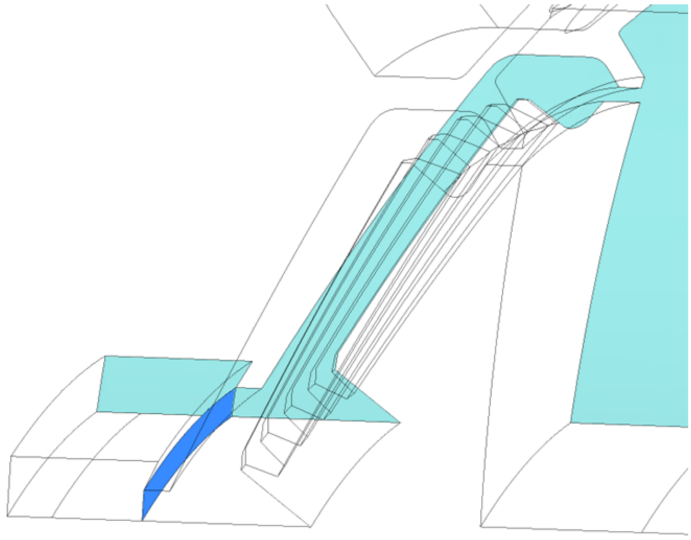

Figure 4.14: Boundary conditions for the full tooth model. Inlet droplet injection surface is highlighted in dark blue.

An oil mass flow rate of 0.25 l/min was used, representing one of the test conditions on the rig. This was adjusted to 0.011 l/min for the 4-tooth sector. Droplets were injected at the beginning of the simulation and monitored for one complete rotation of the gear. This reduces the number of droplets FLUENT needs to track at any one time, improving the speed of the simulation.

When droplets impact on walls within the simulation they can either be removed from the simulation (escape condition) or they can be rebounded back (either with the same energy as prior to impact or with reduced energy, this is the reflect condition). Unless otherwise stated the shroud surface was always set as an escape condition. Droplet impact locations were computed and compared for escape and reflect conditions. In this study, for the reflect condition normal and tangential coefficients of restitution were left at the default value of 1.0 so that a particle retains all of its normal and tangential momentum after the rebound.

Figure 4.15 is a histogram comparing the impact locations of droplets on the shroud for the case where there is an escape condition on all surfaces and for a case where a reflect condition is applied on the rotating surfaces. With the escape condition applied to the gear surfaces droplets are unphysically removed from the calculation. In reality, all droplets that impact the gear surfaces would ultimately be shed back into the flow.

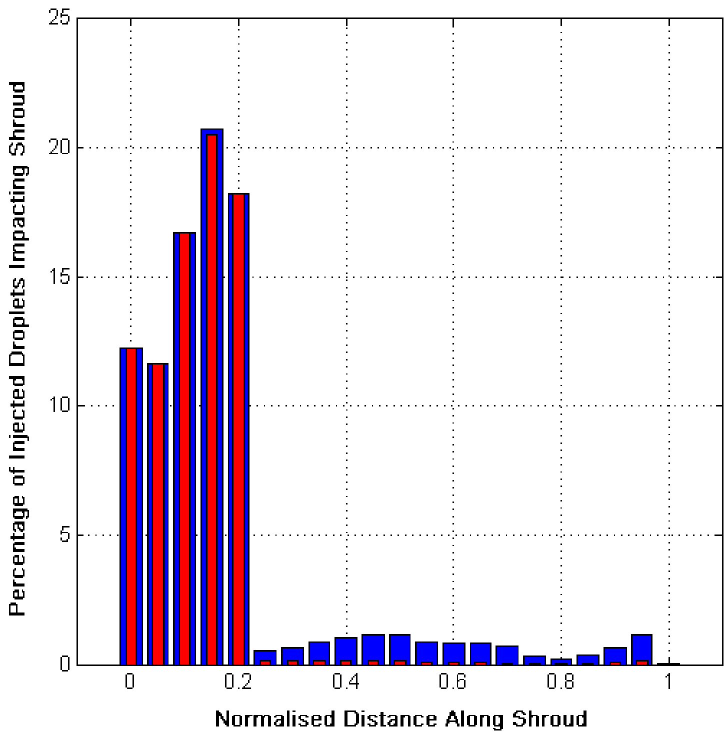

Figure 4.15: Percentage of droplets released into the domain that impact the shroud for geometrically representative model with escape boundary conditions (Red) and with reflect boundary conditions (blue). The impact position along the shroud is non-dimensionalised between 0 and 1. Refer to Figure 4.9 for non-dimensionalised shroud positions.

The reflect condition displays 12% more impacts at higher shroud locations as these droplets are no longer being removed from the domain as soon as they impact the gear. This is significant enough to justify the additional computational expense in future models in order to achieve more realistic droplet behaviour.

Regardless of the impact condition applied, Figure 4.15 shows clearly there is a very high number of impacts at the shroud inlet (around 80%). This suggests that most of the oil entering the gear-shroud domain through the inlet will initially form a film on the shroud towards the inner diameter. It may ultimately form so thick a film that droplets can strip from it and be re-ingested into the flow, further simulation would be required to establish this. However, this behaviour is not inconsistent with what has been observed on the test rig. Analysis of the CFD data shows that only around 6% of the droplets injected at the shroud inlet are ejected at the back of the shroud in the present configuration.

Droplet Release at Into-Mesh Location

The second source of oil under the shroud is the into-mesh jet that lubricates and cools the crown-pinion mesh point. Under normal operation the into-mesh jet is considered a key contributor to oil found under the shroud. With the 4-tooth, axisymmetric model it is not possible to truly simulate an into-mesh jet as it exists at only one angular location within the geometry. Work by Johnson et al [2] showed that the bulk of the into-mesh jet oil is ejected straight onto the shroud once it has passed through the mesh point. However, some of the oil is carried around by the gear and this is simulated in the CFD study by releasing droplets from one gear tooth flank on the trailing edge as illustrated in Figure 4.16. A reflect condition is applied on the gear surfaces to prevent oil shed from the injection point being immediately removed from the calculation when it impacts the opposite tooth flank on the leading edge.

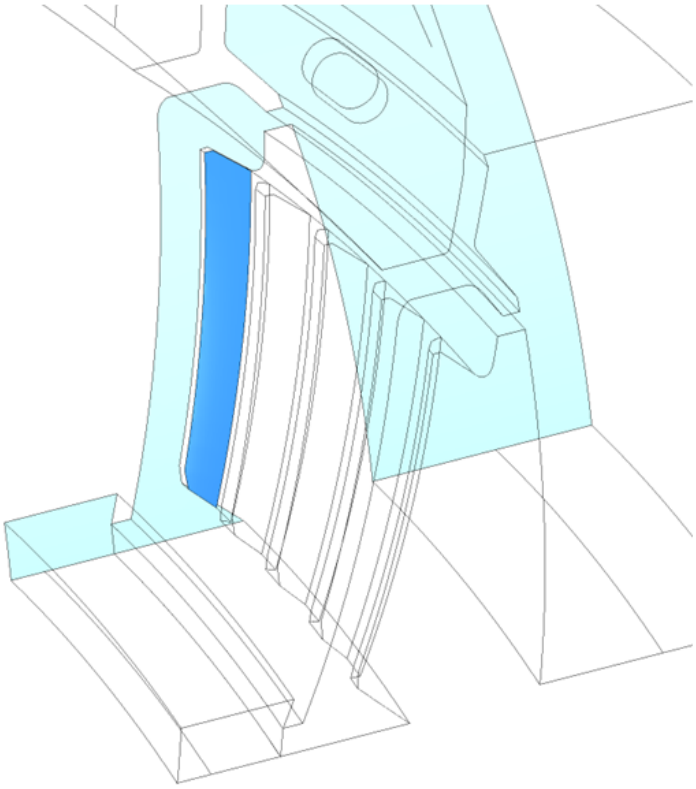

Figure 4.16: Boundary conditions for the full tooth model. Into-mesh droplet injection surface is highlighted in dark blue.

Droplet sizes were consistent with those described in Section 4.5.4 and a representative mass flow rate of 1 l/min, again adjusted to 0.044 l/min for the 4-tooth segment, was taken for the into-mesh jet. Droplets were released at the beginning of the simulation and tracked for one complete revolution of the gear. Droplets were injected with a zero initial velocity and picked up by the continuous fluid phase.

Shroud impacts were monitored and are reported in Figure 4.17. The histogram shows a very different impact distribution compared to droplets released at shroud inlet. There is a far more even distribution of impacts along the shroud with a fairly high number impacting towards the top of the shroud as it changes direction (the so-called gutter region). Compared to droplets ingested at the inlet (where few make it past the inlet section) the droplets from the into-mesh jet comprise the majority of those which collect on the shroud and those which are worked by the rotating gear.

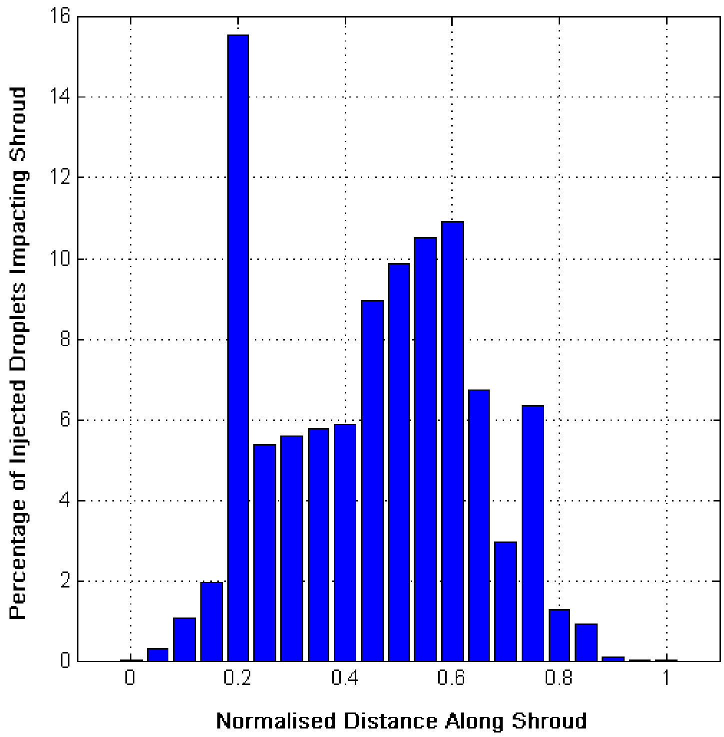

Figure 4.17: Percentage of droplets released into the domain from the into-mesh location that impact the shroud for the full tooth model. The impact position along the shroud is non-dimensionalised between 0 and 1. Refer to Figure 4.9 for non-dimensionalised shroud positions.

Data analysis shows that around 86% of injected droplets impact upon the shroud. The high number of impacts suggest that a film will form on the shroud being thickest in the gutter region where the largest number of impacts occurs. Interestingly, none of the oil droplets introduced from this location are ejected into the back chamber. However, this is misleading because only one revolution has been computed. Oil cannot build up indefinitely on the shroud surfaces and eventually a thick film will form such that oil will be re-injected by the rotating flow ultimately exiting to the rear cavity. A film model is required to see how this oil would behave and preliminary work in this area is presented in the next section.

Addition of Shroud Film Model

A similar case to the into-mesh model was run with a film model applied to the shroud. To account for the droplet behaviour within the tooth valleys a film model would also ideally be placed on the leading gear valley wall. This would represent the collection and stripping of particles at the gear leading edge, likely to be picked up by the fluid or flung onto the shroud. However, in FLUENT it is not currently possible to apply a film model to a rotating wall.

In order to avoid this issue, particles were injected at the gear topland instead of the gear side wall. This represents the oil injected at the into-mesh stripping from the gear edge. Figure 4.18 shows the droplet injection location for this model.

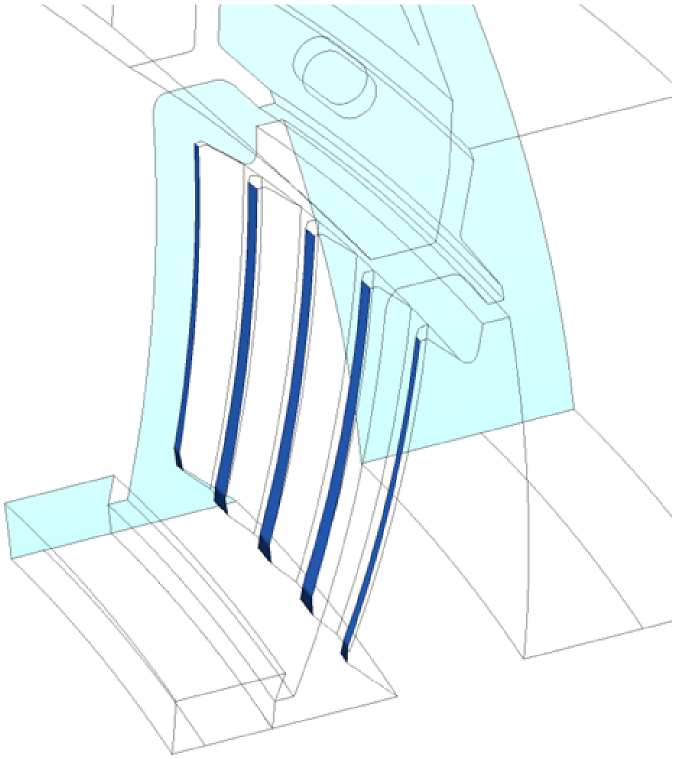

Figure 4.18: Boundary conditions for the full tooth model. The injection surface (gear topland) is highlighted in dark blue.

A flow rate of 1 l/min was used as a representative into-mesh flow rate. This flow rate was maintained for the entire duration of the simulation to investigate oil build up on the shroud and the growth of the film in this location. Due to the resulting very large number of particle tracks, the simulation was only run for 1/10th of a revolution. This was sufficient to show suitable film growth.

For this case the droplet size was set as a uniform 60μm which is within the range of droplets shed from a rotating disk as suggested by Glahn et al [62]. The reason for using a single droplet diameter is that FLUENT only has to track one packet of droplets per cell (as opposed to the Rosin-Rammler distribution where multiple packets are needed) and thus the simulation runs more quickly. The size of shed droplets are determined by gear diameter, flowrate and shaft speed so though there would be some variation droplet sizes are likely fairly uniform.

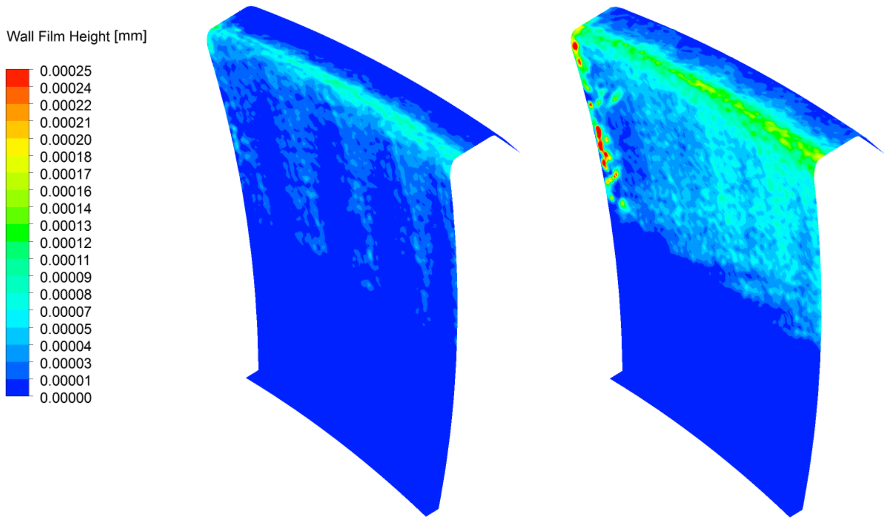

Figure 4.19: Film thicknesses for the oil impacting on the underside of the shroud. The left image shows film thickness at about 1/20th of a revolution and the right image shows film thickness at about 1/10th gear revolution.

Figure 4.19 shows contours of film thickness after approximately 1/20th and 1/10th of a revolution. The plots show clearly that droplets are impacting and forming a film in the upper part of the shroud, consistent with the data obtained without the film model where impact locations alone were considered. The film is thickest in the gutter region where after 1/10th of a revolution the film thickness is around 0.15 microns (which is still very thin). The two plots show clearly that the film is still building up and in addition the film moves both inward down the shroud and also outward towards the back chamber.

Figure 4.20 shows a snapshot of droplet locations after 1/10th of a gear revolution. The droplets are coloured by residence time as indicated by the key on the left of the figure.

Droplets from the gear topland (representing injection from the into-mesh jet) are dispersed both into the back chamber of the model and also to the shroud inlet. It is important to note that the majority of particles which are ejected into the back chamber have been stripped from the shroud at its edge where the shroud restriction opens out into the back chamber. A significant number of droplets are retained under the shroud as part of the film or are recirculated. It is extremely interesting to note that even with the strong flow through the shroud some of the oil droplets travel against the flow.

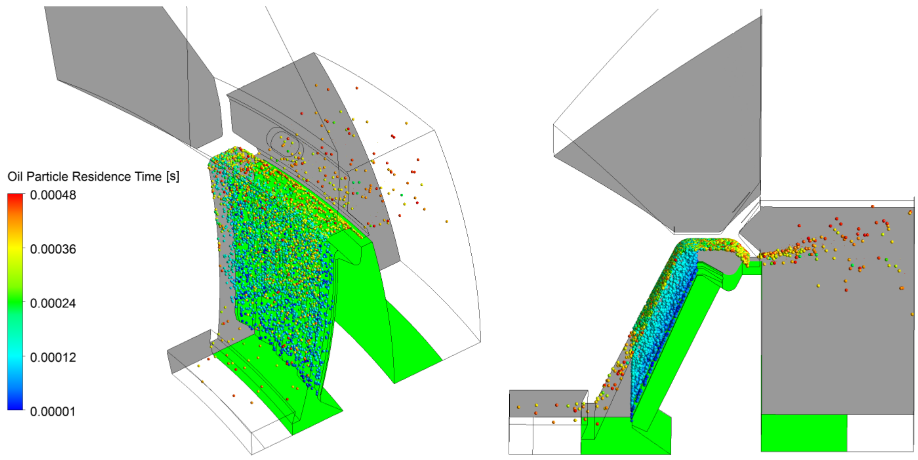

Figure 4.20: An isometric and a side view of the computational domain displaying droplet locations at $4.8 \times 10^{-4} s$ (approximately 1/10th gear revolution). Droplets are coloured by residence time. The side of the chamber is coloured in grey and the rotating surfaces in green for clarity.

4.5.5 Two Phase Momentum Source Model Results

In order to establish the capability of the momentum source model to simulate two phase flows, comparison data is required showing droplet size, landing sites and behaviour under the shroud. At present only CFD data from the representative geometry case is available for comparison.

Droplet release locations for the momentum source cases were chosen to be as similar as possible to those for the representative geometry. Figure 4.21 shows the injection locations for both the shroud inlet and into-mesh droplet release locations. Injection conditions for each case are the same as the corresponding representative geometry cases described previously. Initial droplet velocity was again set to zero.

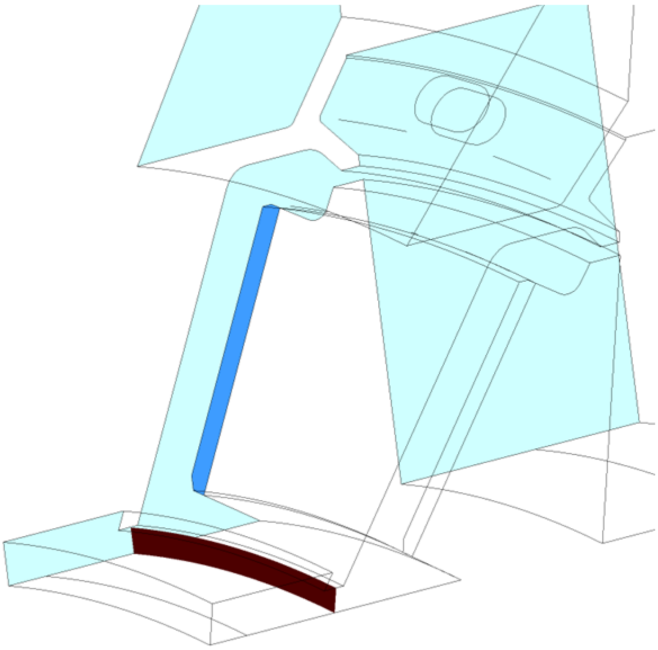

Figure 4.21: Boundary conditions for the momentum source model. Into-mesh droplet injection surface is highlighted in blue and shroud inlet injection surface is highlighted in brown.

Droplet Release at Shroud Inlet

Figure 4.22 shows a comparison between shroud impact histograms for both the momentum source and representative geometry models with droplets injected at the shroud inlet.

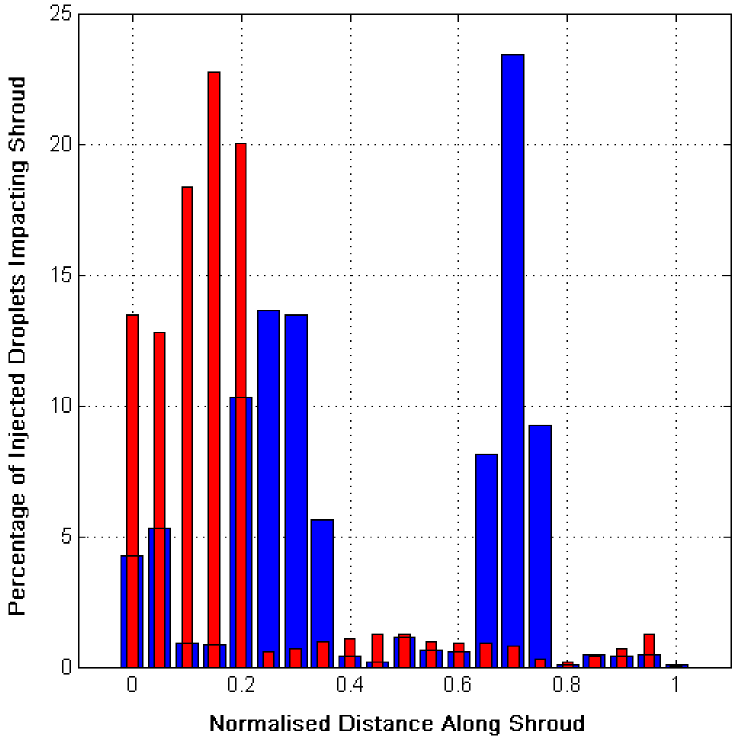

Figure 4.22: Histograms comparing percentage of injected droplets that impact the shroud for the momentum source model (blue) and representative geometry model (red). Droplets are injected at the shroud inlet and impact locations on the shroud are non-dimensionalised between 0 and 1. Refer to Figure 4.9 for non-dimensionalised shroud positions.

For the momentum source model two major impact locations at the inlet and gutter of the shroud are clearly visible. In contrast the representative geometry model has a significant impact location at the shroud inlet but then remaining droplet impacts are spread equally across the remaining shroud length. This is because in the momentum source model the droplets are free to travel with the continuous phase through the domain until they impact the top of the shroud at speed due to the curve in the geometry at that location.

The way droplets in the momentum source model travel unhindered through the gap between shroud and cone is illustrated clearly in Figure 4.23, which shows droplet tracks under the shroud for the momentum source model case. In the geometrically representative model most droplets that make it past the inlet impact the gear and are flung onto the shroud at some point along its length. As a result, droplets are more evenly spread across the shroud rather than making it all the way to the gutter unhindered. Essentially what is missing is local interaction with the gear and local velocities.

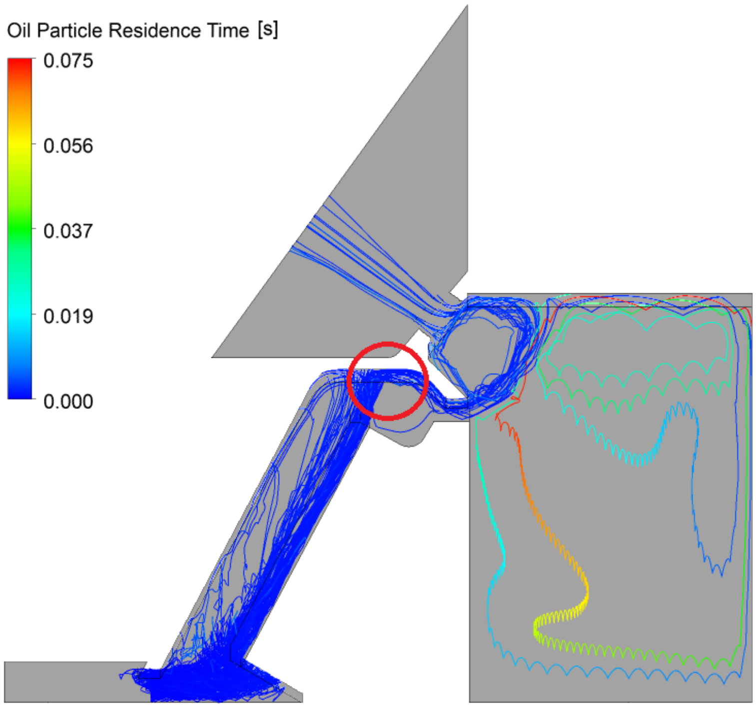

Figure 4.23: Droplet tracks for the momentum source model with droplets injected at the shroud inlet. Location of droplets impacting shroud gutter at high speed is circled in red.

Another key issue relating to the change of geometry is the removal of the tooth valleys. This means droplets have to take a longer route around the solid cone instead of being able to cut through the regions of free space where the tooth valleys would usually be. This is most noticeable at the top of the gear where the flow of droplets is directed straight up to the shroud and restricts the flow of droplets out of the back of the gear. Figure 4.23 shows the high speed jet of droplets impacting the shroud and also the restricted flow region with a lack of droplets. This is further corroborated by the fact that less than 3% of droplets leave at the back of the gear in the momentum source model compared to around 6% in the representative geometry case.

Droplet Release at Into-Mesh Location

Release of droplets at a location representative of those coming from the into-mesh jet reveals a similar picture. The lack of intervening tooth geometry allows droplets to travel much further up the shroud then they would otherwise be able. The histogram data of Figure 4.24 shows a higher concentration of droplet impacts in the shroud gutter whereas the representative geometry model has a much more even spread.

Approximately 6% of injected droplets exit at the back of the gear for the momentum source model and none for the representative geometry case. This shows that the local droplet trajectories have a significant effect on the global droplet transport.

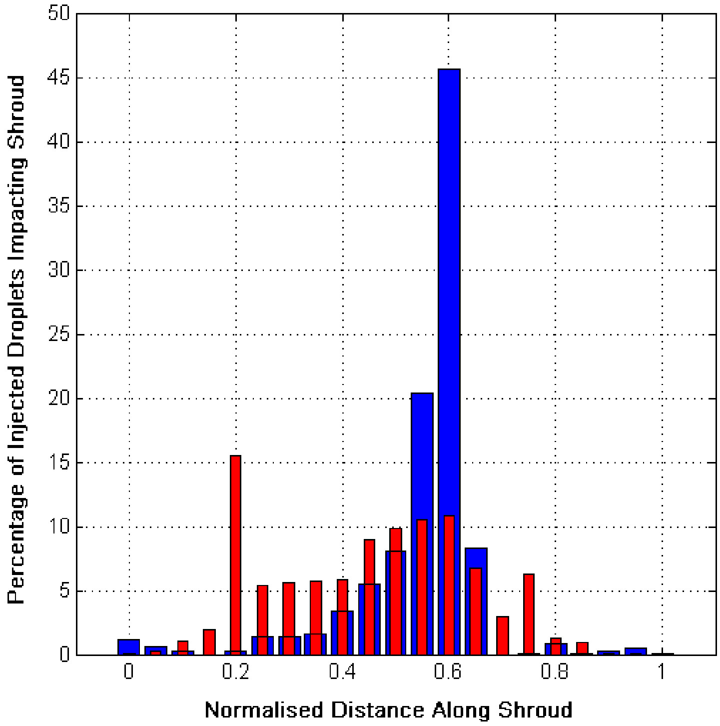

Figure 4.24: Histogram comparing percentage of injected droplets which impact the shroud for the momentum source model (blue) and representative geometry case (red). Droplets are injected representing the into-mesh jet and impact locations on the shroud are non-dimensionalised between 0 and 1. Refer to Figure 4.9 for non-dimensionalised shroud positions.

4.6 Momentum Source Model Conclusions

The aim of this work was to develop a simplified momentum source representation of a gear geometry for CFD calculations in which bulk flow characteristics matched those of a more expensive, geometrically representative simulation. This was successfully achieved in single phase. With the momentum source model formulated in this thesis:

- Bulk mass flow in the momentum source model has been matched to that of the full tooth model (within 4%).

- Mean velocities are modelled accurately (within 1.5% at the shroud restriction).
- It is possible to use a momentum source approach for single phase flow provided good data for calibrating the model is available.

Further studies have shown that the momentum source model can easily be integrated as part of a full chamber model in single phase. This suggests a possible route to a full IGB model.

From the results presented it is apparent that the momentum source model does not allow droplet impact and detailed droplet behaviour under the shroud to be modelled. This is not unexpected given the significant differences in local flow behaviour. The momentum source model has been shown capable of modelling bulk behaviour for single phase flow [10]. It is yet to be shown whether bulk behaviour for two-phase flow can be reproduced as to do this is would be necessary to have reached a steady state condition for the film model case running transiently. With the current resources available, the simulation takes approximately 72 hours to model one complete revolution of the gear. It is unknown exactly how many revolutions are required for the shroud to reach a steady state condition. A secondary issue is that tracking upwards of 500,000 individual particles is very memory intensive, simulating beyond this density of particles is beyond the capabilities of the available resources. With that in mind, the modelling of other aspects of an IGB were prioritised for the remainder of the PhD. It is possible that the momentum source model would eventually reproduce the correct overall oil flow rates at representative velocities and that this would enable a representative model of an IGB to be created (without the under-shroud detail). However further work is necessary to fully establish this.

This chapter has presented CFD research that assesses the capability of a momentum source representation of a shrouded spiral bevel gear to model two-phase flow behaviour. To do this a CFD model of a geometrically representative shrouded gear geometry has been generated and appropriate computations conducted. These computations show that:

- Oil droplets injected at the inlet to the shroud representing oil flow from the external chamber tend to impact towards the lower part of the shroud near the inner diameter
- Oil droplets injected from a gear tooth flank, representing the into-mesh jet, tend to impact relatively evenly along the shroud
- Where a film model is applied, overall oil motion is seen to be towards the top of the shroud for droplets injected at the tooth top land location.

It is identified that further work using the film model would be desirable to enhance knowledge and understanding.

Droplets released within the momentum source model did not impact at the same locations as for the geometrically representative model. The main reasons for this are:

- The majority of droplets are caught in a fast fluid flow and, unhindered by the tooth geometry, do not impact shroud as early as they should.
- The lack of tooth valleys prevents the droplets from exiting at the shroud restriction driving them instead to impact in the shroud gutter region.

Work has not been conducted within this PhD project to assess the ability of the momentum source model to simulate the bulk transport of droplets, which is the key for a simplified gear representation in two-phase. Further work in this area is recommended.

The single phase sections of this chapter, up to Section 4.5.3 have been published in the Proceedings of the XXI International Symposium on Air Breathing Engines, 2013 [10]. The two phase Sections 4.5.4 and 4.5.5 have been published in the Proceedings of the ASME Turbo Expo 2013: Power for Land Sea and Air [11]. Supporting work, informing droplet behaviour at the shroud inlet, has been published in the Proceedings of the ASME Turbo Expo 2014: Turbine Technical Conference and Exposition [54].

Chapter 5

Zonal Coupling Study

Though it is known from experimental work [23] that an IGB is a system and needs to be modelled as such, an important question is: is it possible to study regions in isolation before recombining them into a complete model? This Chapter investigates this with a study into the gear windage test rig geometry, a representation of part of an IGB. The sensitivity of the windage rig flows to variations in velocity and geometry at the boundaries of the three distinct windage rig regions is investigated and recommendations about the benefits and limitations of a zonal modelling approach are discussed. The effect of these parameters on system performance will also be noted.

5.1 The Zonal Approach

The gear windage test rig can be roughly divided into three key regions:

1. The gear and shroud subsystem (investigated in Chapter 4)
2. The rear chamber behind the gear (modelled in Chapter 4 and more thor-

oughly investigated in Chapter 6)

3. The main chamber

These regions are depicted in Figure 5.1 and are bounded at the shroud inlet (zones 3 and 1), the shroud restriction (zones 1 and 2) and the shroud outlet holes (zones 2 and 3). These boundaries will be studied in this chapter to discover if it is possible to decouple each region from the full system. There would be a significant computational benefit to this approach, as each region could be investigated individually without having to model the full system each time. This would allow small parametric changes to be investigated quickly before being simulated in a full model and thus aid design.

All work in this chapter was conducted in single phase.

Two strands of investigation were conducted, in the first case swirl at the shroud inlet was varied and the response throughout the system measured. In the second case the geometry around a boundary was varied.

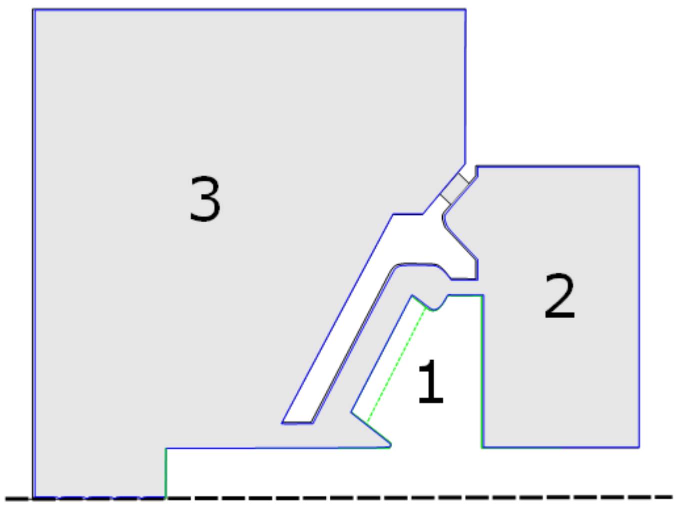

Figure 5.1: Diagram showing the three main regions in the gear windage test rig: 1. the gear and shroud subsystem, 2. the rear chamber and 3. the main chamber.

5.2 Computational Model

5.2.1 Model Geometry

The model simulated in the inlet swirl investigation is geometrically the same as the full tooth model studied in Chapter 4. Its geometry formulation is described in Section 4.3.1.

In the second investigation two geometry features are varied, the shroud geometry and the rear chamber outlet. These variations are discussed in detail in Section 5.4.

5.2.2 CFD Methodology

As with the geometry, the CFD methodology is the same as described in Chapter 4. There are however key differences to the inlet and outlet boundary conditions.

In the swirl investigation the shroud inlet boundary is defined as a pressure inlet with a specified tangential velocity component. This simulates air entering the domain from the main chamber with some element of pre swirl.

In the geometry investigation the inlet and outlet of the domain remain defined as pressure boundary conditions, both set at atmospheric pressure (0 Pa gauge pressure). Due to the geometry change between models, the hydraulic diameters required to correctly determine turbulence are adjusted as appropriate.

5.3 Inlet Swirl Investigation

The work in this section explores the notion that the environmental conditions found within the IGB main chamber must be considered in order to correctly understand and model the flow through a shrouded gear. It is postulated that the amount of swirl velocity the flow possesses, when drawn under the shroud from the main chamber, will affect the flows under the shroud and therefore affect overall IGB performance. Due to the highly swirled flow evident in an aeroengine bearing chamber, the flow into the shrouded gear tooth subsystem will already have some element of swirl before it is then swirled further by the gear. It was not known a priori how much effect this would have, in particular on the flow exiting the gear/shroud system, as Webb's study [31] [24] used an idealised geometry and applied no swirl at the shroud inlet. Johnson [7] has compared a spiral bevel gear to a centrifugal fan and the benefits of pre swirled inlet air in reducing load on a centrifugal fan, via radial inlet vanes, is well documented [65].

The effect on computed flow field of the amount of swirl present at shroud inlet was assessed by varying inlet swirl number, which is defined as the ratio of the tangential velocity component to the axial velocity component:

$$S = \frac{w}{u} \tag{5.1}$$

Table 5.1 shows the cases run in the present study and their Swirl Number.

Table 5.1: Cases run and their inlet swirl velocity values.

Case	Inlet Swirl Number
1	0.00
2	0.12
3	0.44
4	0.89
5	1.37
6	1.87

Velocity profiles were compared at several positions in the domain, as shown in Figure 5.2. The progression of the azimuthal velocity profiles through the shroud inlet (Position 1), the bottom of the teeth (Position 2), top of the teeth (Position 6) and at the shroud outlet (Position 8) are shown in Figure 5.3. The profiles at positions 7 and 8 also gives insight into the possible decoupling of zones 1 and 2 and zones 2 and 3 respectively.

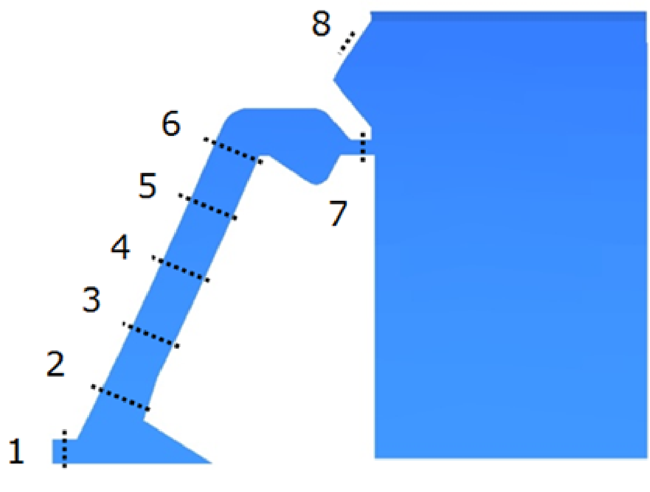

Figure 5.2: Side view of model domain showing locations of data comparison through the tooth region and at the shroud restriction.

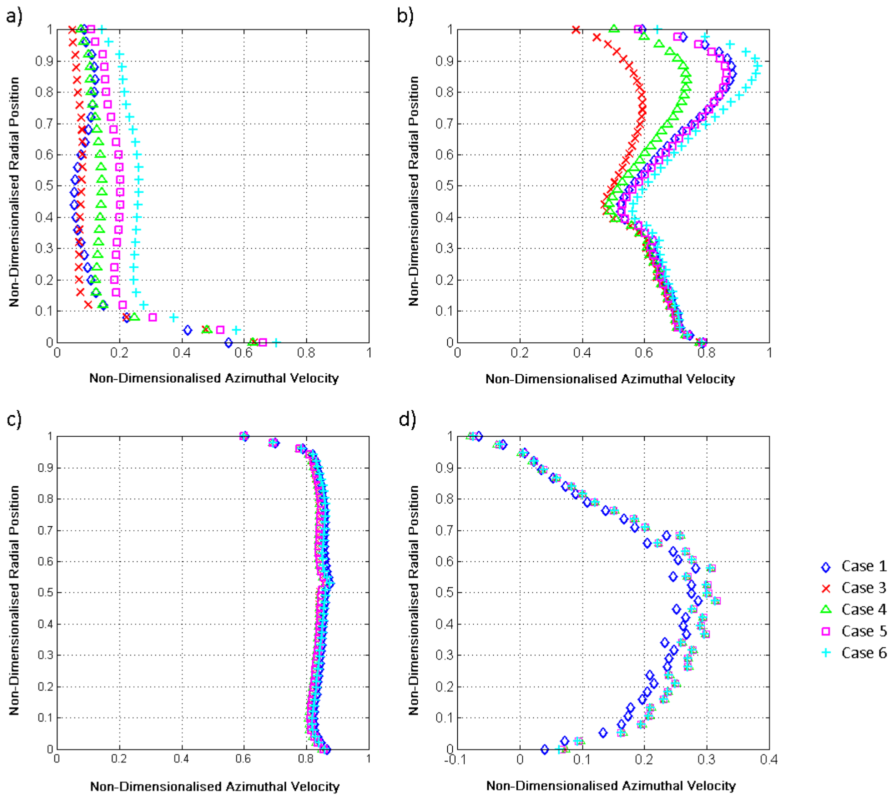

Figure 5.3: Plot of the azimuthal swirl velocity at a) the shroud inlet (Position 1), b) the bottom of the tooth valley (Position 2), c) the top of the tooth valley (Position 6) and d) the shroud outlet (Position 8) for 5 different full tooth models, each with a different inlet swirl velocity.

There is clear evidence that initial large differences in azimuthal velocity become significantly smaller as the fluid is swirled by the gear; with very little difference in azimuthal velocity profile evident by the top of the gear teeth (Figure 5.3c, position 6). Initial average azimuthal velocity difference between Cases 2 and 5 is 152% at Position 1. At Position 2 this is reduced to 33%; at Position 6 it is 2%; at Position 7 it is 1.2% and finally at Position 8 it is 0.5%. An important conclusion from this study is therefore that the swirl exiting at the shroud restriction and shroud outlet hole are essentially independent of the amount of swirl at the system inlet.

These results clearly imply that in single phase for a given geometry and gear rotational speed zone 2 can be decoupled from zones 1 and 3 and a boundary condition can be used at the shroud restriction to study the rear chamber independently.

In addition to this conclusion, swirl does have an effect on other bulk flow properties. Figure 5.4 shows how non-dimensionalised gear torque C_m, defined in Section 3.5, varies with swirl number. Gear windage is commonly linked to fan theory, which states that swirl will have some effect on both gear torque and mass flow rate. Due to momentum transfer, torque should decrease as swirl in the direction of the gear rotation increases. This can be seen in Figure 5.4 for swirl numbers greater than 0.5. Increasing inlet swirl number from 0.44 to 1.87 gives a 7.6% decrease in gear torque.

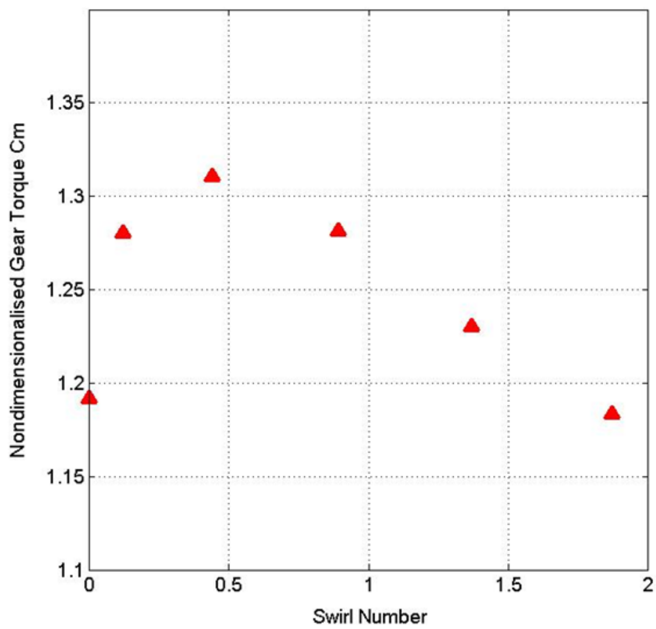

Figure 5.4: Graph showing the effect of inlet swirl on gear torque through the full tooth model.

Since windage power losses are a function of the mass flow rate pumped by the gear [7] it is important to quantify the impact. Figure 5.5 plots non-dimensionalised mass flow rate against swirl number, where mass flow has been non-dimensionalised relative to the mass flow of the zero pre-swirl Case 1 as follows

$$\dot{M}_{nd} = \frac{\dot{M}_n}{\dot{M}_1} \tag{5.2}$$

where $\dot{M}_{nd}$ is non-dimensionalised mass flow rate, $\dot{M}_n$ is the mass flow rate for that case and $\dot{M}_1$ is the mass flow rate of Case 1.

Figure 5.5 shows how mass flow rate varies with inlet swirl and follows the same trend as gear torque. The drop in mass flow rate for swirl numbers above 0.5 is caused by an increased recirculation back down the shroud as swirl increases, see Figure 5.6. However, swirl affects mass flow rate to a lesser extent than it does gear torque, an increase in swirl number from 0.44 to 1.87 produces only a 3.8% decrease in mass flow rate.

From Johnson's experimental work [7] it has been seen that approximately a 25% increase in mass flow rate equates to a 10% increase in gear torque. Therefore the 3.8% decrease in flow rate noted here has only a minimal impact on torque.

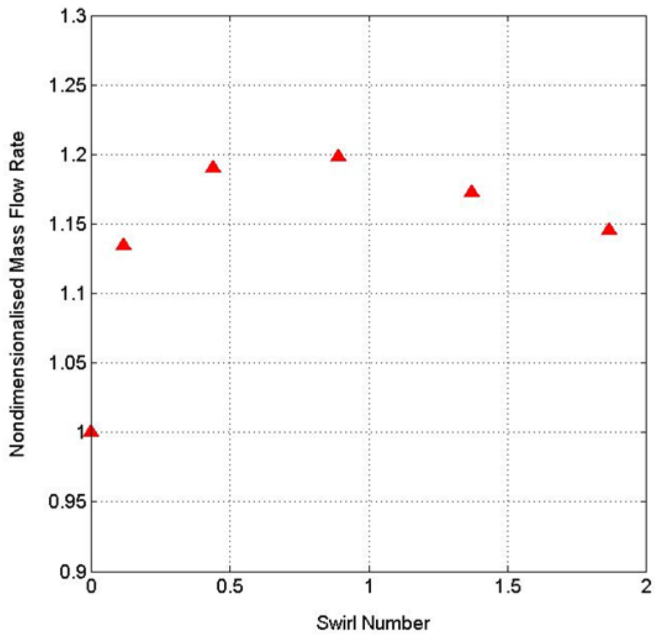

Figure 5.5: Graph showing the effect of inlet swirl on mass flow rate through the full tooth model.

Figures 5.4 and 5.5 both show two distinct trends as swirl number increases. The first is an increase in torque and mass flow as swirl number increases up to 0.44, the second is a decrease in torque and mass flow as swirl number exceeds 0.44. Figure 5.6 shows velocity vectors for Cases 1, 3, 5 and 6 at the shroud inlet which explains these trends.

Case 1 (Figure 5.6a) displays a large recirculation at the shroud inlet which restricts the mass flow into the shroud. As the inlet swirl number is increased this recirculation is reduced (Figure 5.6b) allowing a larger area of the flow to enter the shroud, thereby increasing mass flow.

However increasing the inlet swirl also results in an increase in recirculation of the flow back down the inner surface of the shroud. This recirculation stays attached to the shroud surface for longer and hinders the flow being drawn in by the gear (Figures 5.6c and 5.6d).

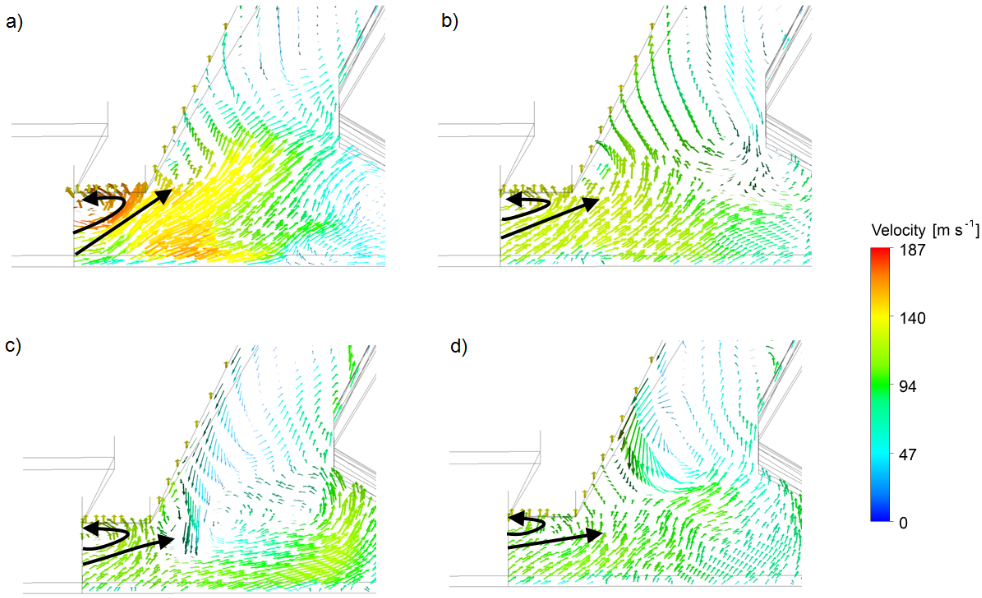

Figure 5.6: Velocity magnitude vectors at the shroud inlet for Cases 1, 3, 5 and 6. The black arrows display the direction of the flow entering the shroud.

It can therefore be said that two distinct flow behaviours exist, both of which hinder mass flow through the gear/shroud subsystem. The point at which these hindering mechanisms are both minimised exists at approximately 0.5 inlet swirl number (Figure 5.6b) where a maximum value for mass flow and gear torque are achieved.

5.4 Shroud Restriction Geometry Investigation

Having established that for a given geometry it is possible decouple zone 2, it is now important to assess the effect geometry changes have on the system. It is also of benefit to understand how the shroud outlet affects the upstream flow through the shrouded gear system.

There are two key differences observed between the results from the current model and that of Webb. The full tooth model presented here models a shroud used in recent experimental work by Johnson [26] (designated as 'new shroud' models) whereas Webb's model used a different configuration of shroud also used by Johnson [7]. Webb's geometry also has an open chamber behind the gear whereas in the current geometry this chamber is far more restricted; the flow is only able to leave from small outlet holes.

In order to evaluate the effect of the model outlet condition on the flow, a four model parametric study was conducted. Two new shroud models, one with a restricted chamber (Case A from the present study) and one with an open chamber (Case B) are compared to two Webb shroud models, one with a restricted chamber (Case C) and one with an open chamber (Case D as described in Webb's work [24]). The geometries for these four models can be seen in Figure 5.7 and are tabulated for reference in Table 5.2.

Table 5.2: Cases run and their key geometry features.

Case	**Shroud Type**	**Chamber Type**
A	New	Restricted (shroud slots)
B	New	Open
C	Webb	Restricted (shroud slots)
D	Webb	Open

The result of this study compares all velocity components at the shroud restriction, as seen in Figure 5.8. This figure shows that axial velocities at the shroud restriction are clearly related to the shroud geometry, rear chamber geometry and the outlet geometry.

The new shroud displays higher axial velocities than Webb's shroud, approximately 18% faster in the restricted case and 43% faster in the open case. Re-

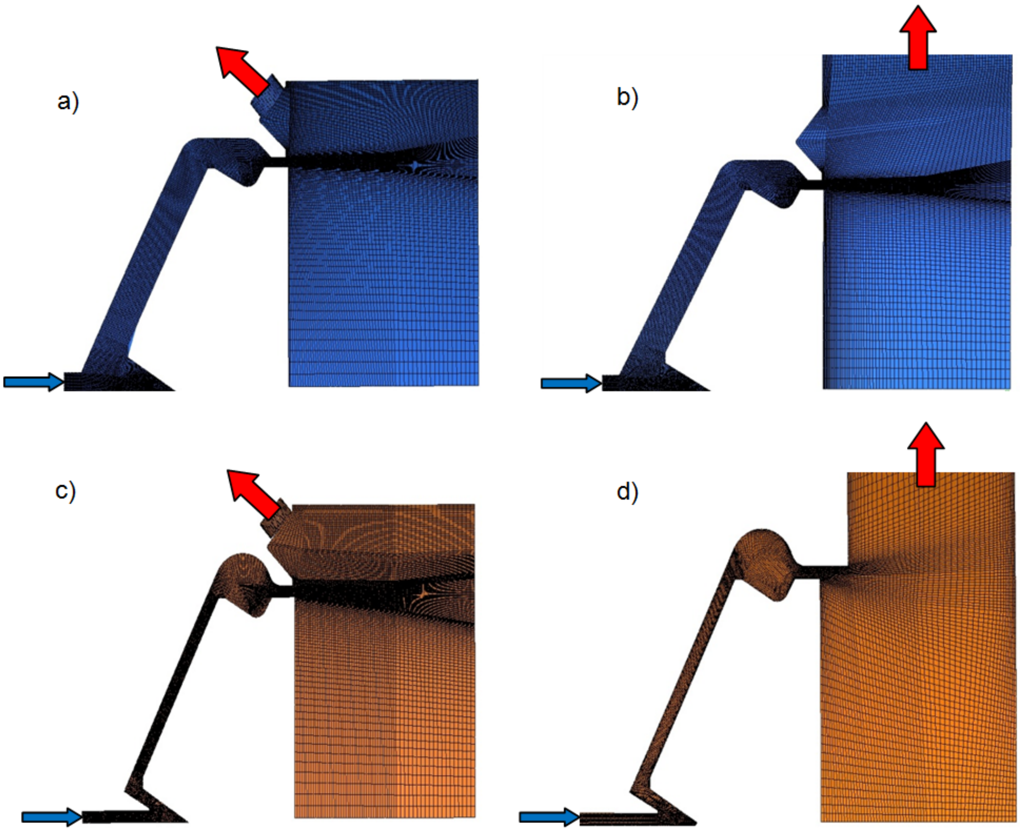

Figure 5.7: Four different models with varying shroud and outlet geometries. a) New shroud with restricted outlet (Case A), b) New shroud with open outlet (Case B), c) Webb's shroud with restricted outlet (Case C), d) Webb's shroud with open outlet (Case D). Blue arrows show flow into the domain and red arrows show flow out of the domain. a) is the present study case; d) is typical of Webb's work.

stricting the outlet results in a very large velocity reduction, approximately 42% for Webb's shroud and 47% for the new shroud.

There are significant differences between the radial velocities for each of the four cases too. For the new shroud, the radial velocities are reduced by approximately 45% when the shroud outlet is opened (Case B).

Most interestingly, when the shroud exit top wall extends further into the back chamber, the flow leaving the shroud is forced to remain attached to the wall and, as a result, this significantly dampens the radial velocities. This condition

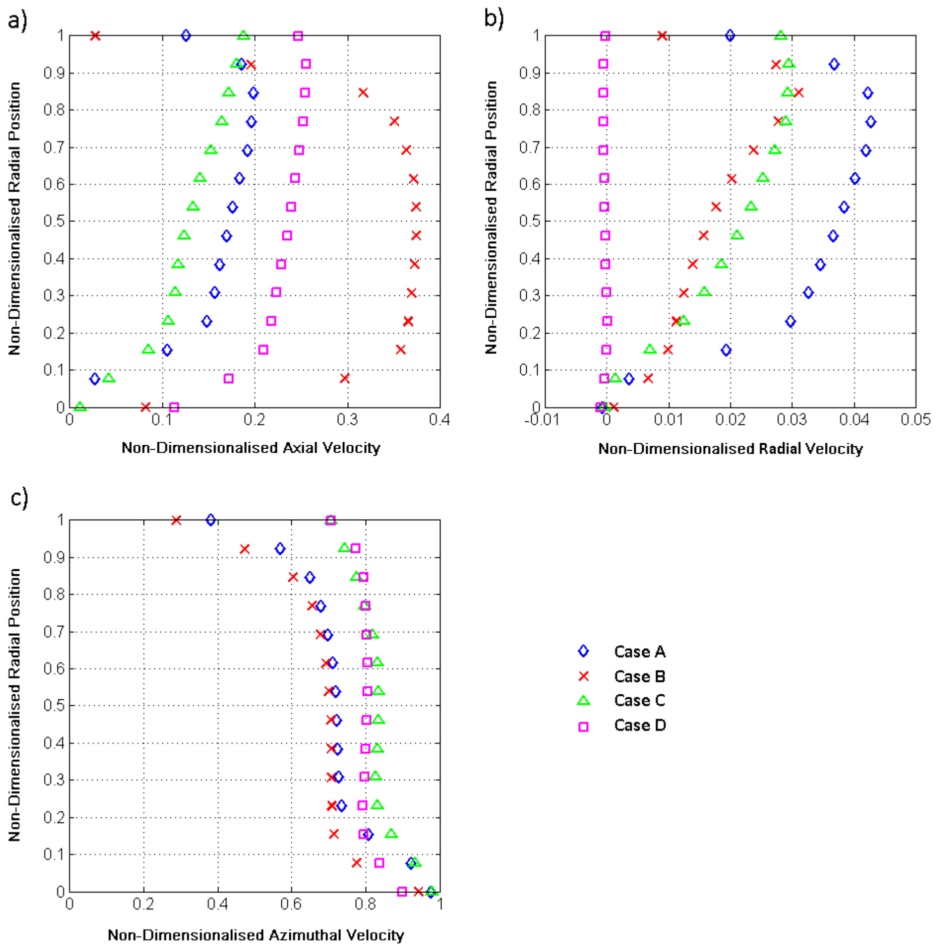

Figure 5.8: Comparison of a) axial, b) radial and c) azimuthal velocities at the shroud restriction for four geometry variations Cases A, B, C and D. Geometry features are described in Table 5.2 for each case.

has only been tested on Case D and is a key difference between this model and Case A, having a significant effect on the velocities in this region.

Comparatively there are no major changes in azimuthal velocity when the outlet is changed, though Webb's shroud displays a higher azimuthal component overall, as seen in Figure 5.8. This difference is approximately 17% indicating that the shroud geometry tested here has a small effect on azimuthal velocities.

The flow structures obtained leaving the shroud are understood to be a function of both the geometry local to the shroud and the geometry of the back chamber exit. A strong interaction between air coming out of the tooth region, the shroud geometry and the shroud outlet is displayed. Mass flow rates are also affected and, for the new shroud, can in fact double when the shroud outlet is open (Case B). See Table 5.3 for mass flow values for each configuration.

Table 5.3: Tabulated mass flow values at the shroud restriction for each case.

Case	**Mass Flow Rate [kg/s]**
A	0.00155
B	0.00310
C	0.00131
D	0.00224

5.5 Zonal Coupling Conclusions

Several practical conclusions can be drawn from the elements of this study:

1. For a given geometry, the swirl exiting a shrouded rotating-gear subsystem at the shroud outlet (position 8) appears insensitive to the swirl entering the gear at the shroud inlet for all likely swirl values (within 0.5%).
2. For a given geometry, the swirl exiting a shrouded rotating-gear subsystem at the shroud restriction (position 7) appears insensitive to the swirl entering the gear at the shroud inlet (within 1.2%).
3. The gear torque decreases as swirl increases, calculated as approximately 7.6% for a 1.42 increase in swirl number.

4. The mass flow rate through the gear is affected by the initial swirl although it only has a marginal overall effect (approximately 3.8%).

5. At low swirl values (below 0.5) separation from the shroud inlet causes increased recirculation back down the shroud and associated decreases in mass flow and gear torque.

6. The flow structures leaving the shroud appear to be a function of both the geometry local to the shroud and the geometry of the back chamber and exit.

Conclusions 1 and 2 imply that, in single phase, the under shroud regions of an IGB can be decoupled from the rest of the main chamber and modelled in isolation.

Conclusions 3-5 show that increased swirl in the outer chamber could result in decreased gear torque and would be a beneficial feature in an IGB.

Conclusion 6 points to the importance of understanding the gear-rear chamber dynamics well as part of a modelling strategy of an IGB. This is particularly important as the rear chamber is typically the location of a large location bearing and a significant source of oil into the IGB.

The work in this Chapter is currently awaiting publication in the Proceedings of the ASME Turbo Expo 2015: Turbine Technical Conference and Exposition [66].

Chapter 6

Rear Chamber Modelling Investigation

Chapter 5 has highlighted the need to understand the rear chamber behind the gear and also established the validity of a zonal approach.

In this chapter results from modelling an axisymmetric sector of the IGB rear chamber are presented. Adjacent to a large location bearing, the rear chamber is the source of a large influx of oil into the IGB system and as such the two phase dynamics in this region is a key concern. Two phase flow behaviour is modelled using both the Volume of Fluid (VOF) and Eulerian models within FLUENT [1]. A comparison between these two multiphase models is made and their suitability to model the oil behaviour in the back chamber is discussed. In conjunction, experimental work conducted by Johnson [67] on the UTC gear windage rig is used as qualitative evidence to support the computational model. A modelling methodology is then presented based on these findings. Oil flow behaviour in this region is reported.

6.1 Experimental Facility

The gear windage test rig at the UTC was designed and built around an existing test bed, gearbox and 130 kW DC motor and is capable of driving the working section shaft bi-directionally at speeds up to 15,000 RPM. The basic facility is shown in Figure 6.1 with the gear and back mounting plate labelled.

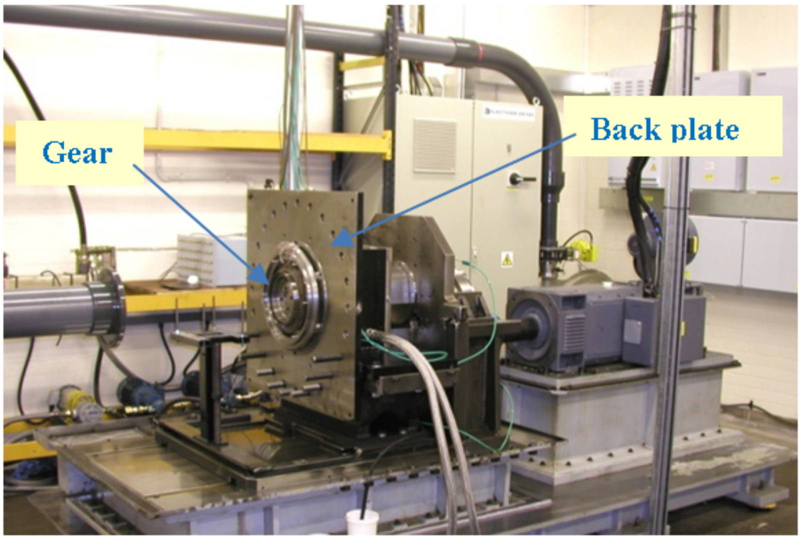

Figure 6.1: UTC gear windage rig - base configuration [7].

In the experimental study of interest the gear was shrouded and an outer transparent chamber was mounted on the back plate. The configuration is as illustrated in Figure 6.2. The shroud contains exit slots that allow oil from the gear and bearing to pass through to the main chamber.

Note that on the test rig there is no location bearing behind the gear. Oil is introduced into this chamber simulating the oil shed from the bearing. The oil is introduced through an annular slot as illustrated in Figure 6.3. The intent with this inlet configuration is that oil will travel up the rear wall of the chamber as a film. Oil flow was varied up to 4 lpm and while the rig is running an additional 0.3 lpm of oil is supplied to the rig slave bearings. This additional oil also enters the rear chamber leaving through the shroud outlet holes.

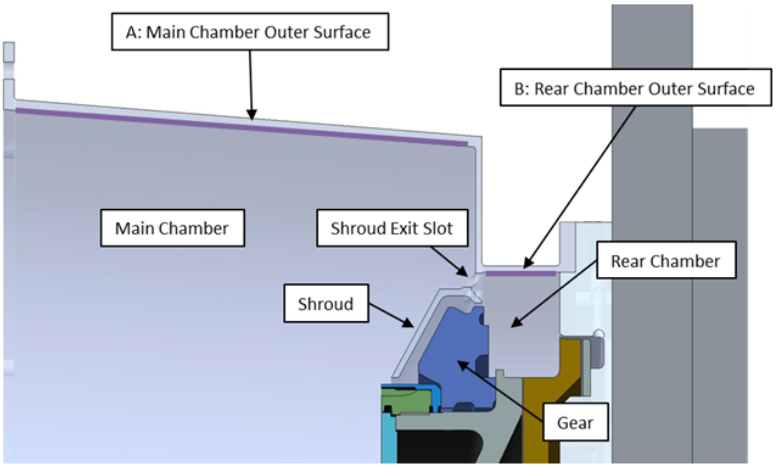

Figure 6.2: Test rig as configured for the rear chamber study [67].

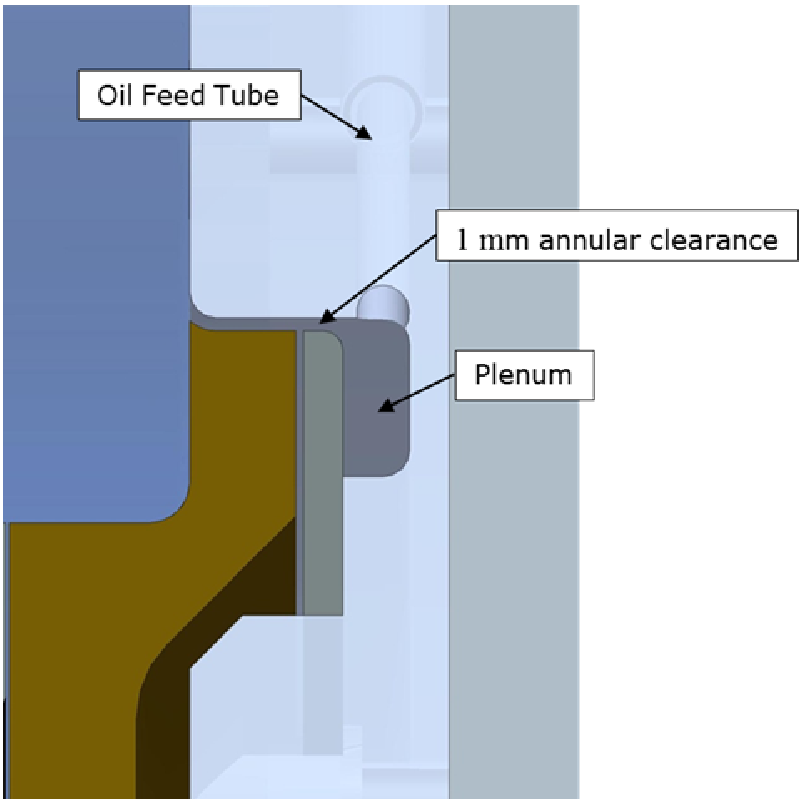

Figure 6.3: Test rig as configured for the rear chamber study [67].

During all the testing conducted in this experimental campaign the rig was run at ambient temperature and pressure. The oil used was Aeroshell 390 and its injection temperature was maintained at 20°C throughout testing.

Film thickness data was collected at the top centre of the back chamber using a Laser Confocal Displacement Meter (LCDM) and video footage was taken at the top, left and right sides of the chamber.

6.1.1 Experimental Results

Figure 6.4 shows a top down view of the experimental rig rear chamber, which is the area enclosed by the red box. This image is a still shot from the recorded video footage. From this view a clearly darker band of oil is seen towards the back of the chamber which means a thicker oil film is present in this region. The black line in Figure 6.4 is drawn at the interface for this band of oil to show this behaviour more clearly. It is difficult to see from the image however the video footage clearly shows the disturbed nature of the film and highlights its highly transient behaviour.

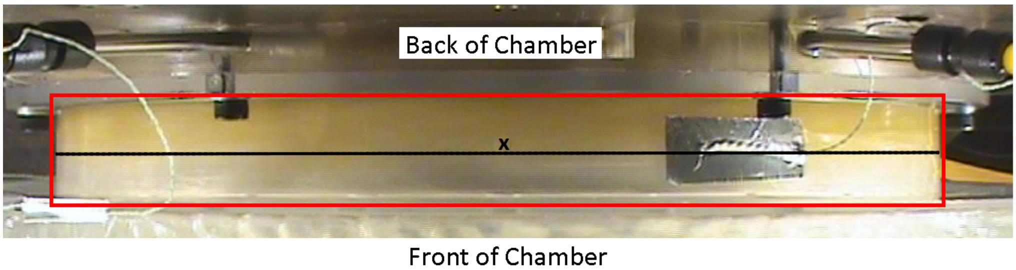

Figure 6.4: Image showing a top down view of the experimental rig rear chamber (enclosed in red) at shaft speed 10,000 RPM and 4.3 lpm oil flow rate. The black line is used to more clearly denote the film interface.

LCDM film thickness measurements were taken at the top centre of the rear chamber, the position of which is marked with an x on Figure 6.4. At 10,000 RPM and 4.3 lpm the film thickness was measured at 0.35 mm. Due to the size of the

LCDM equipment, it was not possible to vary the axial position of the sensor with the current configuration. Unfortunately this means that film thickness measurements were taken very close to the film interface and may not be indicative of the true depth. It was also not possible to give any information on the film thickness distribution. A conservative visual estimate of the oil mass in the rear chamber, informed by the limited film thickness data, is approximately 0.003 kg

The video footage gives some indication that the flow will not be completely axisymmetric. Figure 6.5 shows the left and right side views of the rear chamber at 10,000 RPM. Even at this high rotational speed there is still a bias of oil to the bottom of the chamber. The black lines on Figure 6.5 help to show the oil film interface. This shows that gravity does have some effect on the flow behaviour in the rear chamber though it's influence appears to be minor. It is however difficult to assess the full extent of this influence from the present work.

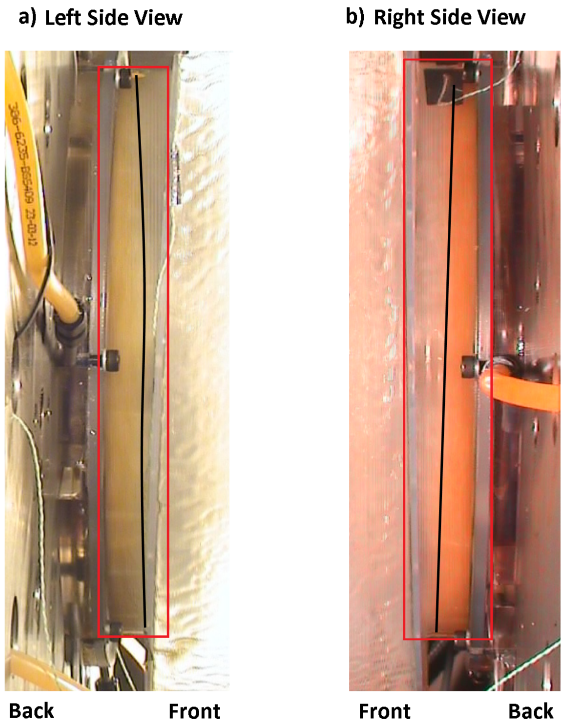

Figure 6.5: Image showing a) the left and b) the right sides of the experimental rig rear chamber (enclosed in red on each image) at shaft speed 10,000 RPM and 4.3 lpm oil flow rate. The left hand side shows shearing flow upwards opposing gravity. The right hand side shows shearing flow downwards in the same direction as gravity. The black line is used to more clearly denote the film interface.

6.2 Geometry Creation

A computational model (comprising a sector with azimuthally periodic boundaries) was created matching as closely as possible the existing UTC gear windage rig rear chamber. The rear chamber is bounded by the gear, shaft, shroud and other stationary walls. The computational domain and these boundaries are shown in Figure 6.6. The plane illustrated goes through the centre of one of the shroud exit slots. The angular extent of the sector is 15.65° as the shroud on the test rig comprises 23 equally spaced slots. This is the same as the sector methodology employed in the models in Chapter 4. The validity of this approach for the rear chamber is detailed in Section 6.3.3. As in the case of the models in Chapter 4, it was not felt to be necessary to model the entire extent of the main chamber and instead a pressure boundary was used. Figure 6.6 shows the pressure boundary in red.

In an aeroengine the majority of oil entering the back chamber comes from the location bearing. In the UTC test rig there is an oil inlet to the back chamber through an annular slot which simulates bearing oil (see Figure 6.3). A similar oil inlet feed was applied in the CFD model.

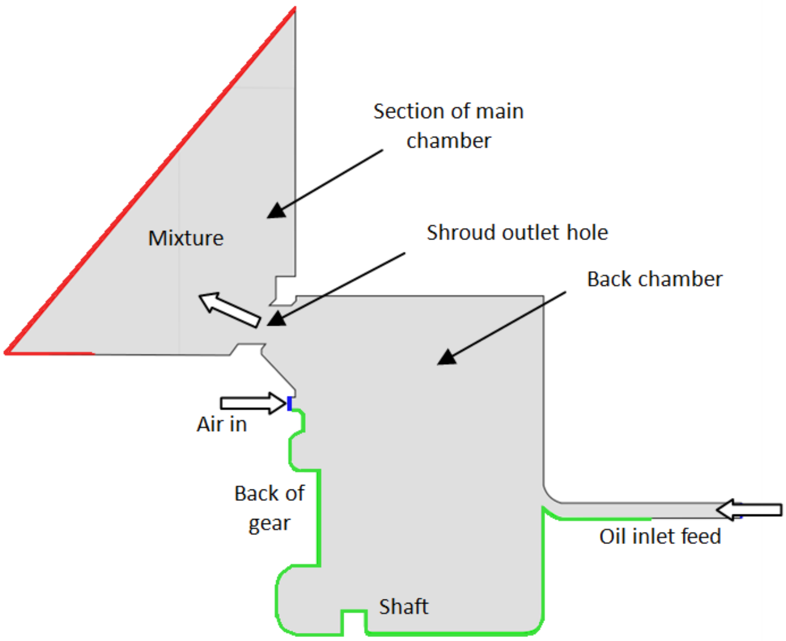

Figure 6.6: Side view of the rear chamber computational domain.

6.3 Single Phase Investigation and Mesh Optimisation

6.3.1 CFD Methodology

Prior to the multiphase calculation, an initial, single phase air flow solution was calculated. A mesh independence study was conducted based on this single phase model and is reported in this section.

Boundary Conditions

The inlet of air entering the domain from the gear was set as a velocity inlet with velocity components taken from a single phase CFD model of the gear [11]. The oil inlet was initially set as an air velocity inlet with a small velocity of 0.1 m/s. The outlet is set as a pressure outlet at atmospheric pressure. This boundary is sufficiently far away from the region of interest not to cause numerical issues due to backflow. Other boundary conditions are primarily set as stationary walls or rotating walls (rotating walls are shown in green on Figure 6.6). The rotating wall was initially set to rotate at 5,000 RPM to ease convergence before increasing to 10,000 RPM. The front and back faces of the geometry are set as rotationally periodic boundaries.

Turbulence Model

The k-ϵ RNG turbulence model, as developed by Yakhot & Orszag [47] and implemented in FLUENT, was chosen for its documented strength in modelling swirled flows. The SST k-ω model was considered but rejected as it switches to standard k-ϵ away from the walls and it is known that k-ϵ does not cope well with swirling flows. The air was modelled as incompressible as its Mach number does not anywhere exceed 0.3. A second order upwind scheme was used for spatial discretisation, which reduces numerical diffusion and improves accuracy whilst limiting the need for too fine a grid.

Convergence

Convergence was determined by monitoring continuity, velocity and turbulence residuals and the moment coefficient for the rotating surfaces. The single phase solution with a grid of 1.6 million cells took approximately 4 hours to converge on 16 Intel Xeon E5472 3.0GHz CPUs.

6.3.2 Mesh Independence Study

A mesh independence study was conducted to identify an appropriate mesh density for the calculations. Five meshes were investigated ranging from 0.32 million cells to 1.6 million. The upper range of these meshes was determined from Tkaczyk's work [68] which advises 10 cells within a wall bounded film to fully define the film profile. The meshes are tabulated against their identifier in Table 6.1.

Table 6.1: Mesh designations and number of cells.

Mesh Designation	Number of Cells in Domain
M1	1,600,000
M2	1,200,000
M3	700,000
M4	400,000
M5	320,000

In order to compare data for the 5 meshes average velocity profiles were created from a plane at the shroud outlet and 3 vertical planes within the rear chamber. The locations of these planes are depicted in Figure 6.7, and profiles of velocity magnitude for the 5 meshes at Position 1 can be seen in Figure 6.8.

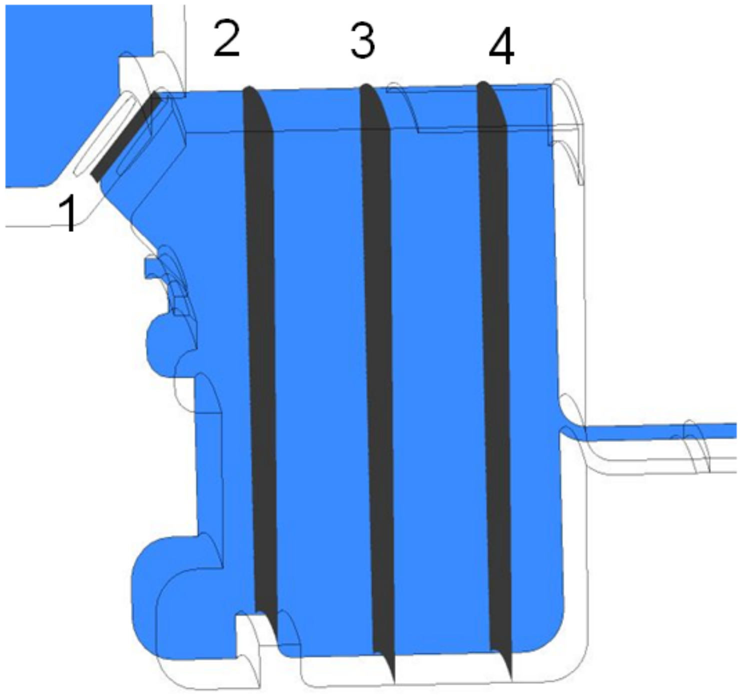

Figure 6.7: Image showing the rear chamber and planes of comparison, shown in black.

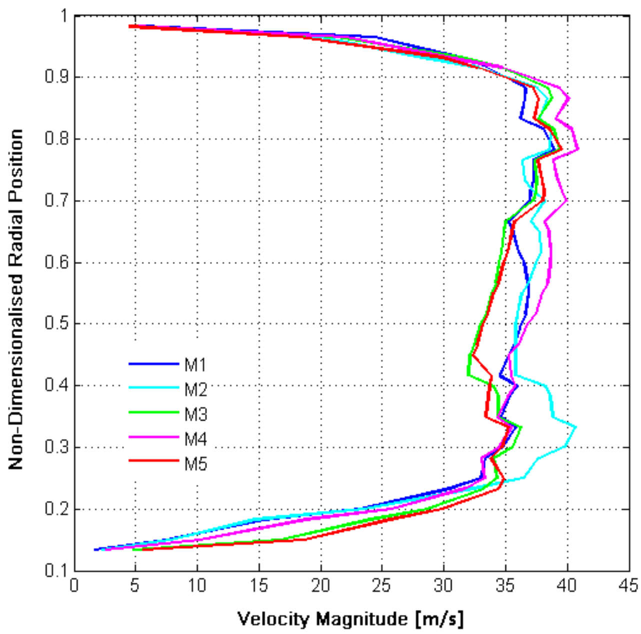

Figure 6.8: Velocity magnitude profile at the shroud outlet hole for each mesh.

The mean velocity magnitude for each mesh at Position 1 is presented in Table 6.2 along with the percentage difference from mesh M1 (the finest mesh) and an L2 measure. The L2 measure is calculated as

$$L2measure = \sqrt{\frac{\sum (u_{M1} - u_{Mn})^2}{\sum {u_{M1}}^2}}.100 \tag{6.1}$$

Table 6.2: Velocity magnitude averages and error from control mesh for each case at position 1 (shroud outlet hole).

Mesh Designation	**Average Velocity Magnitude [m/s]**	**% Difference**	**L2 Measure**
M1	31.9	-	-
M2	32.7	2.8	6.6
M3	32.1	0.8	8.8
M4	33.1	3.9	5.7
M5	32.1	0.8	10.3

Comparison of the velocity profiles at Position 1 (Figure 6.8) shows typical converging behaviour; velocity profiles appear to converge to a central solution profile as the mesh density is increased. Analysis of the velocity vectors shows that all air flow structures appear to be similarly modelled above 400,000 cells. For the lowest mesh density (M5) the majority of velocity vectors are consistent with the higher density meshes however some loss of vortex resolution is evident, as marked on Figure 6.9. The velocity magnitudes of these structures are also all consistent.

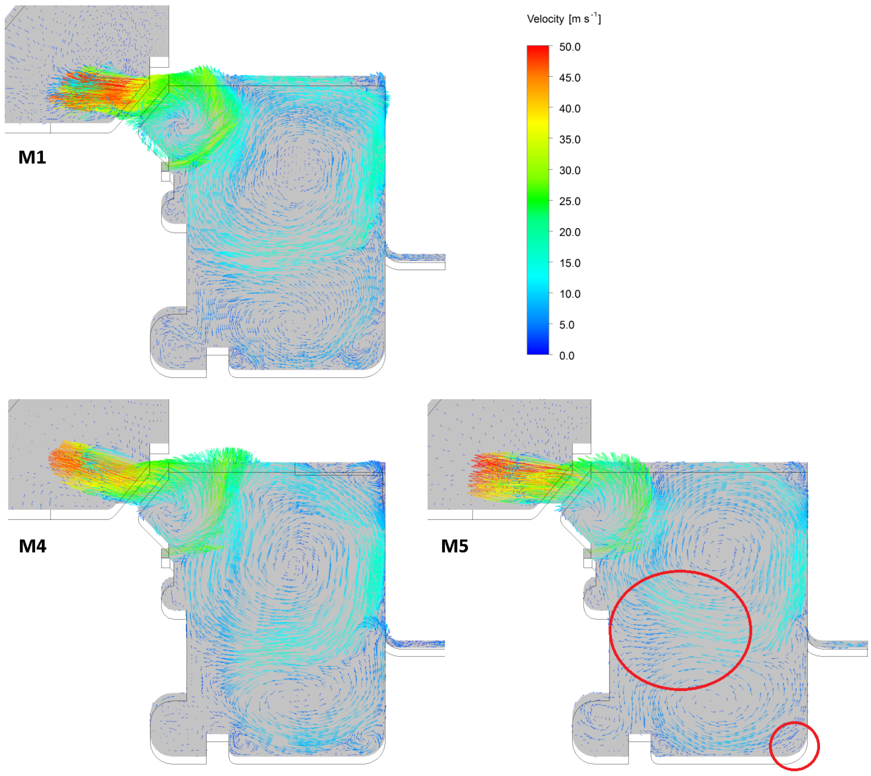

Figure 6.9: Comparison of velocity magnitude vectors for the M1 (1,600,000 cells), M4 (400,000 cells) and M5 (320,000 cells) mesh independence models.

It is clear both from the velocity profiles and average velocity data that there is minimal difference between the solutions for resolutions above 400,000 cells (M4). The maximum difference at this resolution is only 3.9% (see Table 6.2) and is otherwise below 3%. The velocity profiles also display consistent behaviour as indicated by the low L2 values. Data from the other planes was analysed in addition to that from Plane 1 presented here and the M4 mesh consistently gives the lowest L2 values, the maximum being 5.7% at the shroud outlet. Consequently the 400,000 cell mesh (M4) was progressed to the two phase work.

The computed air flow in the chamber is illustrated in Figure 6.10 where vectors of velocity magnitude are displayed. As can be seen, flow from the back of the gear is the driving force for the flows in this region. The jet curves up towards the top of the chamber, splitting on the outer rim and driving the chamber flow from front to back along the outer face and down the back wall towards the oil inlet. Towards the front of the chamber this flow contributes to a small but strong vortex cell at the shroud hole which then leaves through the hole as a jet.

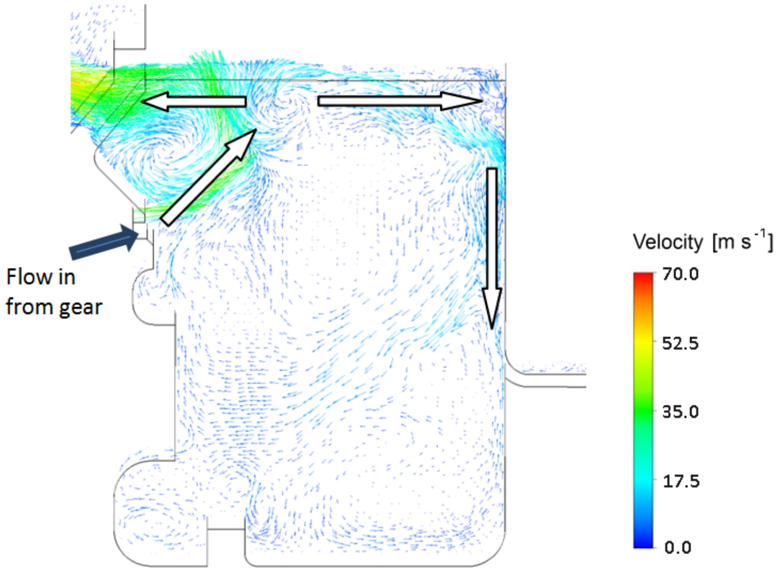

Figure 6.10: Image showing the secondary flow (azimuthal component removed) in the rear chamber. Block arrows show the bulk direction of flow.

6.3.3 Validity of Axisymmetric Sector Model

In single phase, gravitational forces play a very minor role and it is therefore valid to neglect them for high shear flows. This is not necessarily the case for two phase flows where inertial forces are relatively more significant. With a sector model it is clearly not possible to include gravity and this is valid only where the shearing effect of the rotating air flow is dominant.

Based on work by Kay [69] it can be assumed that gravitational effects are negligible when gravitational parameter $\lambda \lessapprox 5$ where

$$\lambda = \rho g h_{film}^2 / \mu U_{film} \tag{6.2}$$

ρ is oil density, g is the gravitational constant, h_{film} is oil film thickness, μ is dynamic viscosity and U_{film} is fluid film velocity. Film velocity has been measured experimentally by Chandra [70] to be 3.5 m/s for similar geometries and flow rates to the present model. Consequently, a film thickness of 7.3 mm satisfies the condition $\lambda = 5$ indicating a shear driven rimming flow. From the experimental work described in Section 6.1.1, film thickness for the present model was predicted to be of the magnitude of 0.35 mm and significantly lower than the critical 7.2 mm thickness. As a result it was thought that the two phase flow would be largely shear dominated and that gravitational effects would be secondary. This justified the use of the segment modelling approach.

The velocity profile on a radial line approximately equidistant from front and back walls (plane 3 as illustrated in Figure 6.7) is shown in Figure 6.11. Here the velocity gradient is seen to be steep at the outer radial positions, lending weight to the assumption the flow would be shear driven.

From the experimental work described in Section 6.1.1 gravity does appear to have some influence on the flow. Based on the distribution of oil in Figure 6.5 this influence appears to be minor however it is difficult to assess fully. For this study a decision was made to use a sector model because of the prohibitive size of a full 360° calculation. It was believed that modelling the rear chamber without gravity would only have a minor effect on the flow behaviour.

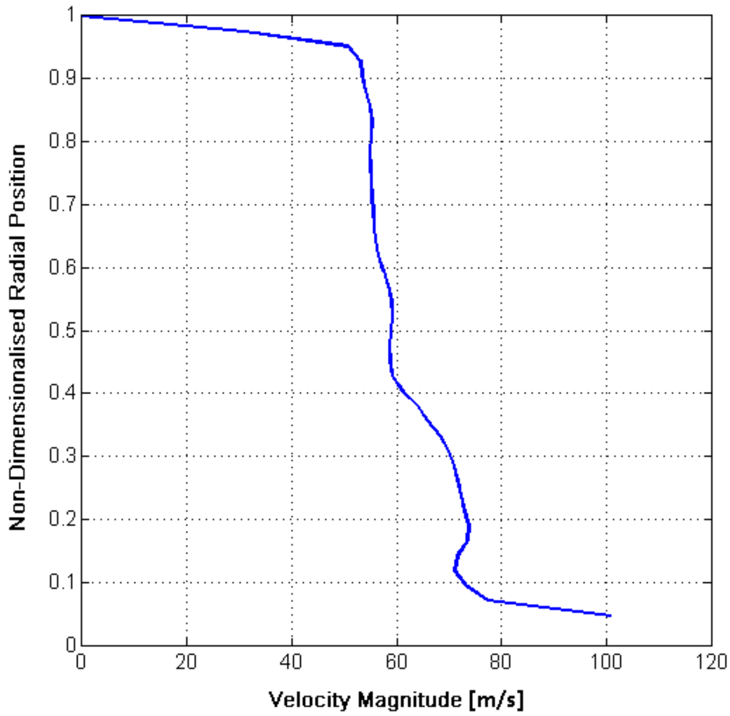

Figure 6.11: Graph showing the azimuthal velocity profile across the rear chamber for a single phase simulation at 10,000 RPM. Data is taken from position 3 (see Figure 6.7).

6.4 Two Phase Investigation

In this section an oil phase is added to the simulation. Two different multiphase models available within FLUENT were studied, the Volume of Fluid model and the Eulerian model. All two phase solutions were obtained for a shaft speed of 10,000 RPM using the 5,000 RPM single phase solution as a starting point.

6.4.1 Volume of Fluid (VOF) Model

A first attempt at modelling the two phase behaviour in the rear chamber utilised the Volume of Fluid approach. The VOF model is an Eulerian type multiphase model that calculates a volume fraction of a fluid phase, or number of phases, for each cell in the computational domain. In this way it is able to track the interface between multiple phases. It is one of the least computationally expensive multiphase models and this is beneficial for very large simulations. The VOF approach is particularly suitable for flows where there is a clear interface between two fluids of significant difference in density. Initial predictions based on the experimental work (see Section 6.1.1) projected that the majority of the oil within the rear chamber would be on the walls and that the oil in the core flow, that was perhaps not adequately represented in the VOF approach, would not significantly affect the overall solution obtained except in minor details. A full description of the VOF model can be found in Chapter 3.

VOF Methodology

The VOF two-phase calculation was started from a converged single phase solution. The oil inlet was set as a mass flow inlet with the mass flow rate set as 0.0033 kg/s equivalent to the 4.3 l/min flow rate used experimentally.

Although the final solution is steady state, a transient approach is required in order to achieve convergence. During early parts of the calculation oil from the inlet fills the chamber until a steady state condition is reached in which there is an amount of film on the walls and some oil in the core flow. It is anticipated that once steady state is reached there is a permanent volume of oil in the chamber and oil inflow matches oil outflow.

As previously explained in Section 3.8.3 an implicit VOF approach is preferable as it generally allows larger time steps to be used than in the explicit formulation thus achieving convergence more quickly. However it proved impossible to achieve convergence for this complex flow with an implicit approach and thus the explicit VOF approach was selected. This scheme incorporates the volume fraction from the previous time step into the equation and does require a typically much smaller time step. To maintain a recommended Global CFL condition of 2 [57], a variable time step was used where FLUENT calculates each time step to satisfy the condition $CFL = 2$. Typically time steps calculated were of the order of 5x10^{-6} s. In addition the VOF time step size is controlled by the Courant number, C, where $C = 0.25$ [57]. This allows the volume fraction to be calculated for several time steps within each global time step.

When using the explicit scheme, FLUENT recommends using the Geometric Reconstruction Scheme to interpolate for values near the fluid interface [42] using a piecewise linear approach. This assumes that the interface has a linear slope within each cell and is used when calculating advection through the cell faces. However, for the results presented here the modified High Resolution Interface Capturing scheme was employed during the early part of the calculation as, although this method is less accurate at calculating the free surface, it converges much faster and allows a larger time step to be used [42]. During initial stages where oil is filling the chamber it is argued that overall numerical precision is less important than minimising the run time. Once this has been achieved a switch to the geo-reconstruct scheme allows for improved accuracy for the final model.

Surface tension and Level Set models were included in the simulation following [68]. In conjunction with the Level Set function, FLUENT can only use the Continuum Surface Force model developed by Brackbill et al [59] where the surface tension is defined in terms of the pressure difference across the fluid surface. The Level Set function, coupled with the VOF model, is designed to track the fluid interface and gives an accurate estimate of both the interface curvature and surface tension as a result of curvature.

Initial VOF calculations showed that the chosen 0.4 million cell mesh was not fine enough to resolve the two-phase flow adequately. Mesh refinement, primarily at the walls where a film was expected to develop, was conducted resulting in a final mesh of 0.9 million cells.

VOF Results

Figure 6.12 illustrates the behaviour of the oil phase calculated using the VOF model. As a result of the driving air flow reported above the air flowing down the back wall of the chamber has a significant effect on the oil entering from the bearing as the opposing air flow prevents a film forming and travelling up the back wall. This counter flow contributes to break up of the oil as it enters the rear chamber. The VOF model struggles to simulate these conditions and the result is a much dispersed, low volume fraction mist.

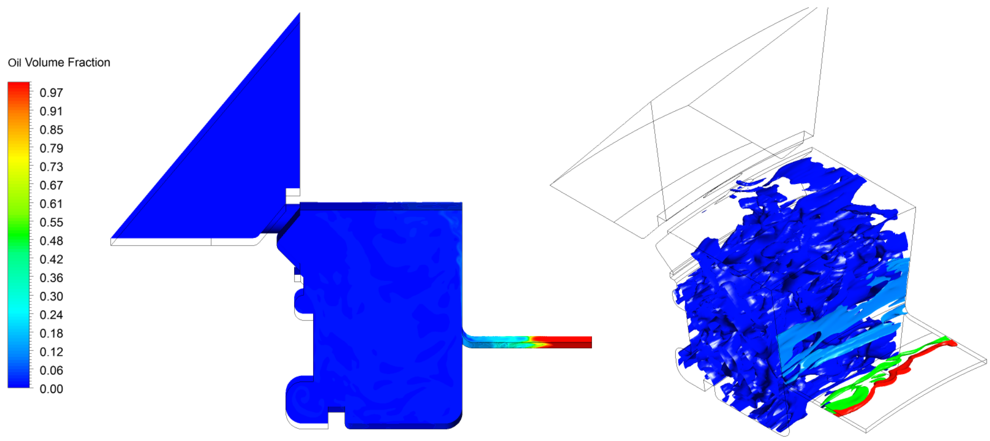

Figure 6.12: Image showing contours of oil volume fraction in the rear chamber for the VOF model. The left hand side shows contours through a plane through the centre of the domain and the right hand side shows an isometric view of iso-contours of oil volume fraction. Dark Blue is for α=0.01, light blue for α=0.1, green for α=0.5 and red for α=1.

The oil mass in the rear chamber is plotted in Figure 6.13 as a function of time. The black plus sign on the graph represents the point in the simulation that the mesh was refined from 400,000 cells to 900,000 cells. As of 0.7 s of flow time the simulation has clearly reached a balance of oil into and out of the chamber, however it is a very small quantity of around 8x10^{-4} kg (0.02 litres). From the experimental work, a conservative visual estimate of the oil mass in the rear chamber, informed by a limited film thickness measurement of 0.35 mm, is approximately 0.003 kg. This is 3.75 times greater than the quantity of oil predicted by the VOF model. There are no indications that this oil will ever form a defined film that could be adequately modelled using VOF and the solution does not resemble the experimental results described in Section 6.1.1. It is therefore concluded that VOF is not a suitable multiphase model for this application.

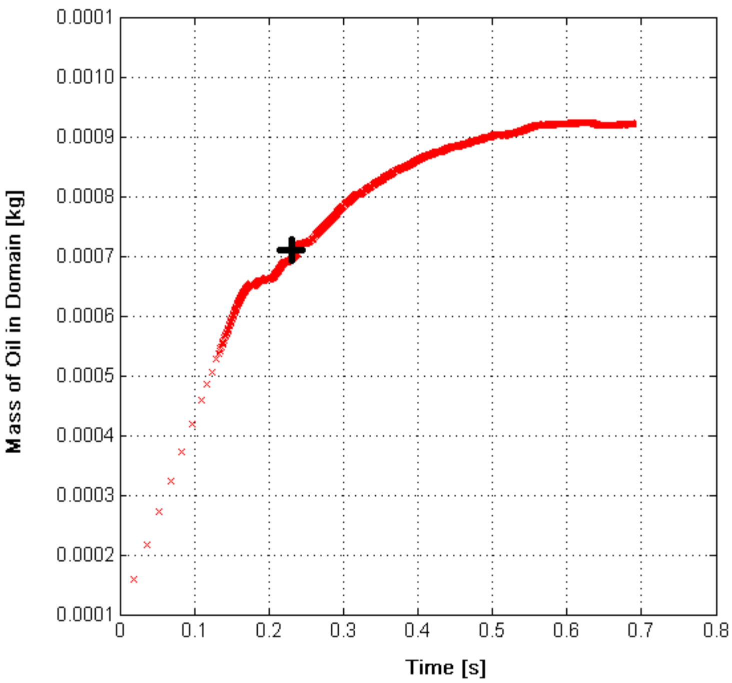

Figure 6.13: Graph showing the mass of oil, simulated by the VOF model, within the rear chamber as a function of time. The black plus sign on the graph represents the point in the simulation that the mesh was refined from 400,000 cells to 900,000 cells.

6.4.2 Eulerian Model

Whereas the VOF model is beneficial for modelling two fluids with a clear interface, the Eulerian model is capable of simulating multiple interpenetrating fluids. The number of fluids and their complexity may be limited by convergence behaviour and available memory. As the VOF model does not appear capable of capturing flow behaviour in the rear chamber, an Eulerian-Eulerian approach was investigated. The main difference between these two models is the Eulerian model solves momentum and continuity equations for each phase. However a single pressure term is shared by all phases. A full description of the Eulerian model and submodels used can be found in Chapter 3.

Eulerian Methodology

Using a Eulerian model approach, a droplet diameter must be set and in this study 80 microns is chosen; this value was chosen with reference to the work of Glahn et al. which has given a range of droplet diameters shed from a roller bearing [61] and from a rotating disk [62] at varying rotational speeds. These works showed the most common droplet diameter at 12,000 RPM was 80 microns. For the same reasons as explained with regard to the VOF model, an explicit time-stepping approach was employed to satisfy $CFL = 2$ and $C = 0.25$.

The same mesh as for the VOF simulation (containing 0.9 million cells) was employed.

Eulerian Results

The Eulerian model was initialised from the converged VOF simulation (point 0 in Figure 6.15). Contours of volume fraction are shown in Figure 6.14 and as can been seen by comparison with Figure 6.12, there is a significantly reduced quantity of low volume fraction mist when compare to the VOF model. This mist appears to coalesce and is pushed up to the top wall of the chamber. Here a higher volume fraction film forms. In addition, oil is not immediately broken up upon entering the chamber but instead strips off the back wall in ligaments. These then add to the growing film on the top wall.

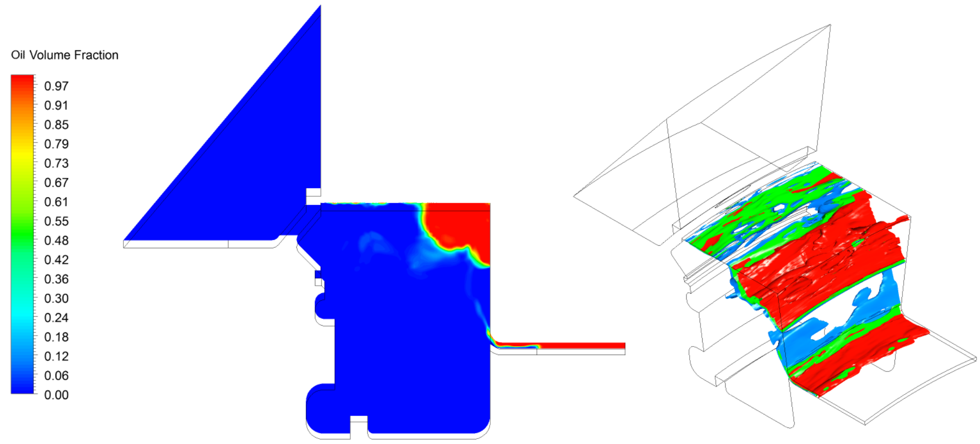

Figure 6.14: Image showing contours of oil volume fraction in the rear chamber for the Eulerian model. The left hand side shows contours through a plane through the centre of the domain and the right hand side shows an isometric view of iso-contours of oil volume fraction. Dark Blue is for α=0.01, light blue for α=0.1, green for α=0.5 and red for α=1

Figure 6.15 shows the mass of oil in the chamber as the calculation progresses. Point 0 marks where the model was switched from VOF to Eulerian and immediately the mass of oil starts to increase consistent with the oil behaviour described. This is a significant, order of magnitude increase from that calculated in the VOF model and more in line with the experimentally estimated oil mass. It is important to note that as of the end of the simulation (point 5 in Figure 6.15) a mass balance has not been achieved and there are indications that continuing increases in oil residence volume may become unphysical. This will be discussed in detail in the following section.

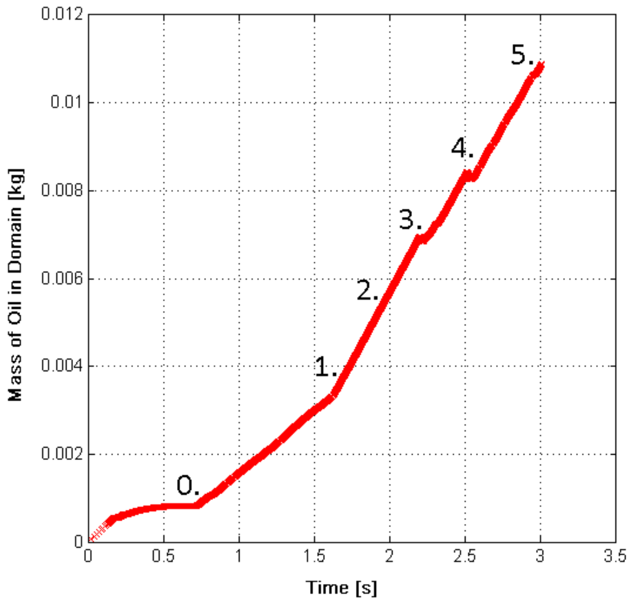

Figure 6.15: Graph showing the mass of oil, simulated by the Eulerian model, within the rear chamber as a function of time. Point 0 refers to the beginning of the Eulerian model. The other points 1-5 refer to the stages illustrated in Figure 6.17.

From comparison of the Eulerian and VOF approaches it is concluded that the Eulerian model is more appropriate for these bearing chamber flows. It is much better at modelling interpenetrating fluid phases as it solves continuity and momentum equations for each phase and it seems that the gaseous and liquid phases interpenetrate and mix more than was initially anticipated.

Figure 6.16 illustrates oil flow behaviour in the chamber at around 2 seconds into the simulation (point 2 in Figure 6.15). As oil leaves the bearing simulator inlet there are no longer regions of volume fraction $\alpha = 1$ and the oil phase can instead be regarded as a lower volume fraction dispersed mixture. This oil travels up to the top wall where it is pushed towards the back of the chamber by the air flow from the gear. A film develops on the rear section of the top wall and is essentially trapped here, as shown in Figure 6.16. In this figure the jet from the back of the gear can clearly be seen to split on the top surface. This creates a vortex cell in front of the outlet hole and also pushes the oil film towards the rear of the chamber.

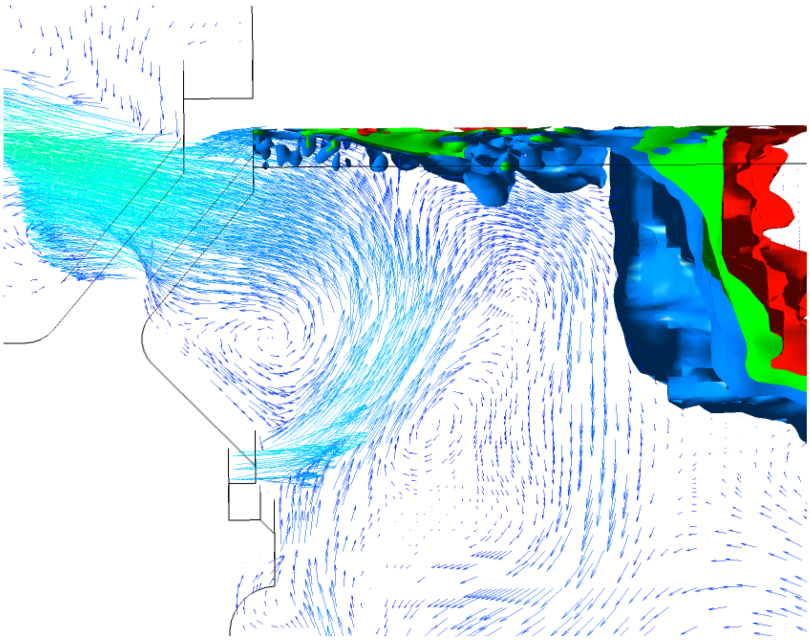

Figure 6.16: A close up view of the rear chamber outlet showing the impact of the gear jet on the oil film in this region at 2 seconds into the simulation (point 2 in Figure 6.15). Volume fraction is displayed as light blue for α=0.1, green for α=0.5 and red for α=1. A non uniform film height along the top wall is clearly identifiable.

The CFD calculation was continued up to 3 seconds and as is evident from Figure 6.15 it is not possible to tell when mass balance may be achieved. Figure 6.17 shows the growth of oil in the chamber from 1.65 s to 2.9 s. There are 5 snapshot images and these are also indicated as points 1-5 on Figure 6.15. The progression clearly shows a non uniform growth in film height and far in excess of the 0.35 mm film thickness measured in the experimental work. Driven by the gear jet, oil is unable to exit the chamber due to the vortex by the shroud exit hole and as result is forced to build in the rest of the chamber. Small amounts of oil are stripped from the film by the jet however the majority is contained within the chamber in the corner region. Whereas the oil flow fields at 1.65 seconds and 1.88 seconds look plausible, those at subsequent snapshots are increasingly less so. With such a large volume of oil it seems highly likely that gravity would play a significant role causing the oil to flow through the lower shroud exit slots.

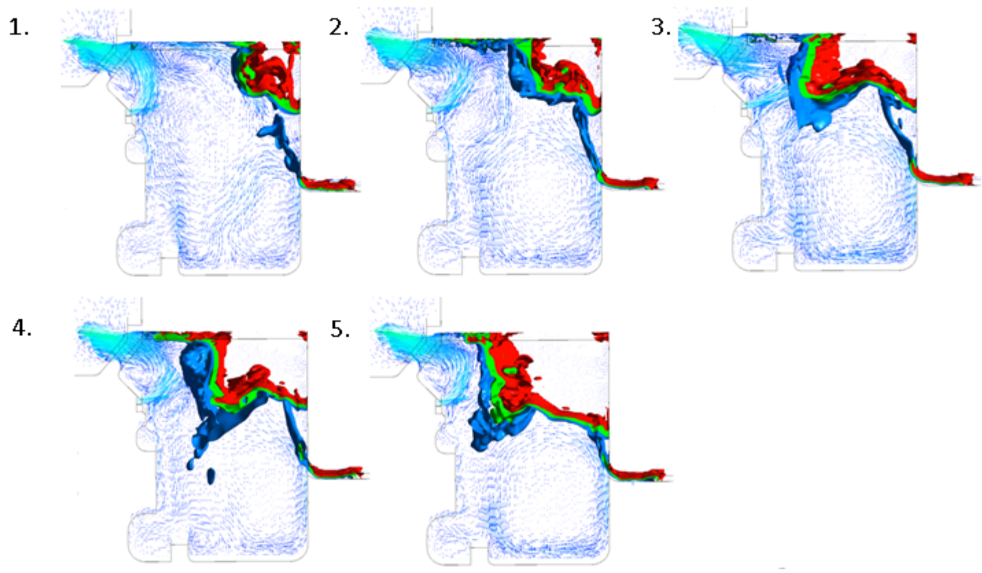

Figure 6.17: Images showing the progression of oil build up within the rear chamber over time. Volume fraction is displayed as light blue for α=0.1, green for α=0.5 and red for α=1. The mass of oil in the chamber for each stage can be seen in Figure 6.15

Looking again at the velocity profiles through the rear chamber, when the oil phase is added to the model, the core velocities in the rear chamber drop significantly and wall shear is no longer as highly dominant. The velocity profile from the Eulerian simulation is shown in Figure 6.18 and is taken at 3 seconds into the simulation at point 5 in Figure 6.15. It is clear that shear acting on wall films is much reduced in the two-phase case. Considering the increased weight of oil, as the film develops body forces become increasingly important and it no longer becomes acceptable to neglect gravity.

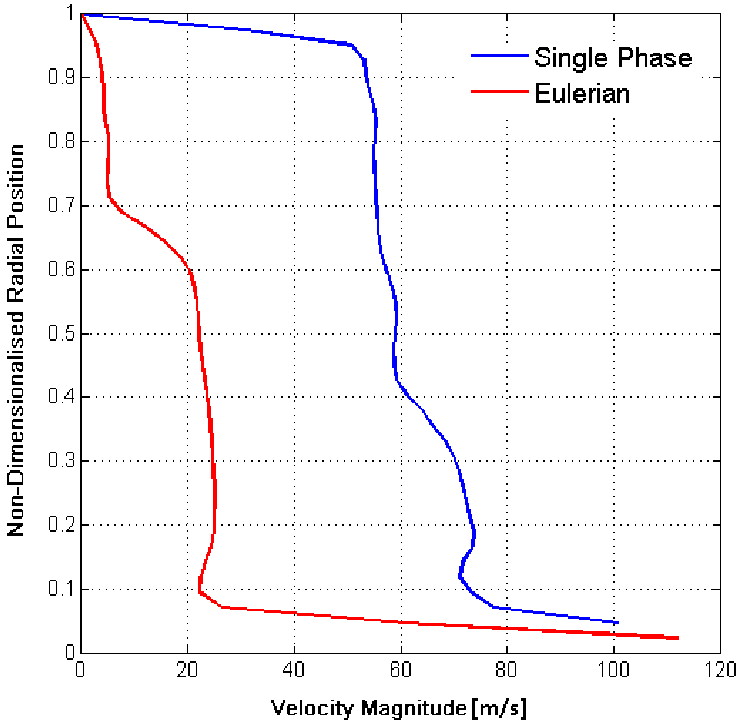

Figure 6.18: Graph showing the azimuthal velocity profile across the rear chamber for both single phase and Eulerian multiphase models. Data is taken from position 3 (see Figure 6.7).

Though gravitational effects were evident from the experimental work, the extent of its influence is greater than anticipated at high oil loads. As such it is not possible to get a representative distribution of oil without modelling the entire 360° chamber. It is therefore concluded that although useful information can be obtained from a sector model, gravity is likely a significant influence under some conditions and in such cases a full 360° model would be required. For these reasons the Eulerian model was concluded at 3 seconds of flow time.

It is important to consider that the present model ran for approximately 2 months on 32 Intel Sandybridge E5-2670 2.6GHz processors to produce 3 s of flow time. A 360° model would have a cell count of approximately 20 times larger than this model and would thus incur a substantial computational expense - a 40 month run time on the same computational resources.

6.5 Rear Chamber Modelling Conclusions

There have been several key findings highlighted by this work and these are:

1. The Eulerian model is a more suitable multiphase tool than VOF for this configuration due to the interpenetrating nature of the oil phase. The Eulerian model most closely matches the behaviour seen in the experimental work.
2. A higher mesh density is required for the 2-phase modelling work of this kind compared to that required for a single phase model full mesh independence for the two phase work is yet to be conducted.
3. Explicit time-stepping is necessary to achieve convergence.
4. The air jet from the gear shroud dominates the secondary flow behaviour in the rear chamber.
5. Secondary flow in the rear chamber acts to oppose oil from the annular inlet (simulated bearing).
6. Oil from the bearing forms a thicker ring towards the back of the rear chamber.
7. On the basis of the CFD data obtained there are several indications that gravity has a larger effect then initially expected and so the solution is unlikely to be axisymmetric. This is supported by recently obtained experimental data. It is recommended that future work on this and similar geometries be conducted on a full 360° model, though this model incurs a substantial computational expense.

The work in this chapter has been published in the Proceedings of the ASME Turbo Expo 2014: Turbine Technical Conference and Exposition [12].

Chapter 7

Rear Chamber Parametric Study

7.1 Introduction

Across many different engine architectures the IGB rear chamber does not have a standardised design and takes several different sizes and features.

Is there an optimum design for an IGB rear chamber? This chapter looks at several geometric features that are common in the rear chamber and suggests improvements based on the work in Chapter 6. The impact of these features on several single phase flow and oil flow characteristics is then assessed. The present study aims to give a quantitative analysis of which features are best to aid scavenge from the rear chamber as well as their impact on overall system performance.

7.2 CFD Methodology

The transient, Eulerian CFD methodology outlined in Chapter 6 will be used for each of the models in this chapter. Chapter 6 has highlighted the need for a full 360° model to fully understand the non-asymmetric, gravity influenced oil flow in the rear chamber. However it is possible to use the sector model to gauge relative improvements across several parameters.

In Chapter 5 a key conclusion was that for any significant change in back chamber geometry, the boundary condition used at the gear shroud restriction would have to be recalibrated from a combined gear and rear chamber model (as in Chapter 4). However, the purpose of this chapter is not to calculate an engine representative solution but to assess the impact of discrete geometry changes. For example, an exact torque calculation for the system is not required but a relative change in torque after a parameter is changed can be used to indicate if that specific parameter change resulted in an improved system performance.

As a result of this the gear shroud restriction boundary condition will be kept constant across all the models simulated in this chapter.

Each of the models described in this chapter operate at a shaft speed of 10,000 RPM.

7.3 Single Phase Analysis

A series of changes from the baseline case described in Chapter 6 will be made over the course of four models. These will be as follows:

A. Relocated shroud outlet hole

B. Reduced chamber dimensions radial extent and depth

C. Modified back wall including sloped section

D. Reduced area shroud outlet hole

These features can be seen diagrammatically in Figure 7.1. Each of these models will be compared to the previous model in the series and benchmarked against the original baseline case.

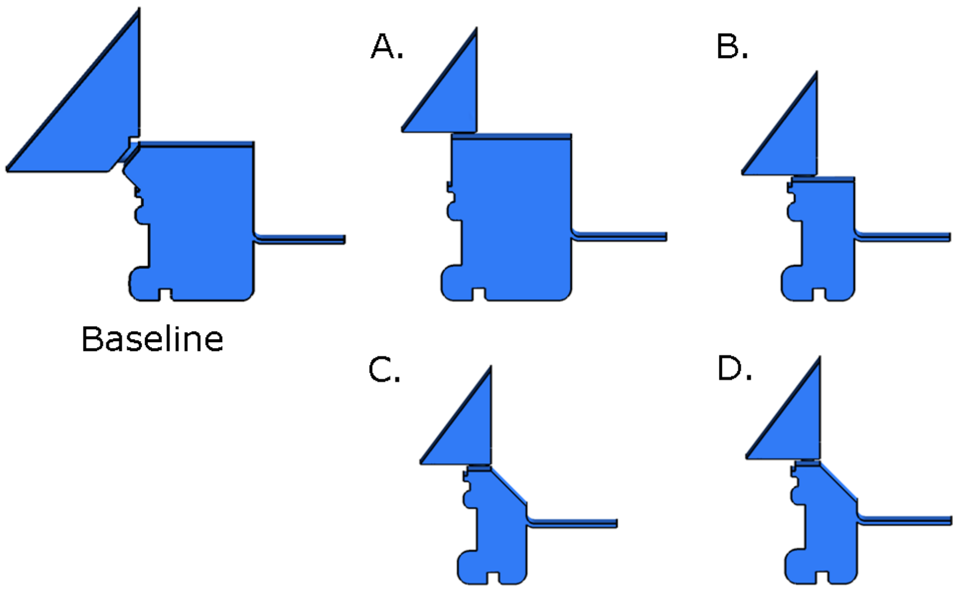

Figure 7.1: Parametric variations for the rear chamber. Baseline case, A) relocated shroud hole, B) reduced chamber dimensions, C) slanted back wall section and D) reduced area shroud outlet hole.

7.3.1 Chamber Vortices

This section investigates the changes in velocity vectors and vortices which occur as a result of the changing chamber geometries. Figure 7.2 shows an overview of the vectors in all five models, the four parametric variants and the baseline study.

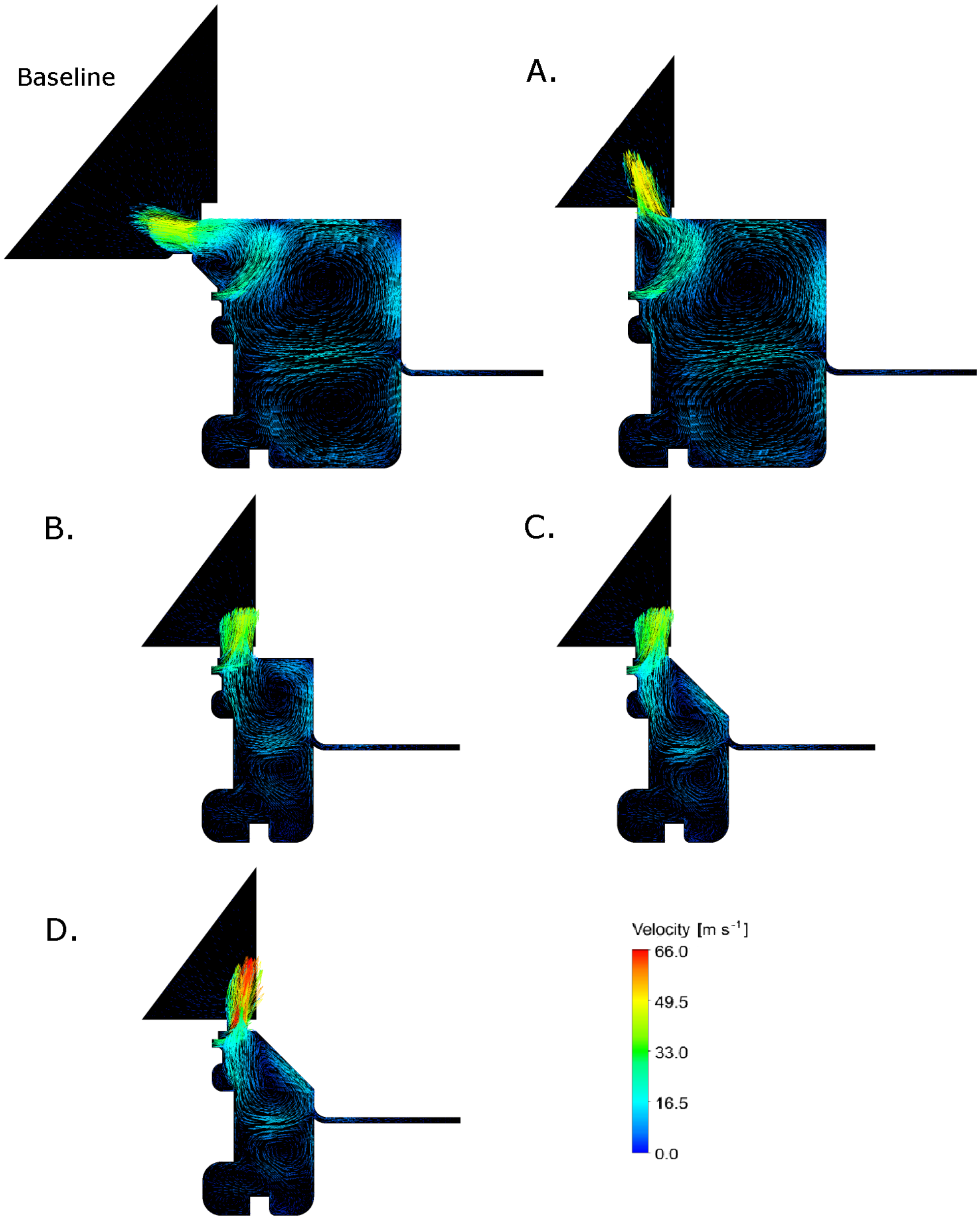

Figure 7.2: Time averaged, velocity magnitude vectors in the rear chamber for all models. Baseline case, A) relocated shroud hole, B) reduced chamber dimensions, C) additional slanted back wall feature and D) resized shroud outlet hole.

Figure 7.3 gives a closer look at the baseline case and defines the key vortex formations. A key feature of all the rear chamber flows is a large central, clockwise rotating vortex driven by the gear jet. This is designated as the primary vortex. Paired with this, and located radially inward towards the shaft, is the counter-clockwise rotating secondary vortex. The interface between these two vortices occurs at the point the oil feed inlet attaches to the rear chamber, the region from which oil is introduced to the system.

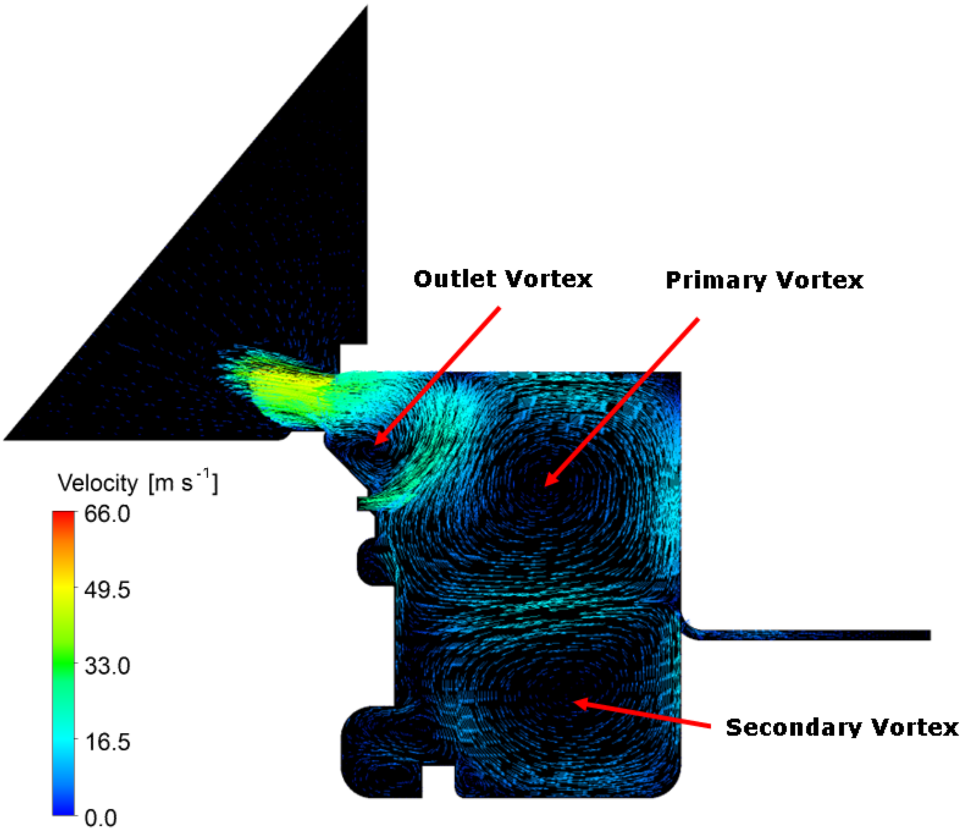

Figure 7.3: In plane, time averaged velocity vectors for the Baseline chamber model.

Outside these large structures there are several smaller, largely inconsequential vortices which form around the back detail of the gear. Of more significant note however is a counter-clockwise rotating vortex located at the shroud outlet which is separated from the rest of the chamber flows by the gear jet. Chapter 6 has shown that this vortex, along with the gear jet, impedes oil scavenge and can trap oil in the back section of the chamber.

The following geometric changes, based on realistic and implementable engine parameters, are designed to simplify the rear chamber structures and maximise the oil scavenge from the rear chamber.

Model A: Relocated Shroud Outlet Hole

The first change, case A, is to move the shroud outlet hole 90° from the back of the shroud to the top wall. The rationale for this is to minimise the impact of the outlet vortex and provide a more direct route for the oil to escape the chamber (see Figure 7.4).

Figure 7.2 shows very little variation in the main body of the chamber with both primary and secondary vortices largely unaffected by the change in the shroud hole. Time averaged velocity magnitudes reflect this with a minor increase of only 3.5%, 46.2 m/s in case A compared to 44.6 m/s in the baseline case.

One benefit, shown in Figure 7.4 is the movement of the hole away from the shroud outlet vortex. This now allows the oil path to bypass this impeding feature completely.

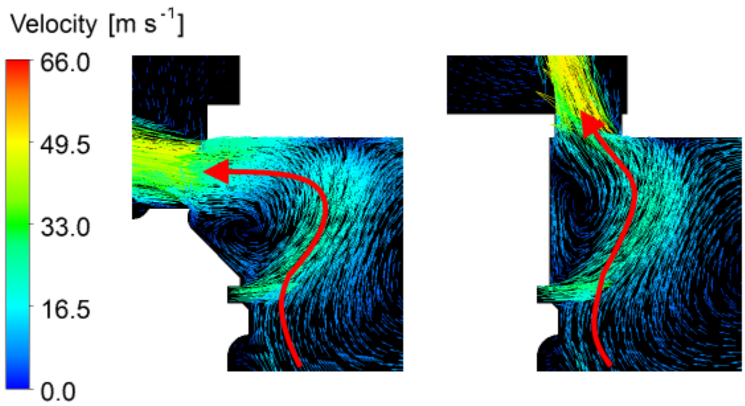

Figure 7.4: Time averaged velocity vector comparison of the Baseline model (left) and model A (right) with relocated shroud outlet hole. Oil path for both models is overlaid in red.

Model B: Reduced Chamber Dimensions

The second change, and most significant concerning the chamber flow formations, is the reduction in the chamber's depth and radial height. In a comparison between case A and B (Figure 7.5) the primary vortex has moved radially inward and the secondary vortex is now substantially more compact and has moved away from the shaft. Due to the proximity of the shroud outlet to the gear restriction, this configuration removes the outlet vortex completely and greatly minimises the oil path from the oil feed inlet to shroud outlet.

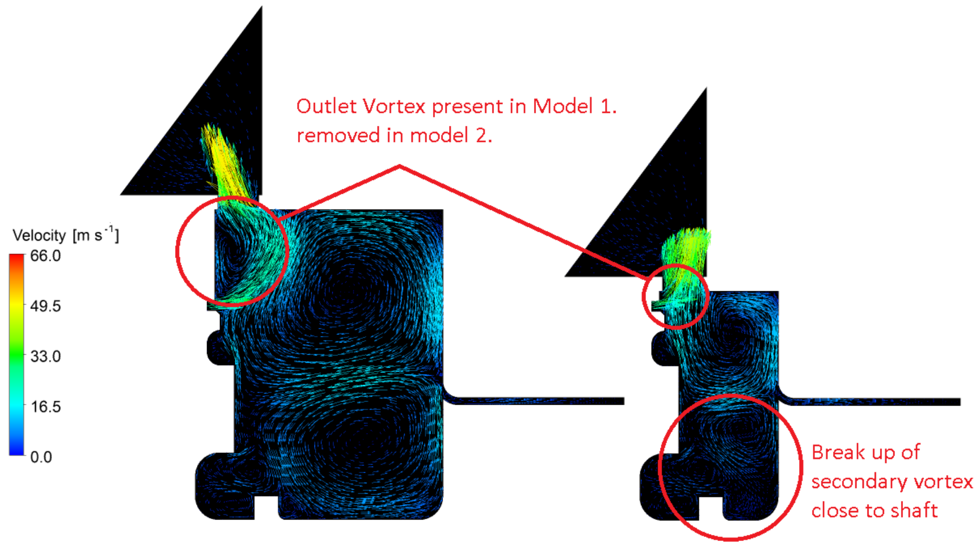

Figure 7.5: Time averaged velocity vector comparison of models A (left) and B (right) with reduced chamber dimensions. Key differences in vortex structure are highlighted in red.

As a consequence of the reduced dimensions the chamber has 63 % less volume available for the oil to fill and as a result will reduce oil residence time. The decreased volume also increases the proximity of the fluid to the rotating elements and as a result the time averaged circumferential velocity in the rear chamber rises by 18%, up to 54.5 m/s from 46 m/s in case A. The velocity range and maximum velocity in the chamber remains largely unchanged, maximum velocity increasing by 2%.

Model C: Sloped Back Wall Section

The modification to include a sloped back wall to case C is the final change to minimise available chamber volume, offering a further 10% reduction. This feature completely cuts off the ‘oil storage zone’ identified in Chapter 6 and again is designed to minimise oil storage volume.

The effect of this feature on the chamber flow structure is shown in Figure 7.6. In this case, the core of the primary vortex moves further radially inwards and the shape matches the profile of the sloped wall. This feature has a modest 6.5% increase on the chamber velocities, notably having a 27.4% increase on the maximum azimuthal velocity component which increases from 96.6 m/s to 123.1 m/s.

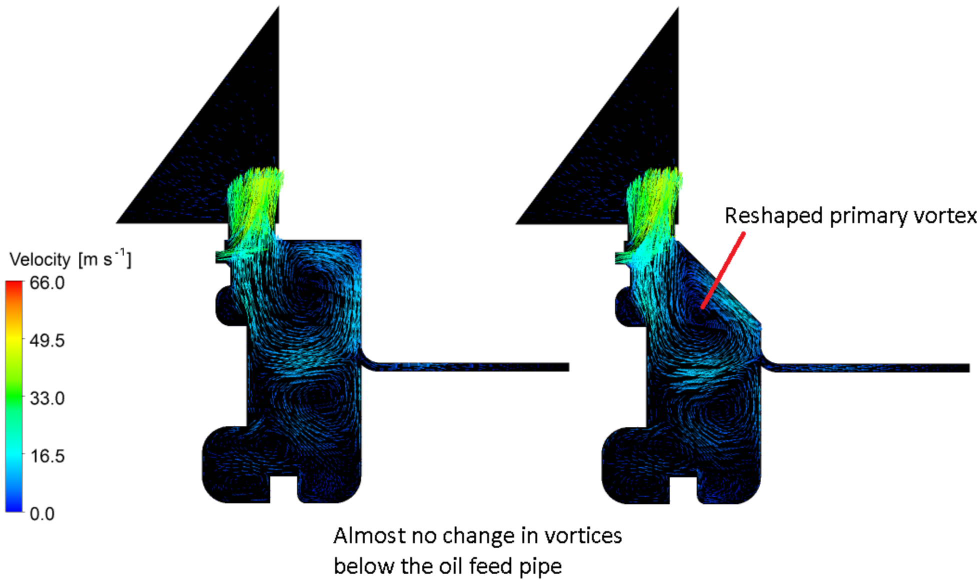

Figure 7.6: Time averaged velocity vector comparison of models B (left) and C (right) with additional sloped back wall feature.

Model D: Reduced Area Shroud Outlet Hole

The final parameter change is to decrease the area of the outlet hole in case D by approximately 33%. This change is approximately representative of actual engine modifications and also results in an increase in hole aspect ratio. Due to conservation of mass the reduced area will necessitate an increased jet velocity exiting the shroud hole and the impact of this on the chamber flow structures can then be assessed.

The effect of the reduction in shroud outlet hole area on the outlet jet will be discussed in Section 7.3.2. The chamber vectors however are largely identical to those in case C as can be seen in Figure 7.7. Both velocity magnitude and the dominant circumferential velocity component vary by only 0.2% and 0.9% respectively and the key vortex formations are all unchanged. This implies that variations in the outlet have only superficial effects on the rear chamber, though this is likely because, in this configuration, the inlet jet from the gear and the outlet are now in close proximity so the main flow effectively bypasses the chamber completely.

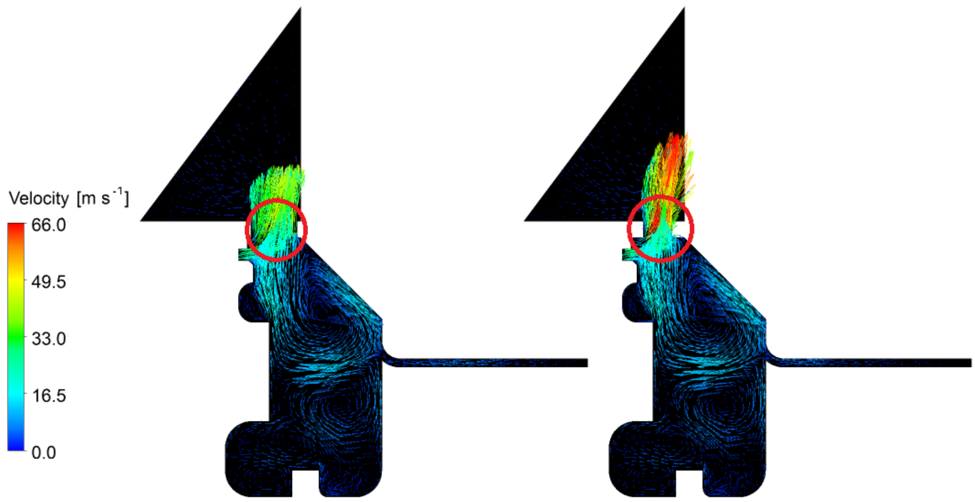

Figure 7.7: Time averaged velocity vector comparison of models C (left) and D (right) with resized shroud outlet hole.

The relative insensitivity of the chamber flows to the outlet affords some leeway to the aeroengine designer. However this extends only so far as significant geometry changes on the outlet structure do affect the rest of the chamber, for example making the chamber completely open backed as seen in Chapter 5.

7.3.2 Jet Characterisation

Two significant features in this study involve changing the location (case A) and size (case D) of the shroud outlet hole. This outlet vents as a jet into the main IGB chamber so understanding the implications of modifying this feature is important when considering the system as a whole.

Figure 7.8 shows top down and front views of the time averaged velocity magnitude vectors at the shroud outlet for each case. It is quickly apparent that modifying the location of the shroud outlet hole has a significant effect on the jet vectors, moving from predominantly axial and circumferential components in the baseline case to predominantly radial and circumferential in the others. The magnitudes of these components are also affected with a 17.3% increase in circumferential velocity, 14.7 m/s in the baseline as compared to 17.7 m/s in case A. It is worth noting at this point that circumferential velocities are greatly reduced from those in the rear chamber (approximately 46 m/s) due to the shroud hole thickness.

In addition to the 90° shift in velocity components, the magnitude of these components also increase when the outlet is moved to the top wall. Radial velocity in case B is 12.7% higher than the axial velocity in the baseline case, the jet velocity magnitude is 18.7% greater in total. These increased velocities are due to simplifying the structures in the rear chamber allowing less opportunity for the gear jet to lose energy before the flow exits the chamber.

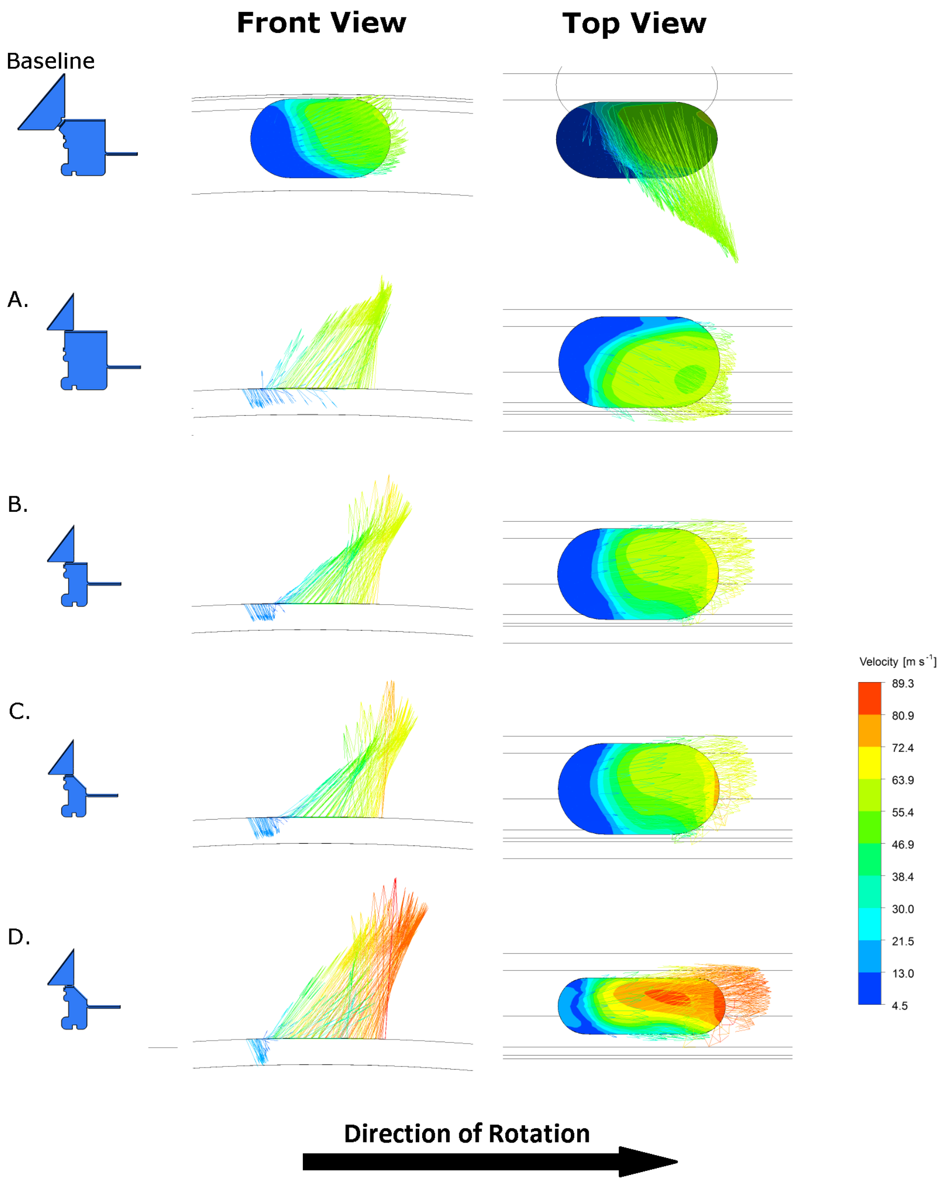

Figure 7.8: Front and top down views of the shroud outlet hole velocity vectors and in plane velocity contours for all five models.

Though there are no further changes to the outlet jet angle (which appears likely to be defined by the shroud hole thickness), further modifications to the rear chamber do vary the jet's shape. For cases A, B and C which share a common outlet hole size and location on the top wall, velocity magnitude and mass flow rate are unchanged in keeping with conservation of mass. However the range of velocities at the outlet do change. Reducing the chamber size (cases B and C) results in a stronger jet core, biased to the downstream side of the outlet. This is paired with a stronger recirculation at the upstream side of the hole which maintains conservation of mass. Maximum velocity in case A is 64 m/s and increases to 73.6 m/s in case B as the chamber dimensions are reduced, an increase of 15%. As the chamber volume is further reduced with the addition of the slanted back wall, the maximum velocity in case C further increases by 5.2%.

The final change in case D is the reduction in outlet hole area. In order for mass to be conserved the reduction in area (32.1%) must be matched by a corresponding increase in velocity and this is observed to be 48.7%, 29.3 m/s in case C up to 43.5 m/s in case D. The maximum velocity in this case increases by 15.5%, 77.4 m/s up to 89.4 m/s.

How these variations affect the flows in the main IGB chamber is currently unknown and is a promising area of further research. It can however be theorised that increased circumferential velocities in the main chamber would reduce gear torque, as air drawn into the gear shroud inlet from the main chamber would require less energy to accelerate it to maximum gear speeds, as evidenced in Chapter 5. The greatest effect on WPL comes from the gear's interaction with oil, both droplets and mist, and so how this exits the rear chamber and its motion around the main chamber is of significant interest.

7.3.3 Gear Torque

A direct benefit to engine efficiency is to reduce the gear windage losses caused by the wasteful energy transfer from the gear to the surrounding air. Webb's work [24] was primarily aimed at reducing this windage loss. Though the models here only include a small section of the rotating elements present in an IGB, a qualitative estimation of the effects of each parameter on the windage loss can be made to inform IGB design.

The equation for torque on the rotating elements in the rear chamber is given as

$$F_T.r = F_v.r + F_p.r \tag{7.1}$$

Where F_T is the total force acting on the element, F_v is the viscous force, F_p is the pressure force and r is the radial distance of the element from the axis of rotation.

In this application, the pressure forces are negligible in size when compared to the viscous forces and can be removed from the equation. The equation for the viscous force and fluid shear stress are as follows

$$F_v = \tau.A \tag{7.2}$$

$$\tau = \mu.\frac{\partial u}{\partial y} \tag{7.3}$$

where A is the surface area, μ is the dynamic viscosity of the fluid, δu is the relative velocity between the fluid and moving boundary and δy is the distance of the cell centroid from the boundary. ∂u can therefore be written as

$$\partial u = u_{fluid} - u_{wall} \tag{7.4}$$

Combining Equations 7.2 and 7.3 with Equation 7.1 gives the following definition of windage loss

$$T = \mu . \frac{u_{fluid} - u_{wall}}{\delta y} . A . r \tag{7.5}$$

Torque values for all models are given in Table 7.1. As is evident from the table, the baseline case and case A have very similar torque levels, within 0.4%. This is consistent as the rotating surface geometry is identical in both models and the velocity vectors close to this region are largely unchanged.

However, Cases B, C and D all have a measured torque around 21% lower than Case A. Primarily this is due to the reduced area of the rotating surfaces, a result of reducing the depth of the chamber in case B. The surface area is reduced from 0.0029 m^2 to 0.0025 m^2 (around 14%) and this accounts for an 11.23% reduction in torque.

Table 7.1: Table showing the time averaged torque loss on the rotating chamber surfaces for all models. Percentage differences from the baseline case are also given for each model.

Model	**Windage Torque [Nm]**	**Percentage Difference from Baseline**
Baseline	0.1187	-
A	0.1183	-0.41%
B	0.0934	-21.33%
C	0.0927	-21.93%
D	0.0923	-22.29%

Additionally then, there must be one or more mechanisms which reduce gear torque to account for the remaining 10%. Referring to Equation 7.2, torque is directly proportional to both area and shear stress. The shear stresses on the rotating surfaces are plotted in Figure 7.9 for Cases A and B.

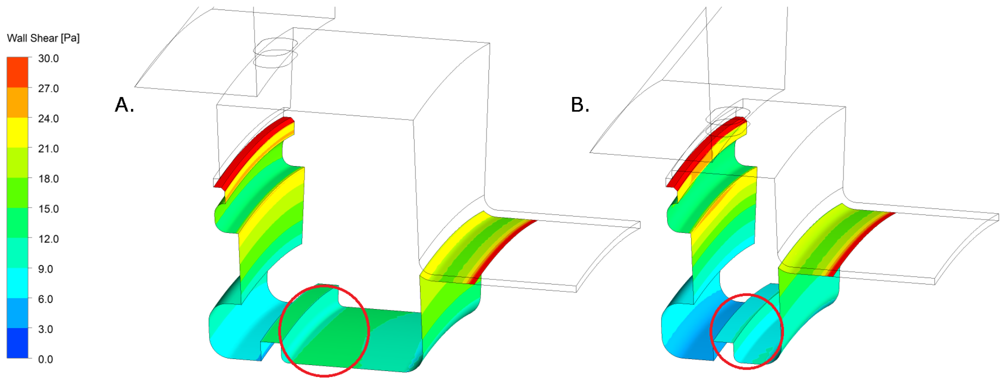

Figure 7.9: Image comparing the time averaged wall shear on the chamber's rotating surfaces between models A and B. The key region of shear comparison is circled in red.

Analysing the stresses on the rotating elements, which are split into the back of the gear and the rotating shaft, shear stress is seen to decrease by approximately 9% and 13.8% respectively. This is most easily identifiable on the rotating shaft and the key region of increased shear is circled in Figure 7.9. When calculated independently from the change in area between cases A and B, the decrease in shear between the two cases results in a torque drop of 10.6%. This therefore accounts for the remaining unknown reduction in gear torque.

The underlying mechanism which affects the amount of shear on the rotating surfaces is the fluid velocity close to the wall boundary. From Equation 7.3, the relative fluid-wall velocity ∂u is the only variable, μ is a fluid constant and ∂y is fixed for the geometry. As ∂u decreases so does the wall shear. The decrease in chamber volume results in an increase in circumferential fluid velocity (by around 20.2%) as described in Section 7.3.1. The shearing force between the

10,000 RPM rotating wall and the slower moving fluid is therefore minimised by the increase in fluid velocity resulting in a reduced gear torque.

Therefore the two practical means of reducing windage loss in the rear chamber are to minimise the rotating wall surface area and to increase the circumferential velocity of the fluid. In single phase, both of these can be improved by reducing the volume of the rear chamber.

7.3.4 Wall Shear

Another consideration in the rear chamber is the amount of wall shear on the top and back stationary surfaces. Chapter 6 showed that these surfaces are very oil laden when modelled in two phase and understanding the shear forces in these locations will inform oil behaviour, i.e. whether the oil will stick to the wall or pool at the bottom of the chamber.

In the baseline model, initially dominant shear forces were surpassed by relatively more dominant inertial forces as the volume of oil increased. Detrimental oil pooling can be avoided by reducing the resident volume of oil in the chamber and by increasing the shear on the outer walls. Section 7.3.3 describes the increase in chamber velocity and the resulting decrease in wall shear on the rotating walls. The opposite is true for the stationary walls where $u_{wall} = 0$ and the increase in fluid velocity u_{fluid} causes a rise in ∂u and resulting rise in wall shear. Table 7.2 show the calculated average wall shear on the top and back walls of the chamber.

As with the shear on the rotating surfaces, there is a significant (36.6%) increase in wall shear as the chamber dimensions are reduced in Case B. This is due to these surfaces moving to closer proximity to the highly rotating gear and high energy gear jet. This trend continues as the chamber dimensions are reduced further in Case C, the slanted wall moving even closer to the gear and presenting

Table 7.2: Table showing the average wall shear on the stationary back and top chamber walls for all models. Percentage differences from the baseline case is also given for each model.

Model	**Wall Shear [Pa]**	**Percentage Difference from Baseline**
Baseline	7.63	-
A	7.22	-5.33%
B	10.42	36.62%
C	13.74	80.16%
D	13.12	71.97%

a high 80.2% increase in shear when compared to the baseline case. Figure 7.10 shows the distribution of the wall shear over the chamber top and back walls for all cases.

Comparing cases A and B directly in Figure 7.11 shows a marked increase in shear on the top wall in line with the shroud exit hole. In case B this region is immediately adjacent to the incoming air from the gear and is the main impact zone of the jet. The circumferential component of the fluid is evident by the higher wall shear on the upstream edge of the shroud outlet. There is a band of very low wall shear at the back of the top wall, which in the baseline case was a region where oil became trapped in the chamber. Removing or reducing this region is a priority to improve oil scavenge behaviour.

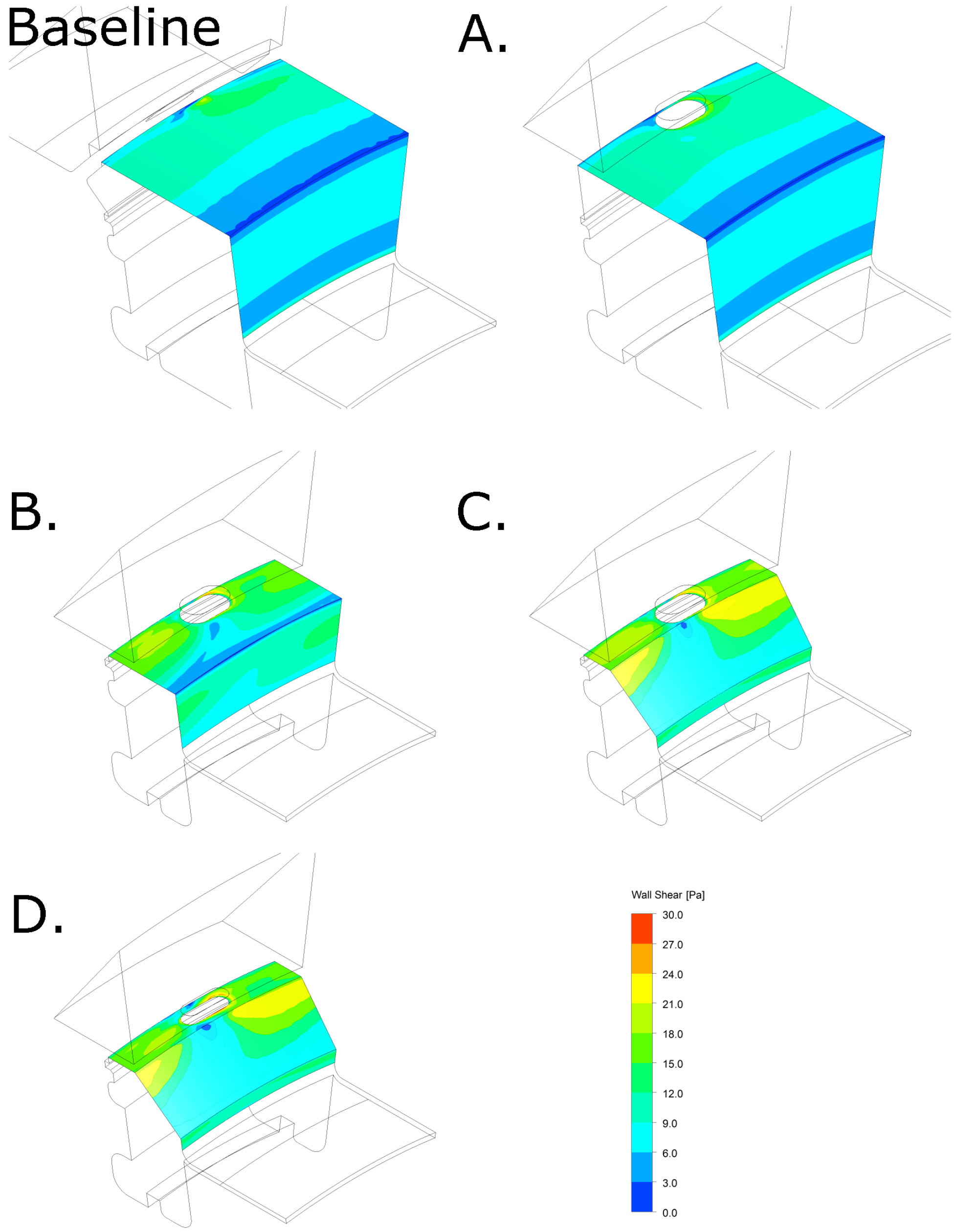

Figure 7.10: Comparison of the time averaged wall shear on the stationary top and back chamber walls for all models.

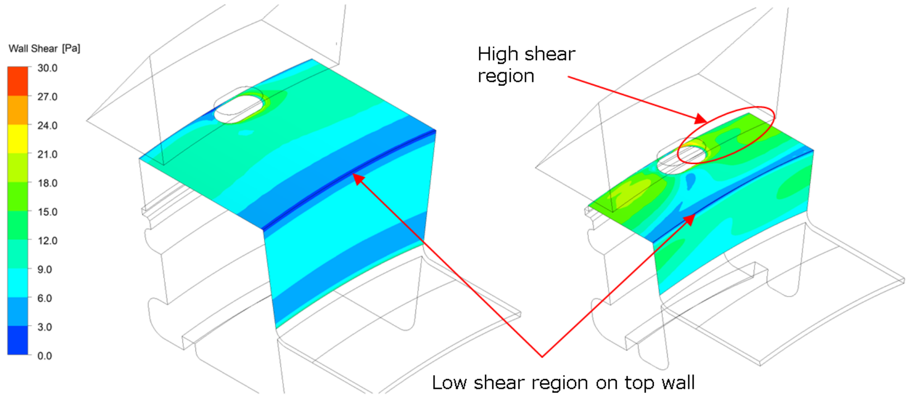

Figure 7.11: Figure comparing the time averaged wall shear on chamber top and back walls for models A (left) and B (right). Key regions of wall shear comparison are highlighted in red.

Figure 7.12 shows the same comparison, this time between Cases B and C. In this case the sloped wall is extremely close to the gear jet and extends the region of high wall shear, circled in red. Additionally, there is no longer any region of very low shear on the top or back walls, having been cut off completely by the sloped wall feature. As a result this case presents the highest calculated average wall shear, nearly doubling that of the baseline case. This, combined with the reduced volume for oil to build up, is a promising indicator that this case will decrease the likelihood of oil pooling.

Benefiting from the same sloped back wall, Case D has much the same wall shear characteristics as case C and shares a high 72% increase in shear from the baseline case. The change in area of the outlet hole appearing to have no significant impact on the shear on the top and back walls.

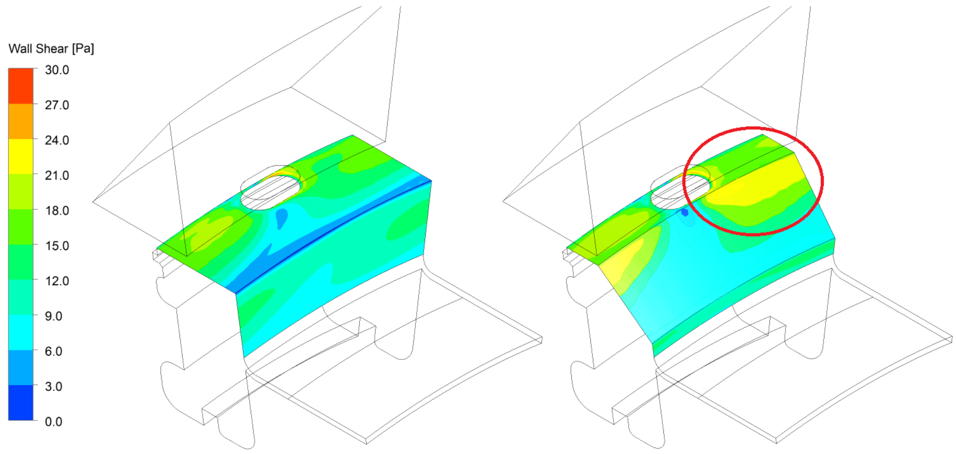

Figure 7.12: Figure comparing the time averaged wall shear on chamber top and back walls for models B (left) and C (right). The key region of wall shear comparison is circled in red.

7.4 Two Phase Analysis

From the single phase analysis described in Section 7.3, one model was taken forward to simulate in two phase. Case D was selected due to having the most beneficial torque, shear and oil path reductions.

The two phase simulation was calculated using the Eulerian methodology detailed in Chapter 6 and the transient single phase model was used to initialise the simulation. The model was run for 1.6 seconds using a variable time step of order of magnitude 10^{-4} s and run for 20 days on 32 Intel Sandybridge E5-2670 2.6GHz processors.

Figure 7.13 shows the oil residence volume over this time and contrasts it with that of the baseline case from Chapter 6. As can clearly be seen from the graph, the mass of oil in the domain reaches a steady value (of approximately 2.6x10^{-3} kg), something which was never achieved in the original baseline case. The baseline continued to fill with oil beyond 1.1x10^{-2} kg which is around 4 times the quantity in the present case.

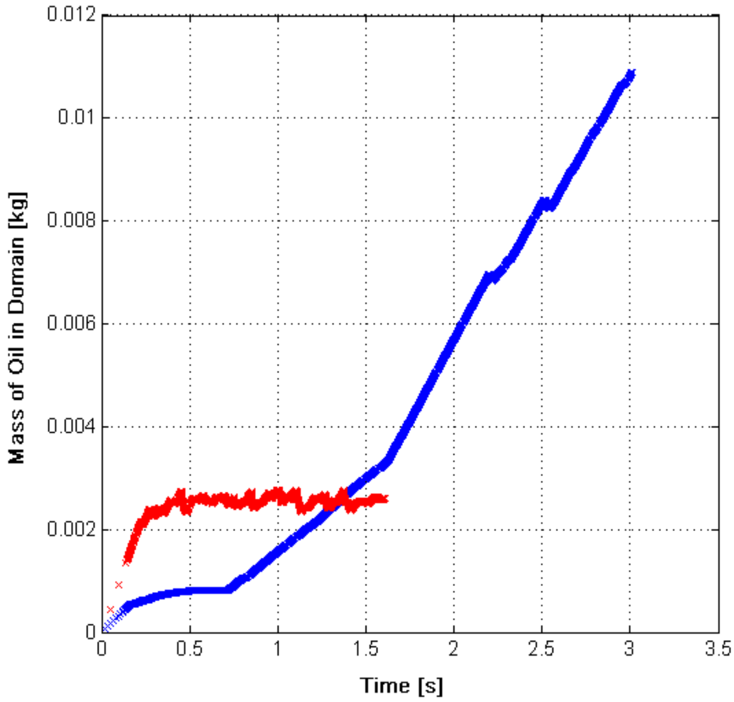

Figure 7.13: Graph tracking the mass of oil in the chamber domain with time. Model D is shown in red and the baseline case is shown in blue.

It is also evident from the oil mass graph (Figure 7.13) that fairly cyclic behaviour occurs with oil filling and then washing out of the chamber. The mechanism for this behaviour is outlined in Figure 7.14 with several distinct phases.

In phase 1 the flow is fairly constant and begins to build up just above the oil feed inlet. It is important to note that the oil flows back down the sloped back wall towards the oil feed as indicated in the figure. This is due to the disrupted clockwise rotating primary vortex still driven by the jet form the back of the gear.

In phase 2 the oil continues to build to a head and becomes gradually more unstable from its interaction with the nearby primary vortex. Eventually this head reaches a critical mass and oil is ejected into the chamber in phase 3. This large flash of oil into the chamber corresponds to the maximum peak of oil mass.

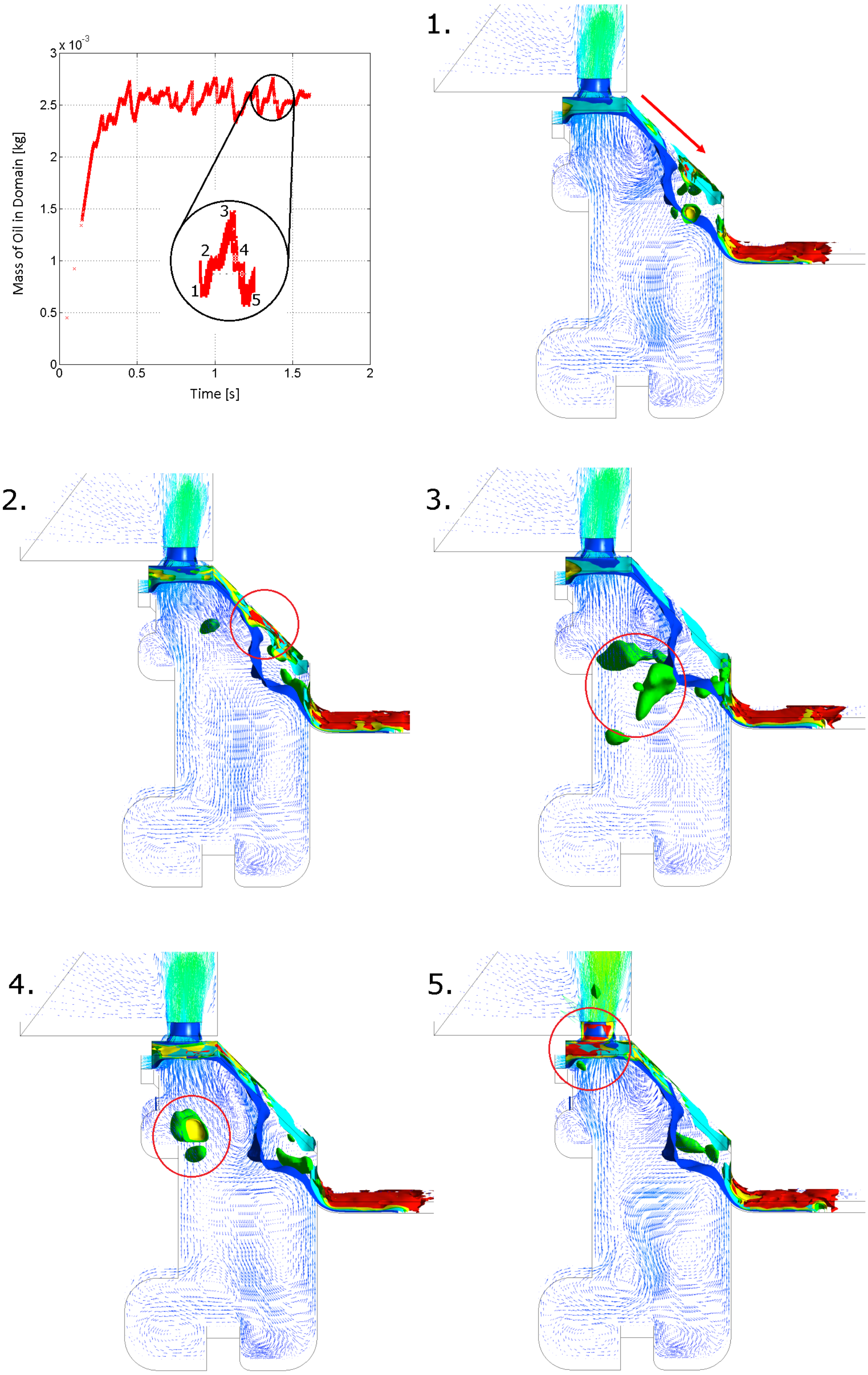

Figure 7.14: Series of images showing the vectors and oil volume fraction contours for the distinct phases of the rear chamber cyclic behaviour. Each images refers to a numbered point on the inset oil residence graph.

After this point the ejected oil is caught up in the primary vortex and directed up towards the high speed gear jet in phase 4. In phase 5 it is primarily flushed from the chamber however where there is no outlet hole a significant quantity impacts on the chamber top wall, circled in red. From this location the oil is either ejected from a subsequent shroud outlet or, alternatively, is washed back down the sloped back wall to restart the cycle.

From a combination of increased shear on the top walls and cutting down the available volume for oil to gather and become trapped, chamber design D shows significant improvement on the original baseline design. In particular reducing the likelihood of detrimental oil pooling.

7.5 Parametric Study Conclusions

7.5.1 Single Phase Conclusions

Four different parametric variations of key rear chamber geometric features have been simulated in single phase. These variations have been compared and contrasted and their effects on the chamber vortex formations, velocity components, windage torque and wall shear have been assessed.

Model A: Relocated Shroud Outlet Hole

The shroud outlet hole was moved 90° from the front face of the shroud to the top wall of the chamber. This had a minor effect on the chamber velocities, increasing by around 3.51%. A major benefit of the move means the oil path out of the chamber no longer passes through the impeding outlet vortex.

Changing the outlet orientation changes flows in the outer chamber and makes radial velocity dominant over axial velocity. In addition circumferential velocity increases by around 17.3%.

Gear torque is largely unchanged form the baseline model as is the wall shear on the top and back stationary walls.

Model B: Reduced Chamber Dimensions

Reducing the chamber dimensions has several benefits which aid oil scavenge. Firstly the decrease in chamber volume by 62.5% reduces the space for the oil to build up and become trapped. Secondly it minimises the oil path from the oil feed to the shroud outlet.

In addition to this average velocity within the chamber increases by 20.2% to 55.5 m/s. Maximum velocities within the chamber remain largely unchanged however the maximum jet velocity at the outlet does increase by 15%.

Reducing the chamber dimensions has a significant impact on the gear torque reducing it by 21.3%. This is a result of cutting down the rotating shaft surface area and an increase in fluid velocity in the direction of shaft rotation which reduces shear.

There is also an increase in wall shear on the top and back walls due to moving in closer proximity to the rotating elements.

Model C: Additional Sloped Back Wall

Replacing the top and back walls with a sloped chamber wall again benefits scavenge by further reducing chamber volume by 10.1%. This feature also cuts off the problematic low wall shear 'oil storage zone' region from previous models.

Average chamber velocities in this model increase by a further 6.4% up to 59.1 m/s. In particular the maximum circumferential velocity component increase from 96.6 m/s to 123.1 m/s. The outlet jet velocity also increase by a further 5.2% from model B.

The sloped wall brings the chamber top and back walls even closer to the gear and extends the impact zone of the gear jet. This results in a significantly increased wall shear, 80.2% greater than presented in the baseline case.

Model D: Resized Shroud Outlet Hole

Reducing the outlet area by 33% results in increased velocities in the outlet jet from 29.3 m/s in case C to 43.5% in case D. An increase of 48.7%.

Reducing the outlet area has otherwise very little impact on the rear chamber flows, with average velocity magnitude and circumferential velocities varying by only 0.2% and 0.9% respectively throughout the chamber. However large variations in geometry, for example opening up the chamber completely, will dramatically change the system flows as demonstrated in Chapter 5.

7.5.2 Two Phase Conclusions

Following the single phase study, model D was advanced to two phase simulations and compared to the baseline case simulated in Chapter 6.

Notably this model achieved a steady state, which the original baseline case was not able to do. In addition the chamber only retained 2.6x10^{-3} kg of oil, four times less than that of the baseline model. As a consequence of the reduced oil load and increased shear, the sector model used in this chapter becomes a more valid approach.

A cyclic behaviour was observed. Oil is washed down the sloped back wall towards the oil feed and builds up at the base of the wall. Once a critical mass of oil is reached oil is ejected into the chamber. This ejected oil is carried up by the primary vortex and is either removed via the shroud outlet or impacts on the top wall. The oil is then either removed from a subsequent outlet hole or is washed back down the sloped wall to begin the cycle anew.

The significantly reduced quantity of oil, in addition to the increased shear on the outer stationary walls promises a reduction in the likelihood of oil pooling. Combined with 21% less gear torque, this marks the model D geometry as a great improvement on the baseline design. In particular the reduced chamber dimensions and the sloped back wall are recommended design features.

Chapter 8

Conclusions

This chapter ties together the conclusions made throughout the thesis and states the contribution to science of the research. Potential avenues for future work are suggested.

8.1 Attainment of Objectives

The aim of this project was to progress the development of computational modelling capability and strategy for a two phase simulation of an aeroengine IGB. The key objectives to achieve this aim were revised as the project progressed, largely as consequence of the work presented in Chapter 5. The objectives were as follows:

1. Progress CFD modelling capability for a full IGB bearing chamber through
   (a) The development and evaluation of a momentum source model to replace the geometric and flow complexity of the spiral bevel gear pair.

(b) Evaluation of the extent to which the IGB can be modelled as a series of linked sub-models.

(c) Evaluation of the effectiveness of conventional CFD multiphase modelling approaches for modelling the chamber behind the gear within an IGB.

2. Apply identified modelling approach for IGB gear back chamber to determine optimum from a range of proposed/existing designs.

Simplified Gear Representation Methodology

As part of the first objective a simplified momentum representation in single phase of a spiral bevel gear, was developed and is described in Chapter 4. This model replaces the complex gear tooth geometry with a simple cone and momentum source region. A $1/23^{rd}$ sector of the chamber was modelled using periodic boundaries. By calibrating the source terms defined in the region above the cone surface, the fluid flow through the gear-shroud sub region was matched to an existing validated modelling methodology. Bulk mass flow rates were matched to within 4% and mean velocities to within 3.4%. This approach is valid for a single phase flow provided good calibration data is available.

Extending development of the momentum source model, the approach was applied to create a representative model of the UTC gear windage test facility, again in single phase. This work, reported in Chapter 4, demonstrated the ability of the simplified model to be implemented in a large chamber geometrically similar to the one used on the UTC rig. In this instance bulk mass flow rates were calculated to within 5% and axial velocity to within 6%. The work relating to these two elements was published in the Proceedings of the XXI International Symposium on Air Breathing Engines, 2013 [10].

Also reported in Chapter 4 was the extension of the simplified gear representation to work with two phase flows using the DPM Lagrangian multiphase model. The results from the momentum source model were compared with data for a geometrically representative model (in this thesis designated the 'full tooth model'). The full tooth model was generated building on techniques developed in prior work but modelling was extended through the application of a film model in additional to discrete phase modelling. Data from the full tooth model added to understanding of two-phase behaviour under the shroud and the following conclusions can be drawn:

- Oil droplets injected at the inlet to the shroud representing oil flow from the external chamber tend to impact towards the lower part of the shroud near the inner diameter
- Oil droplets injected from a gear tooth flank, representing the into-mesh jet, tend to impact relatively evenly along the shroud
- Where a film model is applied, overall oil motion is seen to be towards the top of the shroud for droplets injected at the tooth top land location.

The film model work was limited in scope due to limited computational resources. To representatively model the film generation upwards of 500,000 particles are required and this is very memory intensive. As a result the simulation was only able to run for a finite length of time before memory requirements were exceeded. A limitation of the two-phase full tooth modelling work is therefore that the bulk droplet behaviour over time could not be determined. This remains a promising area of future study as computational resources become more cheaply and readily available.

Using the two phase data generated from the full tooth model simulations, comparisons were then made with the momentum source model. Droplets were released at the shroud inlet and from the side of the domain in a region comparable to release at the tooth flanks. Due to inherent limitations in removing the detailed gear tooth geometry the momentum source model is unable to model droplet impact and detailed droplet behaviour under the shroud. The following conclusions were made:

- The majority of droplets are caught in a fast fluid flow and, unhindered by the tooth geometry, do not impact the shroud as early as they should.
- The lack of tooth valleys prevents the droplets from exiting at the shroud restriction driving them instead to impact in the shroud gutter region.

Much of the work relating to multiphase modelling under the shroud was presented at ASME Turbo Expo 2013 [11].

Zonal Coupling Study

Following on from the development and evaluation of the momentum source model a key conclusion was that the momentum source model was not a viable route towards full two-phase modelling capability if details of oil behaviour under the shroud are required. Research was thus focused towards an approach that allowed full tooth modelling to be used without incurring an unacceptably high computation time. The idea of a linked zonal approach was postulated and investigated. This work is reported in Chapter 5. These studies included varying the amount of pre-swirl of the flow drawn into the gear and shroud subsystem to gauge the impact on performance as well as understanding the influence of the shroud outlet geometry.

The impact of pre-swirled flow on the gear performance can be related to fan theory. It was determined that an increase in swirl in the direction of gear rotation results in a decrease in both torque and mass flow which demonstrates spiral bevel gear behaviour is consistent with fan theory. For this geometry configuration and a swirl number of 1.42 there is a 7.6% reduction in torque and a 3.8% reduction in mass flow rate. An additional finding from this work was that the swirl exiting at both the shroud outlet hole and the shroud restriction appears insensitive to the swirl entering at the inlet. The variation in azimuthal velocity at these points is 0.5% and 1.2% respectively. It can therefore be concluded that, in single phase, the under shroud regions of an IGB can be decoupled from the main chamber and modelled in isolation.

The second part of these investigations compared the outlet geometries for the full tooth model. Four variations were studied with combinations of two shroud types and two outlet types, one with a completely open rear chamber and one with a restricted chamber. The results of this study showed variations in the axial and azimuthal velocities between the different shroud types (up to 18% azimuthal variation measured at the shroud restriction). There were significant differences when the outlet was modified, axial and radial velocities reduced by approximately 47% in the restricted case compared to the open case. Azimuthal velocity at the restriction was largely unaffected by the outlet condition. In a case where the shroud top wall extends into the chamber there is a clear damping of the radial velocities.

The conclusions drawn from these findings indicated that the flows throughout the gear-shroud system are affected by the rear chamber geometry and this was highlighted as an area of promising study. The rear chamber is also bounded by a large location bearing which represents the largest influx of oil into the system. This makes the region critical to understanding the two phase flows in the IGB.

The work on zonal coupling is awaiting publication in the Proceedings of the ASME Turbo Expo 2015: Turbine Technical Conference and Exposition [66].

Rear Chamber Investigation

Evaluation of a suitable two-phase modelling approach for the rear chamber is reported in Chapter 6. Single phase and two phase studies were conducted using the VOF and Eulerian models on a $1/23^{rd}$ sector model which is geometrically similar to the UTC gear windage facility. Due to computational expense a sector model represented the most practical method moving forward and limitations of the chosen approach are discussed in the chapter. This chapter also details the experimental work conducted on the UTC gear windage rig in parallel to the computational study, as results from this experimental work are discussed and used as qualitative evidence to support the computational model.

From the single phase work a mesh independence study was conducted and verified that a 400,000 cell mesh is sufficient (this mesh density was increase to 900,000 for the two phase work). Key flow behaviour was identified including the significance of the jet from the back of the gear in determining the chamber flows. This jet splits on the top wall and causes the flow to travel to and then down the back wall. A strong vortex is also formed next to the shroud outlet hole.

Extending the model to two phase demonstrated that the Eulerian model is superior to the VOF model in simulating rear chamber flows. Experimentally it is shown that oil gathers in a film towards the back of the chamber's top wall. The VOF model was unable to capture this physics largely due to the interpenetrating nature of the flow. The Eulerian model was much more suited to this kind of behaviour and was able to simulate a film on the top wall in the same location as the experimental work. It was determined that this behaviour was a result of the interaction between the gear jet and the annular oil inlet, something that was not apparent from the experimental work alone. An explicit time-stepping approach was required which in part contributed to a high computational expense.

It is important to note that due to the very long simulation time, a maximum quantity of oil in the chamber was not reached. As the oil volume increased it was predominantly contained in the chamber by the gear jet instead of being ejected from the shroud outlet hole. The film thickness grew substantially greater than the film thickness on the chamber top wall measured in the experimental work. Calculations to predict the shear forces in the chamber point to the exclusion of a gravitational term in the model as a likely cause of this error (the exclusion of which was a necessary requirement to implement a sector model). For high oil loads gravitational forces can no longer be neglected and influence the model substantially more than was initially anticipated. As a result the simulation was terminated before a mass balance could be achieved, serving no further academic use.

A key conclusion is that a Eulerian model remains a practical method for modelling rear chamber two phase behaviour however a sector model neglecting gravitational forces is only useful for modelling low oil load conditions. For high oil load conditions a full 360° with a gravitational term is recommended.

The work in Chapter 6 was presented at ASME Turbo Expo 2014 [12].

Rear Chamber Modelling Recommendations

Research conducted using the modelling techniques of Chapter 6 is presented in Chapter 7, where a study is undertaken to provide insight into the design of the rear chamber. A parametric study was created based on four key geometry features and designed to reduce both oil load and residence time. These features were:

- Shroud outlet hole location

- Chamber axial and radial dimensions
- Back wall geometry
- Shroud outlet hole size

Each model was run in single phase and one model was extended to two phase. The sector model was used for both single and two phase simulations which were optimised for a low oil load.

There are several benefits for each feature variation. Relocating the shroud outlet from the front chamber wall to the top wall simplifies the oil path which is favourable for reducing oil residence. In addition this change increased the chamber velocity magnitudes by around 3.5%.

Reducing the axial and radial dimensions decreased the chamber volume by 62.5%. The benefits of this are twofold. Firstly there is a reduced potential for oil storage, which reduces oil load. Secondly moving the walls closer to the rotating gear increases wall shear. The combination of the two reduces the dominance of gravitational forces and lowers the chance of oil pooling in the rear chamber.

Angling the back chamber wall provides a simplified oil path to the shroud outlet hole and further reducing the chamber volume. In addition it removes back corner of the chamber, the main location oil becomes trapped. This positively affects oil residence time and reduces oil loading.

Changing the size of the outlet hole has very little effect on the chamber flows. A reduction in size (by 33%) results in an increase in velocity magnitude (of approximately 48%) primarily due to conservation of mass, however due to the close proximity of the jet to the outlet hole the faster velocities here primarily bypass the rest of the chamber.

By applying all of these geometry features and employing a two phase Eulerian methodology the simulation was able to run significantly faster then the preliminary model described in Chapter 6 and reached a consistent mass balance. A cyclic behaviour is observed with the chamber filling and flushing out the oil once a critical level is reached. Each cycle repeats approximately once every 0.25 seconds. The total oil volume is reduced to 2.6x10^{-3} kg which is a 75% improvement compared to the baseline geometry.

Overall the work presented here has significantly extended modelling capability for an IGB. It has been shown that it should be possible to split the IGB into a series of zones linked by boundary conditions. The flow under the gear should be modelled using a geometrically representative approach with DPM and a film model. The rear chamber can be modelled using an Eulerian multiphase approach. The amount of swirl in the main chamber affects flow behaviour through the gear but flow from rear chamber to front chamber is largely independent of the swirl within the front chamber, within the ranges studied. In addition it has been shown that flow exiting the rear chamber is strongly dependent on the chamber geometry and that reduced volume, vertical exit and sloping rear wall all appear to be good features.

8.2 Future Work

This thesis has demonstrated the ability of a simplified gear representation in single phase. Continuing with this work there are several areas of promising future development.

In the present work, the momentum source model utilised a uniform source term in three dimensions to define the flow field. Adapting these terms to become a function of gear radius and rotational speed would allow the model to be used for a wider range of gear geometries and operating conditions and increase its value as a modelling tool.

The core mechanism in an IGB is a spiral bevel gear pair. Extending the gear representation to include a pinion gear and simulating the effect of the meshing teeth using source terms would create a base around which a fully integrated IGB model can be based. This method is substantially less computationally intensive than explicitly modelling the meshing teeth (for example in the work of Strasser [33]) and frees computational expense to model complex two phase flows. A requirement for this is the prior development of a detailed meshing gear computational methodology as well as further study to determine how well the momentum source model simulates the bulk oil transport under the shroud.

In conjunction with this, this thesis presented a methodology of modelling the gear rear chamber as a sector. With developments in computational resource it would be feasible to extend this to a full 360° model to fully assess the effect of gravity. Extending to a 360° model also allows the inclusion of non axisymmetric geometry such as sumps and more advanced shroud designs.

Finally combining these two methodologies would allow the gear representation to drive a two phase Eulerian simulation. This would provide a significant insight into the interaction between each component, allowing us to see in real time how parameter changes affect every part of the IGB system. Including heat transfer and droplet to film models would create a powerful design tool to understand and improve gear windage, HTO hotspots and overall engine performance.

8.3 Contribution to Science

The work presented in PhD thesis has made a contribution to science in several areas.

The key methodologies and conclusions from this thesis are as follows:

- It is possible to replace a computationally expensive explicitly modelled spiral bevel gear with a simple cone and momentum sources.
- In two phase a cone and momentum source model is unable to model local droplet physics.
- It is possible to decouple the gear and shroud from the rear and main chambers to model each in isolation using boundary conditions.
- The Eulerian multiphase model can be used to model the two phase flow in a IGB rear chamber.
- The rear chamber can be modelled with a sector geometry to reduce computational expense as long as there is a low oil load and shear forces dominate. For high oil loads a 360° model with a gravitational term is recommended.
- Improved rear chamber design can be achieved by reducing the total volume, simplifying the oil path and including features like a sloped back wall to remove possible regions oil may become trapped.

Several sections of this thesis have previously been published and presented to academic peers [10–12, 54, 66]. The work has also been disseminated to Rolls-Royce Plc to inform IGB design.

References

[1] ANSYS, *ANSYS FLUENT 13.0*. ANSYS Inc., Southpointe, 275 Technology Drive, Canonsburg, PA 15317.

[2] G. Johnson, B. Chandra, C. Foord, and K. Simmons, "Windage Power Losses from Spiral Bevel Gears with Varying Oil Flows and Shroud Configurations," *Proceedings of the ASME Turbo Expo 2008, Vol 4, Pts A and B*, pp. 1415–1421, 2008.

[3] ACARE, "www.acare4europe.com," July 2014.

[4] IATA, "Airline & Aircraft Operations." International Air Transport Association, 2012.

[5] A. A. Lord, *An experimental investigation of geometric and oil flow effects on gear windage and meshing losses*. PhD thesis, University of Wales, Swansea, 1998.

[6] P. H. Dawson, "High-speed gear windage," *GEC Review*, vol. 4, pp. 164–167, 1988.

[7] G. Johnson, K. Simmons, and C. Foord, "Experimental investigation into windage power loss from a shrouded spiral bevel gear," *Proceedings of the ASME Turbo Expo 2007, Vol 6, Pts A and B*, pp. 57–66, 2007.

[8] D. Winfree, "Reducing gear windage losses from high speed gears," *ASME Power transmission and gearing conference*, 2000.

[9] G. Johnson, "Experimental investigation into gear windage power loss - UTC Status Report Presentation April 2010," Tech. Rep. FF20, The University of Nottingham Rolls-Royce University Technology Centre in Gas Turbine Transmission Systems, 2010.

[10] A. Turner, H. P. Morvan, and K. Simmons, "Single phase modelling of an aeroengine spiral bevel gear using a cone and momentum-source approach," *Proceedings of the XXI International Symposium on Air Breathing Engines*, 2013.

[11] A. Turner, H. P. Morvan, and K. Simmons, "Two phase CFD modelling of a spiral bevel gear using particle injections and a wall film model," *Proceedings of the ASME Turbo Expo 2013: Power for Land, Sea and Air*, 2013.

[12] A. Turner, H. Morvan, and K. Simmons, "Two phase computational study of flow behaviour in a region within an aeroengine gearbox," *Proceedings of the ASME Turbo Expo 2014: Turbine Technical Conference and Exposition*, 2014.

[13] Rolls Royce, "SPAN (RR Intranet access only)." Rolls Royce plc.

[14] J. W. Chew and N. J. Hills, "Computational fluid dynamics and virtual aero-engine modelling," *Proceedings of the Institution of Mechanical Engineers Part C - Journal of Mechanical Engineering Science*, vol. 223, pp. 2821–2834, Dec 2009.

[15] S. Gorrell, "An air force research laboratory perspective on high-fidelity simulations," *Proceedings of the ASME Turbo Expo*, 2006.

[16] W. N. Dawes, "Technical challenges for a real virtual engine," *ASME Turbo Expo.*, 2007.

[17] J. W. Chew and N. J. Hills, "Computational fluid dynamics for turbomachinery internal air systems," *Philosophical Transactions of the Royal Society A - Mathematical Physical and Engineering Sciences*, vol. 365, pp. 2587–2611, Oct 15 2007.

[18] C. A. Long, A. B. Turner, G. Kais, K. M. Tham, and J. A. Verdicchio, "Measurement and CFD prediction of the flow within an HP compressor drive cone," *Journal of Turbomachinery-Transactions of the ASME*, vol. 125, pp. 165–172, Jan 2003.

[19] Z. X. Sun, J. W. Chew, and N. Fomison, "Numerical Simulation of Complex Air Flow in an Aeroengine Gear Box," *Proceedings of the ASME Turbo Expo 2009, Vol 3, Pts A and B*, pp. 1197–1206, 2009.

[20] R. F. Handschuh, "Efficiency of high-speed helical gear trains," *59th Annual Forum and Technology Display sponsored by the American Helicopter Society, Phoenix, Arizona, May 6-8*, 2003.

[21] C. N. Eastwick and G. Johnson, "Gear windage: A review," *Journal of Mechanical Design*, vol. 130, Mar 2008.

[22] P. H. Dawson, "Windage Loss in Larger High-Speed Gears," *Proceedings of the Institution of Mechanical Engineers Part A - Journal of Power and Energy*, vol. 198, no. 1, pp. 51–59, 1984.

[23] G. Johnson and K. Simmons, "Effect of Chamber Density on the Windage Power Loss of a High-Speed Spiral Bevel Gear Set," in *Performance Enhancing Technologies for Transmissions*, (AugustaWestland, Yeovil), Institute of Mechanical Engineers, Oct 2009.

[24] T. Webb, *Power losses in spiral bevel gears.* Phd thesis, University of Nottingham, 2010.

[25] H. Morvan, "Shroud Design Guidelines," Tech. Rep. FSG 90540, Rolls Royce (FSG) and The University of Nottingham, 2010.

[26] K. Simmons, G. Johnson, and N. Wiedemann, "Effect of pressure and oil mist on windage power loss of a shrouded spiral bevel gear," *Proceedings of ASME Turbo Expo*, 2011.

[27] Y. Yamada and M. Ito, "Frictional Resistance of Enclosed Rotating Cones with Superposed Throughflow," *Journal of Fluids Engineering-Transactions of the ASME*, vol. 101, no. 2, pp. 259–264, 1979.

[28] S. Rapley, C. Eastwick, and K. Simmons, "The application of CFD to model windage power loss from a spiral bevel gear," *Proceedings of the ASME Turbo Expo 2007, Vol 6, Pts A and B*, pp. 47–56, 2007.

[29] S. Rapley, *Computational investigation of torque on spiral bevel gears*. Thesis, University of Nottingham, 2009.

[30] S. Rapley, C. Eastwick, and K. Simmons, "Effect of Variations in Shroud Geometry on Single Phase Flow over a Shrouded Single Spiral Gear," *Proceedings of the ASME Turbo Expo 2008, Vol 4, Pts A and B*, pp. 1483–1492, 2008.

[31] T. Webb, H. Morvan, and C. Eastwick, "Parametric modelling of a spiral bevel gear using CFD," *Proceedings of the ASME Turbo Expo 2010: Power for Land, Sea and Air*, 2010.

[32] T. Webb, H. Morvan, and C. Eastwick, "CFD modelling of gear windage losses: two phase modelling using particle injections," *Proceedings of the ASME 2010 10th Biennial Conference on Engineering Systems Design and Analysis*, 2010.

[33] W. Strasser, "CFD Investigation of Gear Pump Mixing Using Deforming/Agglomerating Mesh," *Journal of Fluids Engineering - Transactions of the ASME*, vol. 129(4), pp. 476–484, 2007.

[34] L. Li, H. Versteeg, G. Hargrave, and T. Potter, "Numerical Investigation on Fluid Flow of Gear Lubrication," *SAE International Journal of Fuels and Lubricants*, vol. 1(1), pp. 1056–1062, 2009.

[35] Y. Yamada and M. Ito, "Frictional Resistance of Enclosed Rotating Cones .1. Frictional Moment and Observation of Flow with a Smooth Surface," *Bulletin of the Jsme-Japan Society of Mechanical Engineers*, vol. 18, no. 123, pp. 1026–1034, 1975.

[36] Y. Yamada and M. Ito, "Frictional Resistance of Enclosed Rotating Cones .2. Effects of Surface-Roughness," *Bulletin of the Jsme-Japan Society of Mechanical Engineers*, vol. 19, no. 134, pp. 943–950, 1976.

[37] M. Wimmer, "An Experimental Investigation of Taylor Vortex Flow between Conical Cylinders," *Journal of Fluid Mechanics*, vol. 292, pp. 205–227, Jun 1995.

[38] M. N. Noui Mehidi, "Gap effect on taylor vortex size between rotating conical cylinders," *15th Australasian Fluid Mechanics Conference*, December 2004.

[39] S. Rapley, C. Eastwick, and K. Simmons, "Computational investigation of torque on coaxial rotating cones," *Journal of Fluids Engineering - Transactions of the ASME*, vol. 130, Jun 2008.

[40] D. Gaden and E. Bibeau, "A numerical investigation into the effect of diffusers on the performance of hydro kinetic turbines using a validated momentum source turbine model," *Renewable Energy*, vol. 35, pp. 1152–1158, 2010.

[41] E. D. Kay, “Integrated IGB Model,” Tech. Rep. UTC-JF59 UTC Annual Report, University of Nottingham Rolls-Royce University Technology Centre in Gas Turbine Transmission Systems, 2010.

[42] ANSYS, “ANSYS FLUENT 12.0 Theory Guide.” Southpointe, 275 Technology Drive, Canonsburg, PA 15317, 2009.

[43] H. K. Versteeg and W. Malalasekera, *An Introduction to Computational Fluid Dynamics*. Longman Group Ltd., 1995.

[44] C. W. Lee, *Air and oil flow investigations in an aeroengine bearing chamber*. PhD thesis, The University of Nottingham, 2004.

[45] S. V. Pantankar and B. E. Spalding, “A calculation procedure or the heat, mass and momentum transfer in three-dimensional parabolic flows,” *International Journal of Heat and Mass Transfer*, vol. 15, p. 1782, 1972.

[46] B. E. Launder, “The numerical computation of turbulent flows,” *Computer Methods in Applied Mechanics and Engineering*, vol. 3, pp. 269–289, 1973.

[47] V. Yakhot and S. A. Orszag, “Renormalization-Group Analysis of Turbulence,” *Physical Review Letters*, vol. 57, pp. 1722–1724, Oct 1986.

[48] M. Wolfshtein, “The velocity and temperature distribution of one-dimensional flow with turbulence augmentation and pressure gradient,” *International Journal of Heat Mass Transfer*, vol. 12, pp. 301–318, 1969.

[49] H. C. Chen and V. C. Patel, “Near-wall turbulence models for complex flows including separation,” *AIAA Journal*, vol. 26(6), pp. 641–648, 1988.

[50] T. Jongen, *Simulation and modelling of turbulent incompressible flows*. PhD thesis, EPF Lausanne, Lausanne, Switzerland, 1992.

[51] B. A. Kader, “Temperature and Concentration Profiles in Fully Turbulent Boundary-Layers,” *International Journal of Heat and Mass Transfer*, vol. 24, no. 9, pp. 1541–1544, 1981.

[52] S. A. Morsi and A. J. Alexander, "An Investigation of Particle Trajectories in Two-Phase Flow Systems," *Journal of Fluid Mechanics*, vol. 55(2), pp. 193–208, 1972.

[53] P. Gorse, K. Dullenkopf, H. J. Bauer, and S. Wittig, "An Experimental Study on Droplet Generation in Bearing Chambers Caused by Roller Bearings," *Proceedings of the ASME Turbo Expo 2008, Vol 4, Pts A and B*, pp. 1681–1692, 2008.

[54] K. Simmons, D. Guymer, and A. Turner, "CFD Investigation into Oil/Air Behaviour Near a Shrouded Spiral Bevel Gear," *Proceedings of the ASME Turbo Expo 2014: Turbine Technical Conference and Exposition*, 2014.

[55] P. J. O'Rourke and A. A. Amsden, "A Spray/Wall Interaction Submodel for the KIVA-3 Wall Film Model," *SAE Paper 2000-01-0271*, 2000.

[56] C. Mundo, M. Sommerfeld, and C. Tropea, "Droplet-Wall Collisions:Experimental Studies of the Deformation and Breakup Process," *International Journal of Multiphase Flow*, vol. 21(2), pp. 151–173, 1995.

[57] ANSYS, "ANSYS FLUENT 12.0 User's Guide." Southpointe, 275 Technology Drive, Canonsburg, PA 15317, 2009.

[58] S. Muzaferija, M. Peric, P. Sames, and T. Schellin, "A Two-Fluid Navier-Stokes Solver to Simulate Water Entry," *Proceeding of 22nd Symposium on Naval Hydrodynamics*, 1998.

[59] J. U. Brackbill, D. B. Kothe, and C. Zemach, "A Continuum Method for Modeling Surface-Tension," *Journal of Computational Physics*, vol. 100, pp. 335–354, Jun 1992.

[60] L. Schiller and A. Naumann, "Fundamental calculations in gravitational processing," *Zeitschrift Des Vereines Deutscher Ingenieure*, vol. 77, pp. 318–320, 1933.

[61] A. Glahn, M. Kurreck, M. Willmann, and S. Wittig, "Feasibility study on oil droplet flow investigations inside aero engine bearing Chambers - PDPA techniques in combination with numerical approaches," *Journal of Engineering for Gas Turbines and Power-Transactions of the ASME*, vol. 118, pp. 749–755, Oct 1996.

[62] A. Glahn, S. Busam, M. F. Blair, K. L. Allard, and S. Wittig, "Droplet generation by disintegration of oil films at the rim of a rotating disk," *Journal of Engineering for Gas Turbines and Power-Transactions of the ASME*, vol. 124, pp. 117–124, Jan 2002.

[63] Root Soultions Ltd, *Pro/Engineer Wildfire 4.0.* Root Soultions Ltd.

[64] ANSYS, *ICEM CFD 13.0.* ANSYS Inc., Southpointe, 275 Technology Drive, Canonsburg, PA 15317.

[65] A. Kovats, *Design and performance of centrifugal and axial flow pumps and compressors.* Pergamon Press, 1964.

[66] A. Turner, H. P. Morvan, and K. Simmons, "A computational investigation into the effects of inlet swirl on a shrouded spiral bevel gear," *Proceedings of the ASME Turbo Expo 2015: Turbine Technical Conference and Exposition*, 2015.

[67] G. Johnson, "SAMULET 3.5.2 - Gear Windage CFD Validation Data Phase 1 - Two-Phase Visualisation," Tech. Rep. FF81/GJ/01, The University of Nottingham Rolls-Royce University Technology Centre in Gas Turbine Transmission Systems, 2012.

[68] P. Tkaczyk and H. Morvan, "SILOET: CFD Modelling Guidelines of Engine Sumps," tech. rep., Nottingham University Technology Centre in Gas Turbine Transmission Systems, 2012.

[69] E. D. Kay, *A depth-averaged model for non-isothermal rimming flow driven at the surface by droplet impact*. PhD thesis, The University of Nottingham, 2013.

[70] B. Chandra, K. Simmons, S. Pickering, S. H. Collicott, and N. Wiedemann, "Study of gas/liquid behaviour within an aeroengine bearing chamber," *Proceedings of ASME Turbo Expo 2012: Power for Land, Sea and Air*, 2012.

Appendix A

In conjunction with the work reported in Chapter 5, a study was conducted to determine a realistic chamber swirl velocity to use as an inlet boundary condition in subsequent gear-shroud subsystem models. This study attempted to combine a full tooth sub-model with one of the outer IGB chamber and thereby determine the velocities and conditions present in the outer chamber. Due to the computational expense of modelling both of these regions together, two separate models were simulated and coupled with a proposed iterative approach.

In the first instance boundary conditions at the shroud outlet hole were determined from the full tooth model calculated in Chapter 4. These variables were then used as inlet boundary conditions for a second chamber model to determine chamber flows. Boundary conditions at the shroud inlet of this chamber model were then used as the inlet conditions for the full tooth model. The intention was to iterate this process until a converged swirl inlet value had been reached, see Figure 8.1.

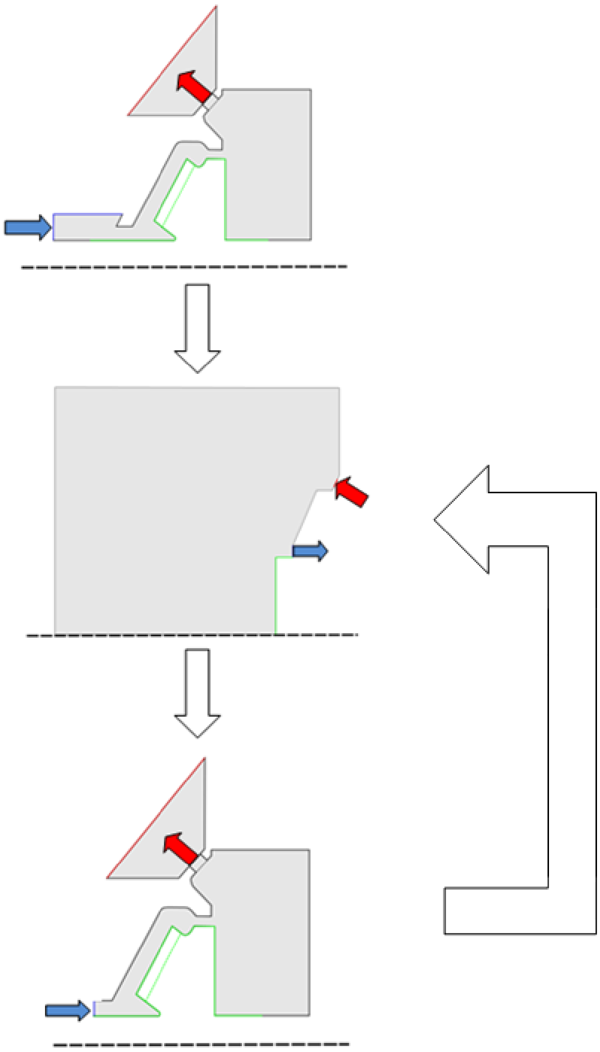

Figure 8.1: Image showing the iterative approach to converge the boundary conditions between the full tooth model and the main chamber model. First a full tooth simulation is computed. The outlet flow of this model is set as the inlet of the main chamber model. The main chamber model is then computed and the outlet flow is then set as the inlet to a second full tooth model. This process is then iterated until the boundary conditions at the inlets and outlets converge to a consistent value.

Chamber Model Formulation

A computational domain was formulated to be as a simplified version of the UTC gear windage test facility geometry. An outline of the computational domain can

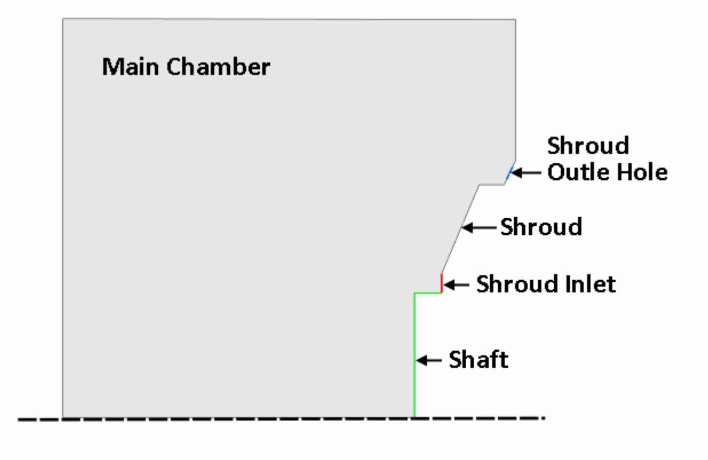

Figure 8.2: Figure of the main chamber model domain with all boundaries labelled.

be seen in Figure 8.2. A curved $1/23^{rd}$ section was modelled for consistency with the coupled spiral bevel gear model.

A mesh density of 400,000 cells was used. A mesh independence study on this geometry has been conducted and published by Simmons et al. [54]. This work shows the geometry is mesh independent above 400,000 cells as shown in Figure 8.3.

Due to the comparable flow velocities and mesh densities at the model inlet and outlet, a similar computational methodology as described in Chapter 4 was applied to model the chamber flow. A key change is that a stationary reference frame is used because the flow is axisymmetric. In the case of the shaft, a rotational speed of 12266 RPM is set on the wall to match the rotational speeds used in the full tooth model.

A velocity inlet is used for the inlet to the chamber and a velocity profile is provided from the full tooth model. This profile includes data on the velocity components, turbulence and static pressure values. The outlet from the chamber is set as a pressure outlet with a static pressure of -200 Pa, which is equal to the

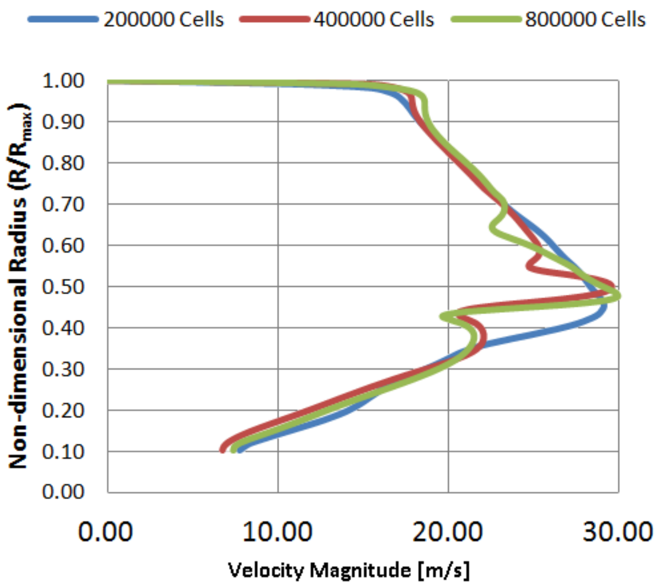

Figure 8.3: Graph of the main chamber mesh independence for cell densities of 200,000, 400,000 and 800,000. Figure is taken from Simmons et al [54].

pressure in the full tooth model at this position. This pressure drop simulates the gear drawing in air from the chamber. Boundary conditions for the chamber model are shown in Figure 8.2.

As with the full tooth model the K-ϵ RNG turbulence model was used. 85% of y* values for the chamber were within the range 20-50 and therefore standard wall functions were used.

Convergence is measured by monitoring general residuals for the whole domain and C_m on the rotating components. Continuity converging to an order of magnitude of 10^{-5}, velocity and energy to 10^{-6} and turbulence criteria to 10^{-5}, typically within 25 inner iterations. C_m was monitored until it's average value per revolution was within 3% for successive revolutions.

Time averaged data was recorded and averaged over 15 revolutions from the point the model was judged to have reached a converged state.

Computational Results

As has been reported in Chapter 5, shroud outlet velocities are relatively insensitive to variations of swirl at the shroud inlet. As a consequence it was found that only one full tooth model/chamber model iteration was required to converge the inlet swirl velocity.

A representative inlet swirl velocity was calculated from the velocity field in the main chamber. Figure 8.4 shows a contour of circumferential velocity in the entire chamber and a close up view of the velocity at the shroud inlet. The location of the full tooth model inlet boundary is marked in black. From this figure it is apparent that the circumferential velocity in the main chamber is fairly uniform throughout and typically within the range 10-20 ms^{-1}. At the inlet boundary location the average swirl number is approximately 0.89 (refer to Chapter 5 for more information of the swirl numbers used in this thesis). This value was then used as the typical inlet swirl for the models simulated in Chapter 4.

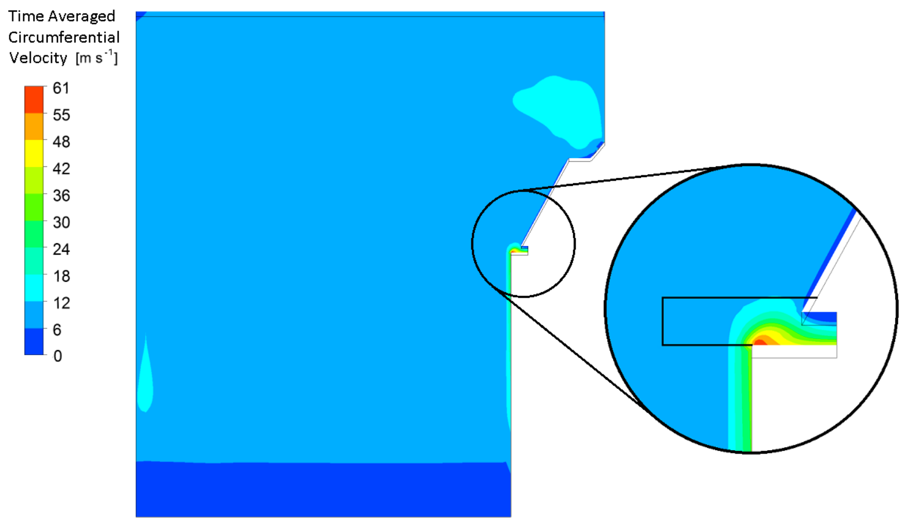

Figure 8.4: Figure showing the contours of time average circumferential velocity in the main chamber. A close up of the swirl velocity in the region of the shroud inlet is also shown.

It was also necessary to determine a representative pressure to set at the full tooth model's inlet and outlet pressure boundaries. As with the inlet swirl velocity, this was determined from the main chamber model.

The main chamber is not pressurised and the pressure field is solely determined by the pressures set at the model inlet and outlets as well as the rotating shaft wall. Figure 8.5 shows a contour of the total gauge pressure variation in the main chamber. This is fairly uniform throughout the chamber and is within the low range of 250-300 Pa. The inlet and outlet locations are marked in Figure 8.5 as points 1 and 2 respectively and show that there is a negligible variation in total pressure at between these two locations. As a result, it was determined that the pressure at the inlet and outlets of the full tooth model could be set to zero gauge pressure. A benefit of this boundary condition is it is possible to compare the full tooth models from Chapter 4 more directly with Webb's simulations [24], all of which were calculated with atmospheric pressure boundaries.

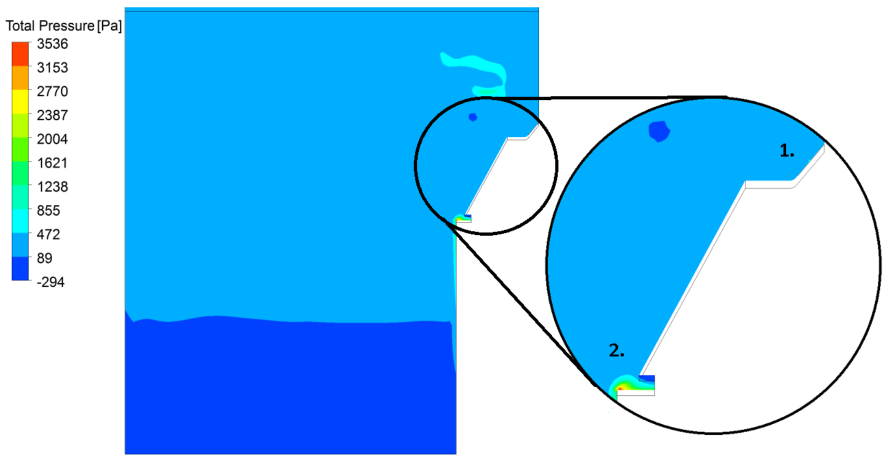

Figure 8.5: Figure showing the contours of time averaged total gauge pressure in the main chamber. A close up of the pressure in the regions of the shroud outlet (point 1) and the shroud inlet (point 2) is also shown.

Conclusions

This work was conducted to inform the boundary conditions for the models calculated in Chapter 4. It has been determined that a representative azimuthal swirl number at the shroud inlet is 0.89 and, due to the negligible pressure difference at between the shroud outlet hole and shroud inlet, it is valid to set a pressure at these boundaries of 0 Pa.